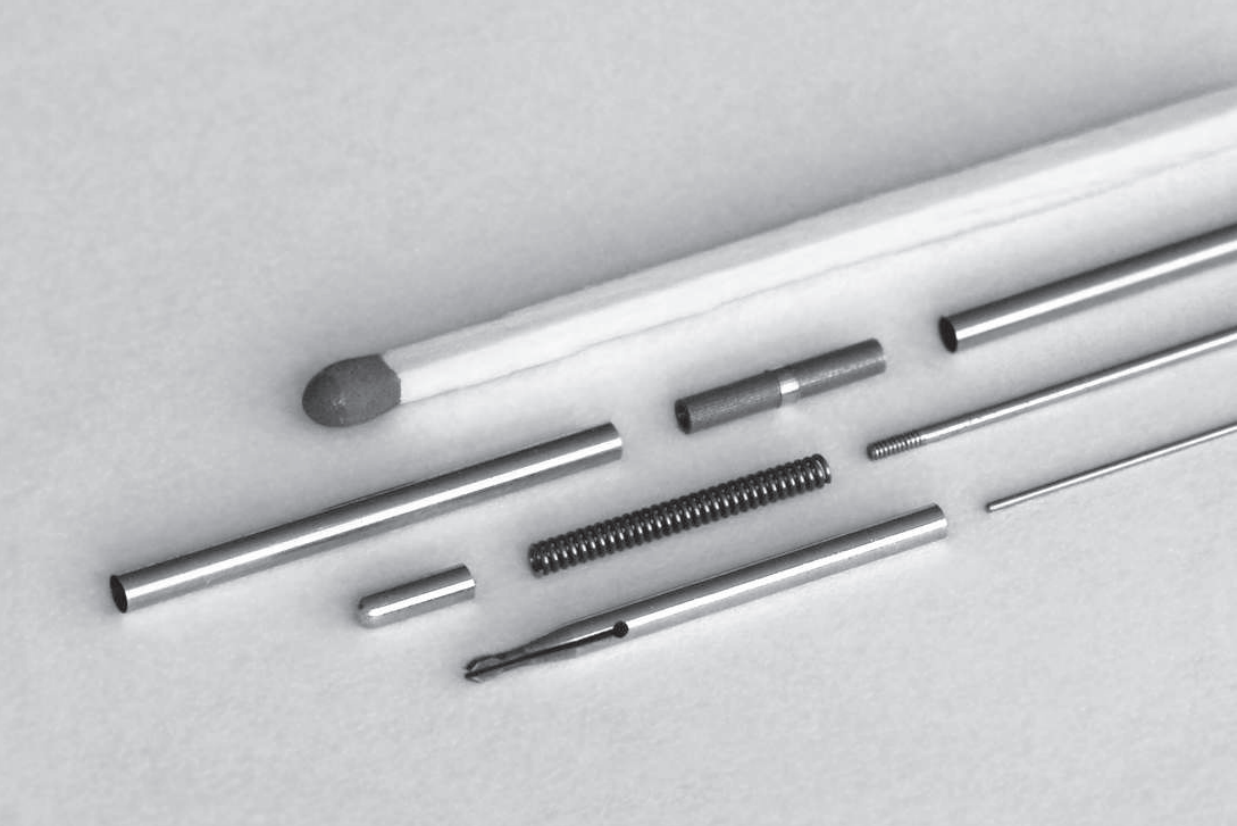
Endovascular crossing of Chronic Total Occlusions using impact force

An explorative design-study

Marleen van der Wiel





Endovascular crossing of Chronic Total Occlusions using impact force

AN EXPLORATIVE DESIGN-STUDY

by

Marleen van der Wiel

in partial fulfillment of the requirements for the degree of

Master of Science

in Mechanical Engineering

at the Delft University of Technology

Main supervisor: Prof. Dr. Ir. P. Breedveld TU Delft Daily supervisors: Ir. A. Sakes, TU Delft

Ir. P.W.J. Henselmans TU Delft



CONTENTS

1	Introduction	1
	1.1 Chronic Total Occlusions	
	1.2 State of the art treatment	
	1.3 Goal of the study	
	1.4 Layout of this report	3
2	Design direction	4
	2.1 Introduction	
	2.3 Crossing method	
	2.4 Impact method theory	
	2.5 Exploration goals	
9		9
3	Design 3.1 Introduction	•
	3.2 Design requirements	
	3.3 Design argumentation	
	3.3.1 Actuation element	
	3.3.2 Indenter	12
	3.3.3 Reload mechanism	
	3.4 Final conceptual design	16
4	Prototype	16
	4.1 Prototype objective	
	4.2 Prototype design	
	4.3 Development and assembly	18
5	Experiment	19
	5.1 Goal of the experiment	
	5.2 Experiment design	
	5.2.1 Indenter performance	
	5.2.2 Puncture effectiveness	
	5.4 Discussion	
c		
	Discussion	28
7	Conclusion	31
8	Acknowledgements	31
Bi	bliography	33
A	Artery modelling	37
В	Actuation feasibility review	43
C	Actuation critical review	45
D	Technical Drawings	51
E	CTO model creation	59
F	Experimental data sets	61

Endovascular crossing of Chronic Total Occlusions using impact force: an explorative design-study

ABSTRACT - Background: Chronic Total Occlusions (CTOs) are the most challenging lesions of Percutaneous Coronary Intervention (PCI). The most common failure mode is the inability to cross the lesion with a guidewire. Crossing is complicated by the lack of guidewire stiffness and the high penetration force of the fibrous proximal cap of the CTO, often causing guidewire buckling during penetration attempts. Therefore, the goal of this study was to explore a novel method to puncture the proximal cap of the CTO.

Methods: Theoretical analysis and modelling of the clinical case and crossing action resulted in the selection of the "impact method", comprising the application of impact force onto the CTO that potentially causes fracture of the proximal cap without (large) environmental disturbance through an inelastic collision. This method was transformed into a functional prototype design, which was subsequently evaluated on its mechanical performance and puncture effectiveness, by means of High Speed Video (HSV) analysis, peak force measurements, and tests with different developed CTO models, representing variable CTO material characteristics.

Results: The developed prototype (\emptyset 2 mm) uses a distal spring-loaded indenter (of different shapes) with a novel reload mechanism to exert impact force onto the CTO. The maximum indenter momentum and mean peak force, at 1 mm object distance and with maximized spring force, were experimentally determined at 1.3 mNs (mass 0.39 grams, mean velocity 3.4 m/s (n = 5)) and 19 N (n = 10), respectively. The puncture effectiveness of the indenter strike was found to be dependent on material characteristics of the targeted CTO model and the indenter tip shape. Proximal cap models with hard and brittle characteristics were fractured most effectively; on average in less than three indenter strikes with non-pointed indenter tip shapes.

Conclusions: The impact method and prototype have shown potential to fracture fibrocalcific cap models. However, to draw final conclusions on potential (safe) endovascular crossing of CTOs, and the most optimal design (parameters) of the instrument, more knowledge on biomechanical properties of CTOs, or an in-vivo experiment, is needed. Nevertheless, it is believed that continued research and development of the method may, in time, improve the endovascular treatment possibilities of coronary CTOs.

1. Introduction

1.1. CHRONIC TOTAL OCCLUSIONS

Atherosclerosis is a disease that causes artery hardening and narrowing through accumulating cholesterol, calcium, and other waste products found in blood, which forms into plaque inside the artery [1, 2], as shown in Figure 1.1. This condition affecting the coronary arteries, known as Coronary Artery Disease (CAD), is worldwide the largest cause of death, with 13% of the global mortality cases throughout the past decade [3, 4]. lesion type found in atherosclerotic arteries is the Chronic Total Occlusion (CTO), which is defined as a complete artery occlusion of older than 3 months, that blocks the blood flow within the artery [5]. Such lesions are identified in 15% to 30% of the patients with known or suspected CAD, referred for coronary angiography (imaging of the artery lumen) [6].

Occurrence and symptoms of CTOs

CTOs can develop in large and medium-sized arteries throughout the whole body [7]. However, within this study we focussed on coronary CTOs, since these are most difficult to treat. In most cases CTOs arise from

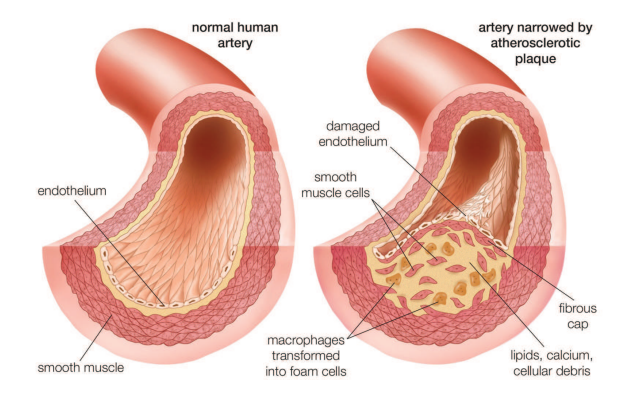


Figure 1.1: Visualization of a healthy human artery (left) and a human artery narrowed by atherosclerotic plaque (right). Figure taken from [8].

a thrombotic occlusion, followed by thrombus organization, and finally tissue aging in the form of calcification [5]. Due to the restriction of blood supply, CTOs may cause dysfunction or death of tissue, heart attack, and stroke [7].

Properties of a CTO

A CTO consists of a heterogeneous mix of materials, including intracellular and extracellular lipids, smooth muscle cells, collagen-rich extracellular matrix, cholesterol, dense collagen, and calcium [5].

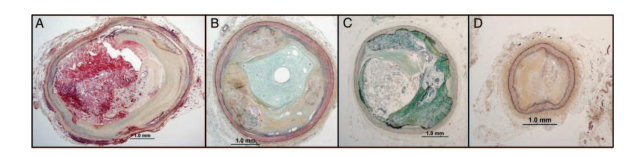


Figure 1.2: Cross-sections of CTOs with varying material properties: (A) organizing thrombus, particular for the core region and young CTO, (B) protoglycan-rich thrombus, (C) calcified CTO, with > 10% calcification, particular for older CTOs, and (D) non-calcified collagen rich CTO with <10% calcification. Figure taken from [9].

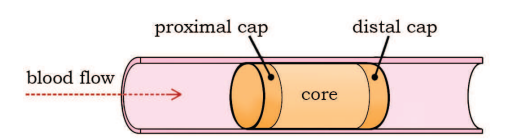


Figure 1.3: Spatial variability model of the CTO, with three specific regions: (1) the proximal cap, (2) the core, and (3) the distal cap.

The material structure differs over age and along the length of the lesion. Figure 1.2 illustrates this material variation. Young CTOs (< 1 year old) consist predominantly of "soft plaque" (cholesterol clefts and foam cells with loose fibrous tissue), but as they grow older the existence of concentrations of fibrocalcific material (calcification) increases, referred to as "hard plaque" [5, 10].

The spatial variability of tissue along the length of the occlusion can basically be described in three specific regions: (1) the proximal cap, (2) the main body (core), and (3) the distal cap, as shown in Figure 1.3. The proximal cap is a thickened fibrous structure at the proximal end of the CTO. It is observed to be the hardest part of the lesion and contains particularly densely-packed collagen. The distal cap is a similar thickened structure, however, it is somewhat thinner and softer compared to the proximal cap. The core, in between the two caps, is softer, and consists mostly of organized thrombus and lipids [5, 10, 11].

1.2. STATE OF THE ART TREATMENT

The current possibilities to treat coronary CTOs include medication, bypass graft surgery, and revascularization through Percutaneous Coronary Intervention (PCI). The chosen treatment modality is individually determined, dependent on measures of the severity of the disease (CAD) and symptoms, as well as individualized treatment risk/benefit analysis [12]. Based on the emerging evidence of positive clinical effects of revascularization of CTOs through PCI, and the introduction of new treatment devices, Stone et al. [12] conclude that PCI should be considered the preferred initial treatment modality in patients for which high procedural success rates are anticipated. Nonetheless, as a result of the low technical probability of accomplishing successful revascularization without complications, many

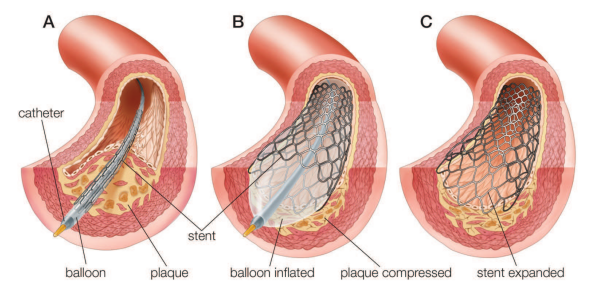


Figure 1.4: The basic procedure of PCI on an artery narrowed by atherosclerotic plaque: (A) placing a balloon catheter over the guidewire, (B) inflation of the balloon (compressing the plaque to the arterial wall and expanding the stent), and (C) the resulting reopened artery with implanted stent. Figure taken from [13].

patients are referred to medication or bypass surgery. The low procedural success rates of percutaneous revascularization of CTOs (55% to 80%) in comparison with non-occluded or acutely occluded arteries (>95%) demonstrate why CTOs are referred to be the "last frontier" of PCI [5, 12]. An increase of the technical success rate, and associated decrease of referral, is desired. Therefore, this study focussed on revascularization of chronically occluded coronary arteries through PCI.

Percutaneous Coronary Intervention

For the revascularization of an occluded artery through PCI, a sheath is introduced into the vascular system at a large peripheral artery, for example the femoral artery. From here, PCI instruments (mostly guidewires and a guiding catheter) are advanced towards the subjected coronary artery, under radiographic visualization. Subsequently, the tip of a guidewire is passed across the occlusion. With the guidewire acting as a pathway through the occlusion, a balloon catheter is pushed inside the lesion and inflated, to compress the plaque against the blood vessel wall, reopening the artery. Additionally, the reopening procedure may be supported by the implantation of a stent (wire mesh tube) guided over the balloon and expanded by balloon inflation, as shown in Figure 1.4.

Failure modes

During the described PCI procedure there are several possible failure modes that cause the low procedural success rates. A study by Kinoshita et al. [14] presents the inability to cross the lesion with a guidewire as most common failure mode of the procedure, with 63% of the failure cases. This failure mode can be attributed to a combination of two main factors: (1) the biomechanical properties of the CTO, and (2) the functionality and properties of the guidewire. Increasing age, and related level of calcification, of a lesion are reported to be factors that negatively affect the chances of successful CTO crossing [12, 15]. Considering the higher tensile strength of calcium

compared to softer thrombus, it can be concluded that crossing old and heavily calcified CTOs asks for high puncture forces. In the occurrence of a failed attempt to cross a CTO, the proximal fibrous cap of the lesion has likely acted as a physical barrier to accessing the CTO [10, 11]. The guidewire, used during the intervention, can be characterized as a long and flexible rod. The flexibility that is needed to passively guide this wire through the vasculature from incision to lesion, is associated with low device stiffness. Axial loading of a guidewire with low overall stiffness may result in instrument failure, in the form of buckling. Guidewire buckling hinders the transmission of exerted forces towards the instrument tip, and may, therefore, obstruct penetration through the lesion.

It is assumed that guidewire buckling is the most common cause of failure to cross the lesion with the instrument. On account of this assumption, the focus of this study was on the problem that the current most frequently used tools for the procedure (guidewires) cannot provide sufficient force to cross the most heavily calcified CTOs. Although attempts to improve the chance of successful revascularization of CTOs have been made, through the development of new medical devices, to (partly) replace the guidewire, and procedural techniques, the stated problem still exists.

Innovation of devices

In literature, multiple devices that have been designed to enable crossing of total occlusions in the vascular system are described. A large variety of crossing methods can be distinguished. A first example is the use of concentrated energy from a saline fluid-jet for the crossing of occlusions (patent [16]). Similarly, lasers may be used to resect tissue through high energy beaming of light (CVX-300 Excimer Laser, Spectrametrics Inc., Colorado Springs, CO, USA). Also, more mechanical approaches such as rotation drilling (Wildcat catheter, Avinger, Redwood City, CA, USA, Figure 1.5 (a)), vibration (Crosser catheter, FlowCardia, Sunnyvale, CA, USA), and blunt microdissection (Frontrunner XP, Cordis Corporation, Miami, FL, USA, Figure 1.5 (b)) are developed into devices for artery revascularization. These examples either use a complete different strategy for crossing the lesion, compared to the axial force push of the guidewire, or combine the axial push with a second direction of loading (radial/ tangential). Even though the broad innovation of PCI instruments might seem promising to solve the CTO crossing problem, statistics and practical instrument use do not underpin this speculation.

From all of the developed devices, only several devices have been approved for clinical practice.





Figure 1.5: (a) *Wildcat catheter* (Avinger, Redwood City, CA, USA). (b) *Frontrunner XP* (Cordis Corporation, Miami, FL, USA).

The proposed main reasons for abandonment of devices are safety and lack of advantages over the standard equipment. Increased crossing possibility might not always outweigh the risks of artery wall damage [17]. Also, high expenses and operation difficulty were found as reasons for abandonment. In other cases, devices have never been developed into functional clinical prototypes, due to a lack of proper functioning, funding, or possibility for small-scale manufacturing. In the cases of successful device introduction, the improved treatment performance has been attributed mostly to the use in peripheral arteries.

Even so, the development and practical use of several innovative devices has contributed to a steadily increased technical and procedural success rate of PCI in CTOs. However, success rates are still undesirably low for this lesion subtype, suggesting the need for more innovation that is focussed on this specific intervention. Therefore, it was questioned if a new crossing method could be found, that would show higher potential for endovascular crossing of CTOs, compared to the current state of the art, by means of focussing on puncturing the proximal fibrous caps of heavily calcified CTOs.

1.3. GOAL OF THE STUDY

The desire for the innovation of a clinical instrument for endovascular crossing of CTOs, in combination with the idea to focus on the part of the lesion that is most difficult to cross with the currently availble instruments, has led to a global description of the study objective as follows: "Explore a new method to puncture the proximal caps of heavily calcified coronary CTOs during PCI." This explorative study has been performed in a process covering theoretical derivation of a promising crossing method, translation of the method into a functional prototype design, and validation of the method through experimentation.

1.4. LAYOUT OF THIS REPORT

The entire process of the development and evaluation of a crossing method and instrument will be discussed within this report. First, in Chapter 2, an analysis of the design case from a mechanical perspective will be described, that is subsequently used for the idea generation and selection of a promising crossing method. Secondly, in Chapter 3, the complete design process and final conceptual design of an instrument will be expound. design requirements for the overall instrument will be drafted, as well as the conceptual design steps of the several elements within the design. In Chapter 4 the design and manufacturing of a proof-of-principle prototype will be illustrated. Following, in Chapter 5, the validation experiments that are performed with the prototype are presented and discussed. The overall study results, along with study limitations and possible improvements and future applications of the explored method and design, will be discussed in Chapter 6. Finally, in Chapter 7, a conclusion of this study will be drawn.

2. DESIGN DIRECTION

2.1. Introduction

To define a promising new crossing method, a simplified model of the CTO and its environment was developed. Subsequently, ideas for possible crossing methods were generated and a selection of a method was made, based on evaluation with the developed case model. Furthermore, the working principles and variables of influence of the selected method have been examined and described.

Throughout the portrayed theoretical phase, the considered basic instrument design consisted of a specialized instrument tip that is connected with a long flexible shaft to an instrument handle. The design focus throughout this phase was on the instrument tip.

Within the following sections, all the results of the theoretical study phase will be described. The chapter will be concluded with an extended description of the goals of this study, which have been detailed with the input of the selected crossing method.

2.2. CASE MODEL

The developed model of the clinical case will be described in three parts. First, a simplified physical model of a CTO and its environment will be described. Next, the material properties of the main components of this model will be given. Finally, based on the physical model, in combination with the material properties, a mechanical model will be portrayed.

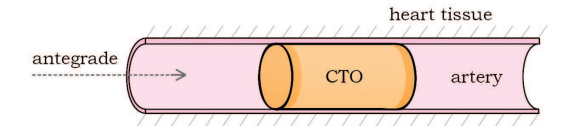


Figure 2.1: Simplified physical model of the CTO (orange, cylindrical block) surrounded by a coronary artery (pink, elastic tube) and heart tissue (grey lines, elastic environment).

Simplified physical model

In the physical model, shown in Figure 2.1, the CTO is characterized as a cylindrical block of material. This block may be subdivided in three regions: two hardened caps and, in between, a softer core. The block is rigidly connected along its entire circumference to an elastic tube; representing the artery. This rigid connection embodies the strong bonds of the plaque material with the inner wall of the artery. Finally, the elastic tube is surrounded by an elastic environment, representing heart (cardiac muscle) and other surrounding body tissue.

Material properties

The material properties of cardiac muscle and the arterial wall, categorized as soft, viscoelastic, tissues, are known to be non-linear. The stiffness of this soft body tissue increases with increased load and tissue deformation. Moreover, the stiffness of these tissues may be largely depended on the direction of the deformation. Therefore, developing a detailed case model, including material properties, is very complex. Nevertheless, in literature, global material properties are mentioned, which give elemental insight in the studied case.

For the arterial wall, elasticity in longitudinal direction is of most interest for the studied case. This is given to be in the range of $200-800\,\mathrm{kPa}$ [18, 19]. For the surrounding body tissue, the cardiac muscle was selected as representative tissue. The elastic modulus of cultured rabbit cardiac muscle cells is measured to be $100\,\mathrm{kPa}$ [20]. For the human cardiac muscle, Chen et al. [21] state that stiffness is between 10-20 and $200-500\,\mathrm{kPa}$, during the start and end of the diastole, respectively.

Characterization of the material properties of the CTO is more difficult. Chai et al. [22] write that experimental information on elastic properties of atherosclerotic plaque is limited and shows large variability, with Young's moduli ranging from 30 kPa to the order of 1 MPa. It must be noted that these numbers represent the elasticity of plaque found in narrowed arteries, rather than in CTOs. The Young's modulus of collagen and calcium are given to be 0.1 – 8 GPa [18, 23] and \sim 20 GPa, respectively. These numbers may be more representative as elasticity modulus for the CTO, since the proximal cap (the area of focus) mainly consists of particularly dense-



Figure 2.2: Simplified mechanical model of the CTO submerged in its elastic environment of artery and heart tissue. The CTO is represented as a somewhat rigid block of material, whereas the surrounding artery and heart tissue are characterized with compression springs and dampers.

packed collagen, and the relative calcium area at the most calcified cross section of a CTO may reach up to 54% in the case of failed PCI [15].

Concluding, the elastic moduli of the cardiac tissue and the arterial wall are found to be of similar magnitude ($\sim 100~\mathrm{kPa}$), and may be much lower than the modulus of CTO material ($\sim 100~\mathrm{MPa}$). However, due to the lack of reported details on CTO material properties, only an assumption can be made that the stiffness of the CTO is much larger than its environment.

Simplified mechanical model

By means of incorporating the obtained information on the material properties within the simplified physical model, a simplified mechanical model was build. In this model, the CTO is represented as a rigid block of material (in which the proximal cap characteristics are taken as representative for the study), suspended with a compression spring and damper in parallel, on either ends of the block, that represent the viscoelastic environment. The model is shown in Figure 2.2. In the most simple form, a single suspension would have been sufficient to model the (linearized) viscoelastic environment, however, the double suspension provided a more appropriate model, in which occurring tension and compression of the environment (upon axial CTO loading) could be distinguished. The scenario prediction that has been performed with the help of this model was based on theoretical reasoning, rather than mathematical modelling, due to the uncertainties of the biomechanical properties of the model parts.

2.3. Crossing method

To propose a promising new crossing method, the mechanical implication of the "crossing" activity was investigated. In this study, "crossing" is defined as the creation of an opening within the targeted material and subsequent moving through the material. For the creation of an opening it is necessary to fracture the material. Fracturing occurs when internal material stresses exceed the cohesive strength of the material, as a result of applied load. Therefore, the search for a crossing method was performed through examining possibilities of applying load onto the CTO. To finally select a promising method, these possibilities have been evaluated with the help of the described case models.

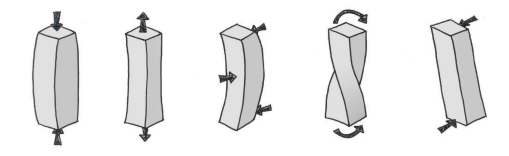


Figure 2.3: The five general methods of material loading. From left to right: compression, tension, bending, torsion, and shear.

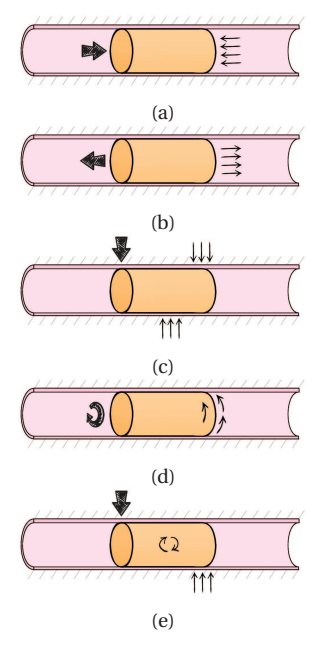


Figure 2.4: The five general methods of material loading placed within the simplified physical model: (a) compression, (b) tension, (c) bending, (d) torsion, and (e) shear. The thick arrows represent the force to be applied by the PCI instrument; the thin arrows characterize environmental force.

Basic load types

In general there are five methods to mechanically load a material: compression, tension, torsion, bending, and shearing. These methods are illustrated in Figure 2.3, in which the arrows portray the application of load. For the evaluation of the methods, they have been placed into the context of PCI with the help of the simplified physical model, which is presented in Figure 2.4. It is assumed that the CTO can only be reached proximally, since the antegrade approach is most commonly the initial approach taken during PCI. Therefore, necessary counterforce to the applied load needs to be provided by the environment.

Deduced from the scenario drawings, the bending and shearing type of load have been excluded as possibilities, due to the inability to approach the CTO sideways. The remaining three load types (tension, compression, and torsion) were subsequently evaluated on the necessary material grip to apply the load. To apply a compressive load, only low grip is needed to prevent slip between instrument tip and CTO, which may be provided by surface friction. For both the tension and torsion

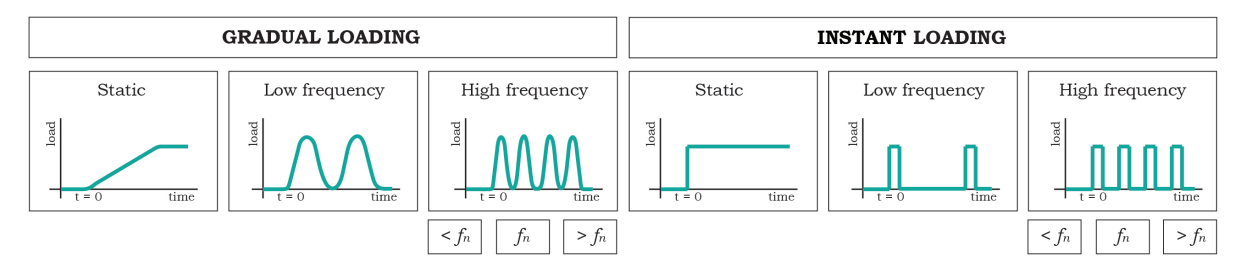


Figure 2.5: Structural categorization of compressive load application methods, classified by their load versus time diagram in two levels. The first level distinguishes gradual and instant loading, the second level discriminates the frequency of the loading/unloading cycle.

load, high grip is needed on the CTO its surface to generate the pulling or twisting force. To gain high surface grip, through, for example, adhesion or vacuum suction, the instrument tip design may become unnecessary complex. Therefore, compression was selected as the favoured load type for this design case.

Detailed method of load application

Loading material in compression is a widely used method for fracturing material. Examples include knife cutting and chopping, needle puncture, hammering, a bullet shot, and jack hammer drilling. These methods are all based on compressive load, however, applied in largely different ways. To gain an overview of all methods, a structural categorization was made based on load versus time diagrams, which is presented in Figure 2.5.

The structure was developed with two separate levels. The first level distinguishes a gradual load application ("gradual loading") from an instant, impact, load application ("instant loading"). The second level characterizes load application on frequency of the cycle of loading and unloading, in three classes. The "static" group is characterized by constant and continuous load application after initial load introduction. The other two groups are characterized by consecutive loading and unloading. The "low frequency" category includes cyclic behaviour that allows stabilization of the system (the CTO and its environment, in this study) in between two subsequent loading cycles. The "high frequency" category is too fast with consecutive loading cycles to allow stabilization of the system in between. This last category may further be subdivided into: vibration below the natural frequency ($< f_n$), at the natural frequency (f_n) , and above the natural frequency $(> f_n)$. To evaluate the several presented methods, the simplified mechanical model was used to sketch the systems behaviour resulting from the different load methods.

The gradual and static loading method, which includes the current guidewire push method for penetrating the CTO, is expected to cause movement of the CTO in an early stage of load application. Due



Figure 2.6: Mechanical scenario sketch of the gradual and static load method, in which the applied load causes movement of the CTO and stretch of the antegrade environment in an early stage.

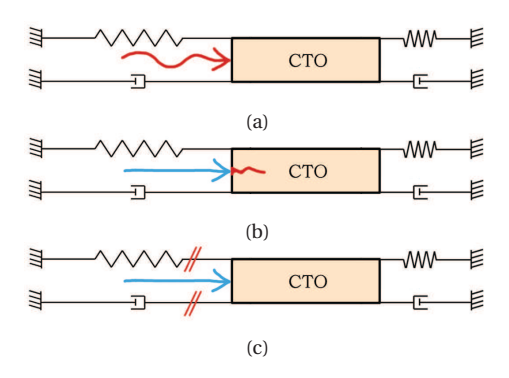


Figure 2.7: Mechanical scenario outcomes of a continuous static compressive push on the CTO: (a) instrument failure, (b) CTO fracture, and (c) arterial wall fracture.

to the comparatively low environmental stiffness, the antegrade arterial wall and surroundings will be stretched, leading to the scenario depicted in Figure 2.6. Consequently, at the point of maximum environmental strain, three scenario outcomes are anticipated, visualized in Figure 2.7: (1) instrument failure, (2) CTO fracture, and (3) arterial wall fracture. In the first scenario, the instrument failure can be devoted to low instrument stiffness, of which guidewire buckling is an example. In case the instrument stiffness is sufficient to cause fracture to the system, the second scenario may occur when the strength of the environmental material exceeds that of the CTO material. Providing the CTO material has a higher strength, compared to its environment, the third scenario may occur. Considering the focus of this study on heavily calcified CTOs, and the described material properties of the CTO and its environment, it is assumed that the compressive strength of the CTO is higher than the tensile strength of the arterial wall. Hence, the desired second scenario seems unlikely. For this reason, the gradual and static load application has been eliminated as

promising solution to safely cross the proximal caps of heavily calcified CTOs.

The gradual and low frequency loading method was judged not to be significantly different from the previous elucidated static scenario. Whereas early unloading may prevent the undesired scenarios of environmental damage and instrument failure to occur, the method is not expected to be more effective in causing the desired scenario of CTO fracture.

The high frequency method, for both gradual and instant loading, seems most interesting in the form of forced vibration at the natural frequency, known as free vibration. In free vibration, the amplitude of vibration increases manifold, which may cause the desired fracture of the material. However. the environmental damping within the system will absorb energy from the vibration. This situation may lead to medically undesired environmental heating. Moreover, due to the varying CTO and tissue characteristics, associated with varying natural frequencies, applying this method may be impossible without also crossing a phase of vibration below or above the natural frequency. For both vibrations below and above the natural frequency of a system, it is difficult to predict the behaviour of the system with a lack of details on the system dynamics. Accordingly, the high frequency categories hold uncertainties for application in this study.

The instant loading, of both the static and low frequency category, is characterized by a collision between a moving body and a non-moving body, which provides an interesting design solution. As a result of the velocity of an impact load, the environmental damping and CTO inertia may play a role in the occurring scenario, acting as a "counterforce" to the incoming compressive load. Such force can prevent sudden movement of the CTO. In case this environmental counterforce is sufficient, the impact load may lead to a scenario of energy absorption by the targeted CTO in the form of material fracture, as presented in Figure 2.8, rather than any environment stretch or damage. An example of this method in practice is the biopsy harvesting method described by Jelinek et al. [24], in which high velocity of the cutting tool minimizes elastic deformation of the targeted material before cutting through it.

To further distinguish the static and the low frequency method of the instant load type, it has been considered how the system would behave in case the impact load does not penetrate the CTO. For the static category, failure of direct penetration may result in similar undesired scenarios as described for the gradual and static load method, due to the continuous load after impact. In the case of short

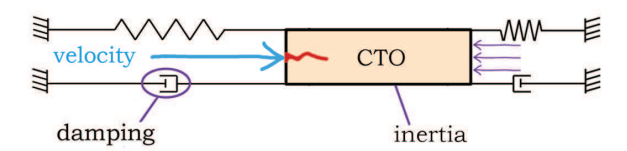


Figure 2.8: The environmental damping components and the inertia of the CTO form "counterforce" to an impact load, which may allow CTO material fracture.

"bouncing" impact shots, with which the low frequency loading may be characterized, direct unloading after loading may prevent the undesired environmental damage. Furthermore, instrument failure may be easier to prevent as the critical buckling load of a thin structure increases with a decrease in load duration [25].

Based on the presented analysis of the different load application methods, the instant and low frequency method, further to be referred to as the "impact method", was judged as most promising to accomplish proximal cap puncture for crossing heavily calcified CTOs. The associated selection of this method was confirmed by the finding that this working principle has not yet been developed into a device for crossing total occlusions.

2.4. IMPACT METHOD THEORY

Considering mechanical theory to elaborate on the impact method, there are two main aspects to be addressed. First of all, the physical interaction of two bodies in collision, and secondly, the formation of fracture within material. In this section, a short review on these topics will be presented. The colliding instrument body, which is depicted as a moving part within the instrument tip, will be referred to as the "indenter" throughout the report.

Collision

The main working principle of the impact method can be descried as a collision between a moving body (the indenter) and an initially non-moving body (the CTO). During the short moment of interaction between the two bodies, kinetic energy of the indenter may be transferred into kinetic energy of the CTO or dissipated into other forms of energy, such as heat or deformation. There are two main types of collision that can be distinguished: elastic collision and (2) inelastic collision. elastic collision is featured by conservation of kinetic energy, whereas during an inelastic collision a part of the kinetic energy before collision dissipates into other forms of energy. Perfect elastic collision of macroscopic bodies is never fully realized, but they may be approximated. In this incident, drawn as "worst case scenario" for our application, both linear momentum ($\mathbf{p} = m \cdot \mathbf{v}$) and kinetic energy ($E_k = \frac{1}{2} \cdot m \cdot \mathbf{v}$) v^2) will be conserved and may be transferred from

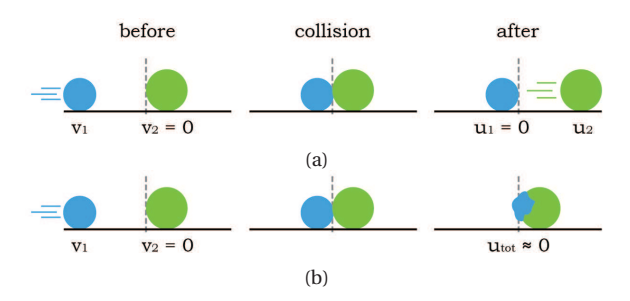


Figure 2.9: Visualization of (a) a perfect elastic collision, drawn as "worst case scenario" for the impact method, and (b) an inelastic collision with high energy dissipation, drawn as "ideal scenario" for the impact method. The term \boldsymbol{v} is used for velocity before collision, and \boldsymbol{u} for the velocity after collision.

indenter to CTO. This is illustrated in Figure 2.9 (a) and with the Equations 2.1 and 2.2. Within the equations, \boldsymbol{v} is used to express velocity before collision, \boldsymbol{u} for the velocity after collision, and m for mass. Moreover, the initial velocity of the CTO and the resulting velocity of the indenter are equated to zero.

$$m_{indenter} \cdot \boldsymbol{v}_{indenter} = m_{CTO} \cdot \boldsymbol{u}_{CTO}$$
 (2.1)

$$\frac{1}{2} \cdot m_{indenter} \cdot v_{indenter}^2 = \frac{1}{2} \cdot m_{CTO} \cdot u_{CTO}^2$$
 (2.2)

The "ideal scenario", on the contrary, can be drawn as a perfect inelastic collision, where the two colliding bodies stick together after collision, and the maximum amount of kinetic energy is lost. For a perfect inelastic collision in a closed system, linear momentum will be conserved, so that the scenario can be presented with Equations 2.3 and 2.4.

$$m_{indenter} \cdot \boldsymbol{v}_{indenter} = m_{total} \cdot \boldsymbol{u}_{total}$$
 (2.3)

$$\frac{1}{2} \cdot m_{indenter} \cdot v_{indenter}^2 > \frac{1}{2} \cdot m_{total} \cdot u_{total}^2 \quad (2.4)$$

In the ideal scenario, however, the resulting velocities of both bodies is equal to zero, preventing CTO movement and allowing energy dissipation to form fracture of the CTO material. The latter case, only to occur due to environmental influences, is presented in Figure 2.9 (b) and with the Equations 2.5 - 2.7.

$$u_{total} \approx 0$$
 (2.5)

$$m_{indenter} \cdot \boldsymbol{v}_{indenter} \gg m_{total} \cdot \boldsymbol{u}_{total}$$
 (2.6)

$$\frac{1}{2} \cdot m_{indenter} \cdot v_{indenter}^2 \gg \frac{1}{2} \cdot m_{total} \cdot u_{total}^2 \quad (2.7)$$

The scenario occurrence is dependent on the system dynamics of the CTO and its environment, as well as the dynamics of the indenter. In this study, the system dynamics of the CTO are unclear and may be largely variable between lesions. Accordingly, it is difficult to predict the optimal system dynamics of the indenter. Therefore, it is desired to account for a

variable indenter momentum within the instrument design phase.

Fracture formation

Other than the design variables velocity and mass, the indenter shape may also be of large influence for optimal functioning of the impact method. Material stress, which causes fracture, is related to the amount of applied force as well as to the area of impact of this force. This relation is shown in Equation 2.8, in which σ represents the amount of stress, F the applied force, and A the area of impact. The latter component may differ with variable indenter shapes.

$$\sigma = \frac{F}{A} \tag{2.8}$$

Considering the given expression, a decrease in area of impact will increase material stress, which can be related to easier fracture. This line of argumentation supports the selection of a sharp shaped indenter. A practical example of a sharp indenter shape is the tip of a needle, puncturing skin with low effort. However, also blunt shaped indenters have been designed for optimal fracturing, for example used to fracture hard and brittle rock material through chip formation.

A difference in fracture forming can be found between elastic material, that allows material compression, and brittle material, which does not compress. The latter material is characterized by "brittle fracture", which includes material pulverization and chip formation upon compressive load. This is in contrast to material tearing, which is more common in flexible material. Therefore, the optimal indenter tip shape design is material dependent.

For the design of the shape of the indenter, both optimal fracture results and medical risks should be considered. Medical risks can, for example, be found in chances of arterial wall puncture, facilitated by sharp tools. These risks may be anticipated and taken into account by means of design guidelines for the instrument. The optimal fracture results, however, are difficult to predict, due to the uncertainty of the material properties of the CTO. Consequently, it is desired to explore the effect of the indenter tip shape on efficient crossing through the proximal caps of CTOs, by means of experiments with both blunt and sharp indenter designs.

2.5. EXPLORATION GOALS

As a result of the main theoretical phase, described throughout this chapter, the study goal stated within Chapter 1.3 has been adjusted as follows: "Explore the possibilities in design and the effectiveness of the impact method to puncture the proximal caps of

heavily calcified coronary CTOs during PCI." It was a goal to explore the design possibilities for a new medical instrument, that is able to apply impact force strikes, and designed within the dimensional limitations of instruments used in PCI. Moreover, it was desired to acquire knowledge on the mechanical performance of such an instrument. Finally, it was desired to explore experimentally if the instrument is able to fracture hard material surrounded by elastic tissue, and what indenter tip shape works most effective for this application.

3. DESIGN

3.1. Introduction

Designing is an activity that encompasses continuous deliberation between different design requirements and wishes. The optimization of a product on aspects of function, as well as safety and production costs, may lead to conflicting solutions. Within the design process of every product, it is the main challenge to find a golden mean of design, in which all aspects are deliberately weighed. The continuous consideration of multiple aspects makes it difficult to design with a pre-defined straightforward process; rather it becomes iterative, with multiple small design cycles. This describes globally the design process that has been worked through, for the design of the desired instrument to explore the impact method for puncturing heavily calcified CTO proximal caps.

In this chapter, the instrument design will be described by the main components it envelopes. For each of these components, as well as for the design requirements, the road of design activities and argumentation will be explained, giving insight in the deliberation between aspects. Finally, the chapter is concluded with an overview of the complete instrument design.

3.2. DESIGN REQUIREMENTS

To describe and demarcate the desired instrument, global design requirements have been defined in three categories: (1) functional requirements, (2) geometrical requirements, and (3) medical safety requirements. In the first category, the requirements describe the required functioning of the instrument, focusing on the impact strike action. Within the second group of requirements, the dimensional limits are described. Finally, the third category includes requirements and safety margins for the prevention of medical trauma.



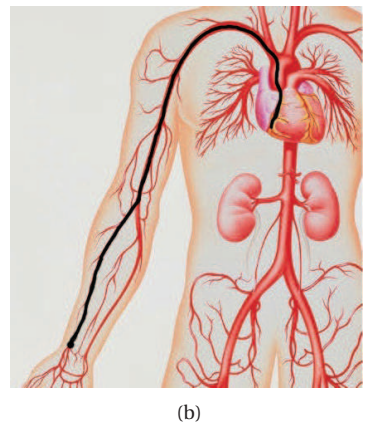


Figure 3.1: Approaches in PCI to reach the RCA: (a) the transfemoral approach, reaching the RCA from the groin, and (b) the transradial approach, reaching the RCA from the wrist. Figures adjusted from [26].

Functional requirements

The main function of the instrument is to deliver an impact force onto the proximal cap of the CTO. As described in Chapter 2.4, it was desired to explore the design possibilities and effectiveness of variable indenter momentum. For this exploration, it was decided to prioritize the evaluation of maximum feasible velocity (requirement 1.1), considering high velocity is needed to make optimally use of the CTO inertia and damping of the surrounding tissue. The desired variability of indenter momentum and indenter tip shape has been described in a second requirement (requirement 1.2).

On top of these basic functional requirements, two requirements have been added, dedicated to the use and reliability of the instrument. First of all, reload ability of the impact strike action was desired, to allow for multiple strikes without exchanging the instrument (requirement 1.3). Secondly, it was desired that the impact strike is consistent over location and time (requirement 1.4). In more detail, the brought impact should be independent of instrument shape and not influenced by the iteration of the action.

Geometrical requirements

The geometrical requirements have been subdivided in three different categories: tool diameter, length and flexibility. These requirements were determined by analysing the vascular system from incision to lesion, by different approaches in PCI, as well as by looking at current PCI tools in use. The most prevalent location of a coronary CTO is the Right Coronary Artery (RCA) [5], which may be reached with a transfemoral or a radial approach, as shown in Figure 3.1. A detailed analysis of these approaches can be found in Appendix A. It was concluded that within these approaches the RCA and radial artery are

Table 3.1: Complete overview of the design requirements in three categories.

Func	ctional requirements				
1.1	Indenter velocity	The indenter velocity should be maximized			
1.2	Indenter variability	The indenter momentum and tip shape should be variable for experimentation			
1.3	Reload ability	The indenter strike action should be repeatable, without exchange of the catheter instrument			
1.4	Consistency	The indenter strike action should be consistent, independent from CTO location or action iteration.			
Geor	netrical requirements				
2.1	Diameter	The maximum tool diameter is 2.0 mm			
2.2	Flexibility	The tool should be flexible; the maximum stiff part length is 6.5 mm			
2.3	Length	The tool length should be scalable without affecting the indenter strike action			
Medi	Medical safety requirements				
3.1	Operation risks	The design should be actively evaluated on medical risks and interference with other tools			
3.2	Indenter reach	The indenter reach should be limited			
3.3	Indenter bounce	The indenter should be able to bounce during the action			
3.3	Indenter sharpness	The indenter tip should be rounded with a minimal radius of 0.2 mm			



Figure 3.2: Part of the analysis of curvature and bifurcations in the transferoral and transradial approach to reach the RCA: (1) the curvature of the aortic arch, (2) the bifurcation of the aortic arch to the RCA, and (3) the curvature of the RCA. The dimensions given are in mm. Left figure adjusted from [26].

smallest in diameter; in the range of 3 mm [27–34]. Looking at currently used tools, the typical outer diameter of practically used catheters is 2 mm [35]. Combining this information, it was decided that a maximum diameter of 2 mm would be suitable for a first instrument design (requirement 2.1).

Furthermore, the approaches were analysed on curvature and bifurcations to define the needed flexibility of the tool. For an instrument to make a certain curvature, the maximum stiff part length is limited. This maximum stiff part length was calculated with the help of bifurcation and curvature modelling, of which an example is shown in Figure 3.2. In Appendix A, a complete overview of the performed modelling and calculations can be found. In conclusion, the maximum stiff part length was defined to be 6.5 mm (requirement 2.2).

Finally, the catheter should be scalable to different lengths, to be used in different interventional procedures. The current practically used tools are available in a wide range of lengths, typically with an average of 100 to 110 cm [35]. The initial tool length for the design was set to 100 cm, however, it was later decided that the tool should be scalable to different lengths, without influencing the performance (requirement 2.3).

Medical requirements

For the introduction of a medical device in clinical practice, there are strict regulations that are meant to minimize the risks of device-related trauma. The medical instrument to be designed should, at least, not increase the risks of the intervention. It is for this reason that throughout the design process, the design should be actively evaluated on possible medical risks and interference with current medical practices, such as X-ray guidance (requirement 3.1).

Furthermore, to minimize the main risk of arterial wall damage, a threesome of safety margins were set. First of all, there should be a possibility to limit the indenter reach, giving control of location reach and preventing the indenter to disconnect from the tool (requirement 3.2). Secondly, the indenter should be able to bounce back from the CTO in case no penetration is achieved, which prevents the risks presented with the static loading scenario in Chapter 2.3 (requirement 3.3). Lastly, the sharpness of the tool should be restricted, to limit chances of arterial wall dissection. The smallest guidewires used in current PCI have a diameter of approximately 0.4 mm with a spherical tip, therefore, the minimal tip radius was set to 0.2 mm (requirement 3.4).

In table 3.1 an overview of all requirements, organized in the three presented categories, is given.

3.3. DESIGN ARGUMENTATION

The conceptual design of the instrument was divided in three main elements: (1) the actuation element, (2) the indenter, and (3) the reload mechanism. Multiple brainstorm activities have been performed to find potential design solutions for each of these elements. Subsequently, structuring and reviewing of the solutions for all elements was performed to finally select the most feasible instrument tip design. In the upcoming sections the deliberation for defining the design of each of these three elements will be discussed.

3.3.1. ACTUATION ELEMENT

The first system part that was defined is the actuation element. For the instrument to apply an impact

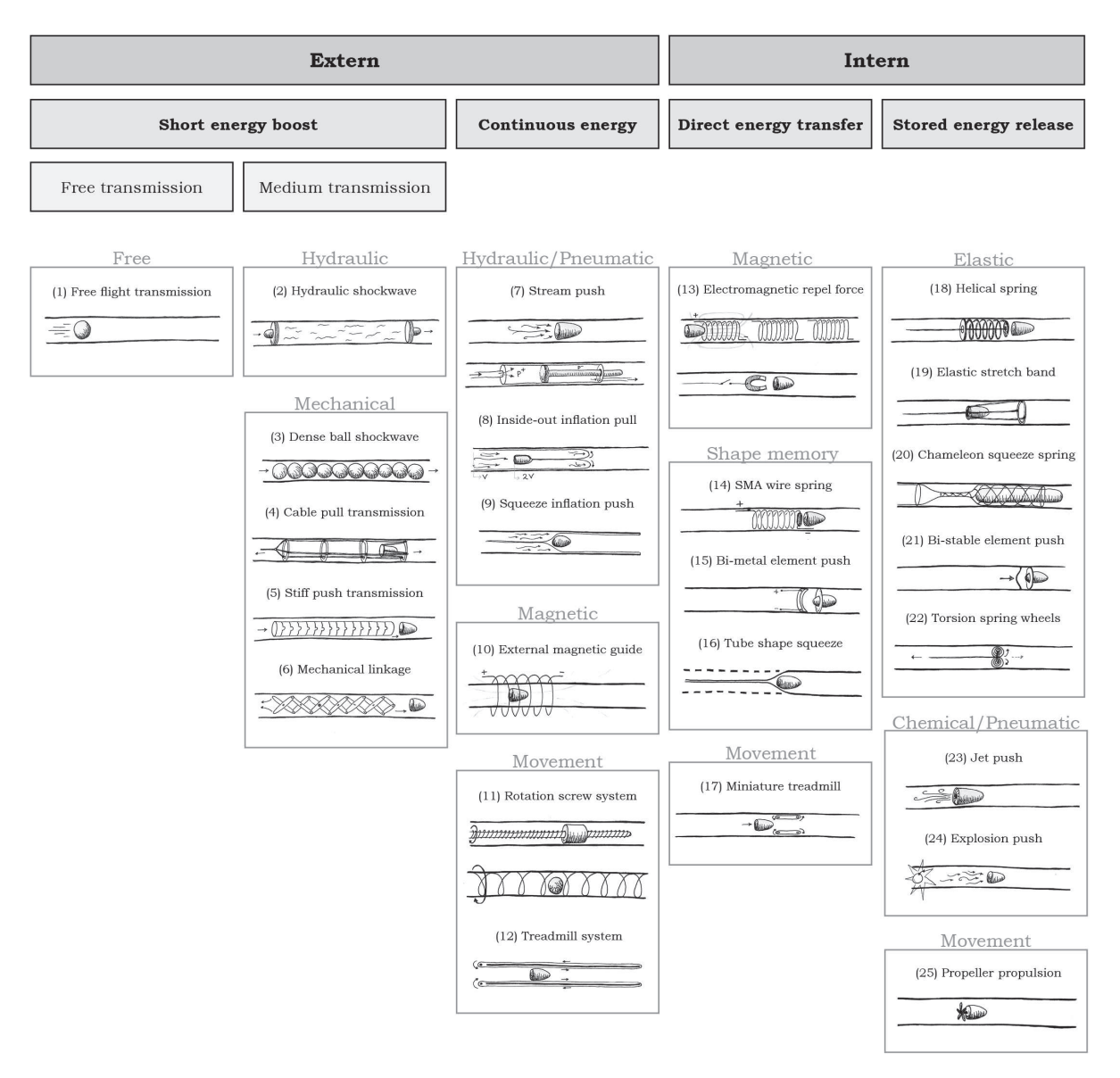


Figure 3.3: Idea structure of the 25 conceptual ideas for the actuation element. Distinction is made between the location of momentum generation (internal) and the method of momentum transmission (external) and momentum generation (internal).

force onto the CTO, the indenter part should have a translational momentum, which needs to be generated. The function of the actuation element is to ensure indenter momentum at the instrument tip.

Idea generation and structuring

By means of several brainstorm sessions, ideas of possible actuation elements were generated, which resulted in a total of 25 conceptual ideas. These ideas are presented in the structure of Figure 3.3. The ideas were subdivided based on the location of momentum generation; either outside ("extern") or within the tool ("intern"). In the external category, the momentum can be generated through a short impulse input with a passive transmission of the momentum towards the instrument tip ("short

energy boost") or it can be transmitted towards the instrument tip through a more continuous energy supply ("continuous energy"), for example, by a hydraulic stream push. The short energy boost category is further subdivided based on the method of transmission; either free flight ("free transmission") or through a medium ("medium transmission"), such as a hydraulic shockwave. For the internal generated momentum category, a distinction is made between a direct energy transfer from source to momentum ("direct energy transfer"), for example the transfer of electrical energy to momentum through an electromagnetic force, and the sudden release of stored energy ("stored energy release"), such as elastic energy stored in a compressed spring.

Feasibility check

For the selection of one of the ideas as actuation element, two consecutive reviews were made. First of all a basic feasibility check of all ideas was executed, after which the feasible ideas were critically judged and compared with a more in depth performance analysis.

The feasibility check was based on five aspects, derived from the set design requirements: medical safety, (2) dimensional feasibility, (3) level of reachable velocity, (4) reload ability, and (5) shape independency (the consistency of the action, independent of the shape of the instrument its flexible shaft). In Appendix B, a detailed explanation of these aspects and the associated arguments is For 10 of the ideas it was argued to be unfeasible to develop the actuation method within the limited diameter of the desired instrument. Negative marks were also given to 9 ideas that were judged to realize much lower velocities in comparison to other ideas. Moreover, all ideas within the category of "short energy boost" were judged to be highly shape dependent, largely influencing the momentum resulting at the tip of the instrument, excluding them from further reviewing. The medical check has led to the exclusion of pneumatics and chemicals only, and the reload ability seemed least feasible to be developed for the 3 "squeeze" ideas. The five ideas that were not judged negatively on one (or more) of the review aspects have been classified as feasible, including: (1) hydraulic stream push, (2) electromagnetic coil, (3) shape memory alloy (SMA) wire spring, (4) helical spring, and (5) elastic stretch band.

Actuation selection

To make a deliberate decision between the five ideas that were judged feasible, an in-depth review of the potential critical factors of each design was performed. A detailed description of this critical concept review is given in appendix C. By means of basic modelling and calculation, it was concluded that the electromagnetic coil showed least promising results for velocity generation. For the SMA wire spring too little information was found to make an estimation of velocity generation, and was, therefore, rated as uncertain. Furthermore, both the electromagnetic coil and SMA wire spring were judged to include a possible medical risk, as resistive heating of the wire occurs, which could lead to undesired heating of body tissue in a worst case scenario. The elastic stretch band was judged to be the less favourable elastic solution, due to the nonlinearity of rubber elasticity. One of the most critical factors of the hydraulic concept was found to be the influence of instrument shape on flow

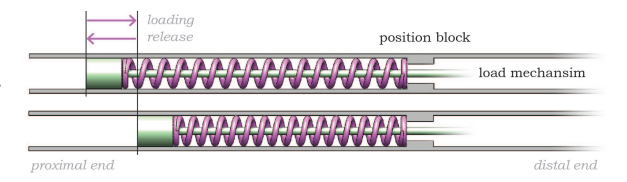


Figure 3.4: Configuration of the compression spring (purple) in the instrument tip, with the distal end blocked in position and the proximal end free to move. The spring can be compressed by forcing the proximal end backwards (by means of a load mechanism, green), after which the stored elastic energy is available during release.

resistance, and, therefore, on the action consistency. For the helical spring, it was found that the design of a reload mechanism would comprise of a mechanism that can be decoupled during the release action, to prevent shape dependency and high friction influences of the mechanism on actuation performance. This mechanism was judged as most critical factor of this concept, as it would increase the complexity of the concept largely.

Based on this review, it was concluded that a helical compression spring, which is widely off-the-shelve available in small dimensions, was the most favourable actuation element for the instrument. This concept was judged to have the least medical risks, due to its purely mechanical working principle. Also, it should perform highly independent of instrument shape, with the actuator located in the tip of the instrument. Furthermore, the estimates on velocity generation performance were most positive (4 m/s - 13 m/s for indenter masses of 1.0 - 0.1 gr, respectively, neglecting any influences of friction). Finally, the added complexity of the reload mechanism to be designed for this concept, was intuitively rated lower than the overall complexity and uncertainties that would come with the design of the other concepts.

In the final conceptual design, the actuator is arranged as shown in Figure 3.4. A compression spring is located in the tip of the instrument, positioned by a shape block at its distal end. To store elastic energy, the spring can be compressed from its proximal end. At the moment the spring is released to deform back into its original length, it will produce a forward push, that can be utilized to accelerate an indenter.

3.3.2. INDENTER

Within the instrument, the indenter is the part that will apply the impact force onto the CTO. It is located at the proximal end of the compression spring, to be accelerated by spring release after compression. The indenter has been designed in three main phases. First, a basic shape and method of functioning was defined. Secondly, an indenter stop was designed to limit the reach of the indenter. Finally, the

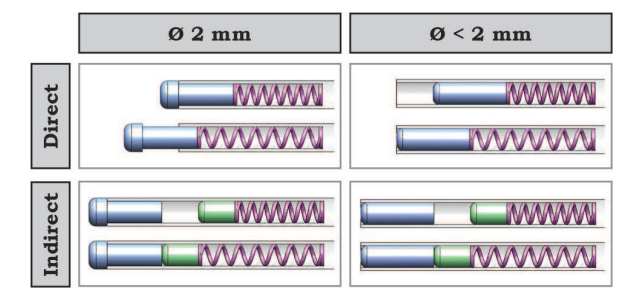


Figure 3.5: Idea structure for the basic shape and functioning of the indenter. The basic shapes (diameter dependent) and basic interaction forms are presented within the rows and columns of the structure, respectively.

possibilities of indenter momentum and tip shape variation were examined and designed.

Basic shape and functioning

The main considerations made for a basic indenter shape and method of functioning are shown in the structure presented in Figure 3.5. For the basic tip shape a maximum length of 6.5 mm was taken into account (requirement 2.1). Furthermore, two options have been considered for the indenter diameter: (1) a part with the maximum of 2 mm outer diameter at the tip, and (2) a part that fits completely within the catheter with an inner diameter < 2 mm (requirement Additionally, two ideas for the interaction between the indenter and the spring and reload mechanism were considered: (1) direct interaction, and (2) indirect interaction. In the case of direct interaction, the indenter is directly accelerated by the spring. The indirect interaction uses an extra part to compress the spring, which subsequently transfers its momentum to the indenter through collision.

In evaluation, the direct interaction method was rated as the most efficient (fewer energy losses) and simplistic (less parts) method. Furthermore, it was argued that the solution of the indenter fitting inside the catheter is the more favourable solution, because it allows to use the catheter tube to align with the CTO for a consistent reach distance. The advantage of a Ø 2 mm indenter was defined to be the possible creation of an opening sufficiently wide to advance the complete instrument through the CTO. However, it has been argued that only initial fracturing of the proximal cap would be sufficient to meet the goals for this project. Based on this argumentation, the basic design with direct spring-indenter interaction and the smaller diameter, completely enveloped by the catheter (Figure 3.5, upper right), was selected as most suitable design option.

Indenter stop

To make sure the indenter has a limited reach in its action to puncture the CTOs, fulfilling requirement 3.2, a stop for the indenter was integrated into the



Figure 3.6: The shape lock ideas for the indenter stop design, with either a narrowed part of the catheter or a protruding part of the indenter that slides in a slot carved into the catheter.

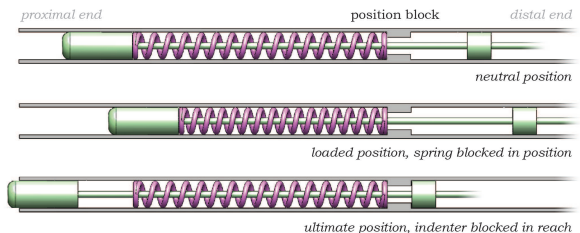


Figure 3.7: Configuration of the selected indenter with stop, using the narrowed catheter part of the spring position block to prevent forward movement of the indenter at a pre-defined ultimate position. The "neutral position" shows the spring in rest (free length), the "loaded position" shows the spring being compressed from its proximal side, and finally the functioning of the indenter stop is shown with the "ultimate position".

design. For this stop ideas have been generated in two main categories: (1) a shape lock, and (2) a permanent connection. In an early selection phase, the second option was excluded, due to the reason that a permanent connection between the indenter and the spring is difficult to manufacture. shape lock, which may be shaped by for example a narrowing part of the catheter or a protruding indenter part that locks into a slot, as illustrated in Figure 3.6, was determined to be the more simple and favourable solution. The protruding indenter design, however, was judged to detrimentally decrease the stiffness and strength of the catheter tube and was potentially more complex in manufacturing. Therefore, the shape lock with a narrowed catheter part was selected.

In the final conceptual design, the shape lock was positioned at the distal end of the spring. In this location, the element to block the spring in position was given a double function: (1) block the spring during compression (proximal side), and (2) block the indenter in its reach (distal side). A down side of this design decision was the necessary extension of the indenter through the spring, leading to an increased effect of friction on performance due to an extended contact surface. However, this also led to a desired increase of space for the reload mechanism design. The indenter design illustrated in Figure 3.7 represents the final configuration in the instrument.

Indenter momentum variation

With the selected actuation method, indenter momentum may be adjusted by means of the distance of maximum spring compression; a shorter

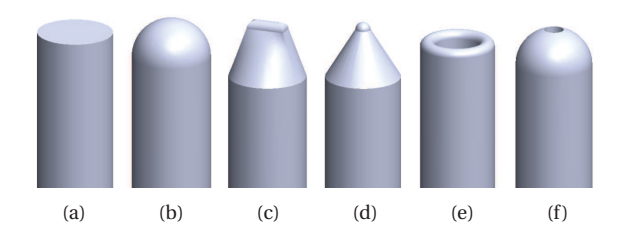


Figure 3.8: The variable indenter tip shapes designed for exploring the effectiveness of sharp, blunt and hollow shapes on CTO fracture: (a) stamp indenter, (b) spherical indenter, (c) wedge indenter, (d) pointed indenter, (e) ringed indenter, and (f) spherical indenter with guidewire passage.

distance of compression will decrease the force acting on the indenter and shorten the acceleration path, resulting in lower indenter velocity, and, correspondingly, lower indenter momentum.

To vary the mass of the indenter, the indenter volume may be varied, as well as the indenter material density. While designing the final indenter, however, it was encountered that mass variation could only be realized with small differences; limited by undesired friction effects of increased indenter length, and material availability, hardness, and machinability. Hence, indenter mass variability has not been implemented within the final instrument design.

Indenter tip variation

To define the specific shapes of the indenter, a short literature review on commonly used indenter shapes was performed. This has resulted in a set of four basic shapes, which are explicitly described in a review of indenter rock fracturing by Guo In the category of "blunt" tip design this includes a right-angled "stamp" indenter (Figure 3.8 (a)) and a "spherical" shaped indenter, with the tip radius equal to the indenter radius (Figure 3.8 (b)). The "sharp" tip design category includes a "wedge" indenter (Figure 3.8 (c)), leaving a lined imprint, and a "pointed" indenter (Figure 3.8 (d)), both with an edge radius of 0.2 mm (maximum sharpness, as stated in requirement 3.4). These four shapes provided a transition from completely blunt to maximal sharpness. On top of these basic designs, two hollow shapes were added. These designs allow for guiding another system through the instrument, such as a guidewire or balloon catheter, for a possible The illustrated "ringed" indenter future design. (Figure 3.8 (e)) was designed with a maximized inner passage diameter: the indenter diameter minus four times the edge radius. Finally, an indenter was shaped with a spherical tip and a Ø 0.4 mm passage, through which the thinnest guidewires can pass (Figure 3.8 (f)).

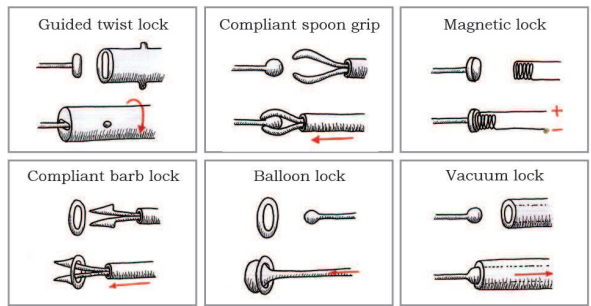


Figure 3.9: Several examples of the conceptual solutions for a reload mechanism that allows a couple and decouple action.

3.3.3. RELOAD MECHANISM

The reload mechanism allows for compressing and triggering the spring in such a way that the loading and release action can be performed multiple times without exchanging the instrument from the body. For the design of this reload mechanism, there were two main design guidelines. First of all, the mechanism should ultimately be designed to generate a pulling force at the indenter to realize the spring compression. Secondly, to load and release the spring multiple times, the mechanism should have a couple and decouple function. Furthermore, two main design challenges were taken into account. Firstly, the mechanism should work without control feedback, because most of the haptic feedback will be lost with the transmission throughout the long and flexible shaft of the instrument. Secondly, since the narrow diameter of the instrument highly limits the design freedom in radial direction, displacements in the mechanism should be minimal in this direction.

Idea generation

Several conceptual solutions for the reload mechanism were found. These ideas ranged from mechanisms that make use of a shape lock to ideas including controllable force generators and systems with multiple preloaded parts. A selection of the conceptual solutions is shown in Figure 3.9. The "guided twist lock" and the "compliant barb lock" are both shape lock ideas, in which a passive connection (no energy input) between the parts is created through shape change during the coupling action. The "balloon lock" and "compliant spoon grip" may also be categorized as shape lock, but in these concepts the connection between the parts is actively held with energy input, through continuous pressure (hydraulic or pneumatic) and force grip, respectively. Finally, the presented "magnetic lock" and "vacuum lock" are mechanisms with an actively controlled lock, where attractive forces are created to connect two parts.

All of the ideas were judged on their feasibility, which excluded the "vacuum lock" due to the medical

risk of pneumatic leakage in arteries, as well as the "magnetic lock" due to insufficient force generation. Moreover, the "guided twist lock" was excluded due to the necessary torsional input force, which may be difficult to be transmitted through the instrument its flexible shaft. Finally, the "balloon lock", based on a hydraulic system, was judged to be undesirably complex, compared to the two mechanical compliant lock ideas. Therefore, the compliant ideas were selected as most promising solutions for the reload mechanism.

Compliant lock design

The main analogous characteristic of both compliant lock solutions (the "compliant barb lock" and the "compliant spoon grip"), is the use of flexible parts that deform when connecting with the indenter. The two flexible spoon shaped gripper plates from the spoon grip idea deform outwards to move over the ball that is to be gripped. The gripper of the barb lock idea, consisting of two barbed plates, deforms inwards to move through a ring that is to be gripped. Furthermore, the two ideas are contradictory in their methods of grip and control. The barb lock has a grip within the gripped part, is locked passively by its shape, and is actively triggered to decouple, whereas the spoon grip grasps around the gripped part, is actively locked by the tube, and is decoupled passively when the tube grip is removed. Through this analysis of grip and control method, a systematic ideation on possible other combinations arose, presented in Figure 3.10. In this matrix, the upper left and lower right cell can be filled with the two presented ideas. To fill the two remaining cells, compliant lock ideas working with a moveable core were developed. In the upper right cell, a gripper is shown that will deform to move into a hollow part, in which it will find its coupled position. Subsequently, a core will be pushed forward into the gripper to actively lock the grip, which prevents slipping of the grip during the loading phase. For the lower left cell, the solution includes a core that is used to push open a set of grippers that grasp around a part, to release the coupled state.

In evaluation, it was argued that an active lock is more favourable than an active release mechanism. In case a passive lock is created with a compliant gripper, there is a risk of early release due to deformation of the gripper initiated by the spring forces acting on the gripped part. Moreover, the active lock designs have the advantage that the release is initiated with a pulling force, rather than a pushing force. The latter may be more sensitive to obstructions when transmitted through the instrument shaft. In the active release solutions, this pushing force is to be given at the moment with

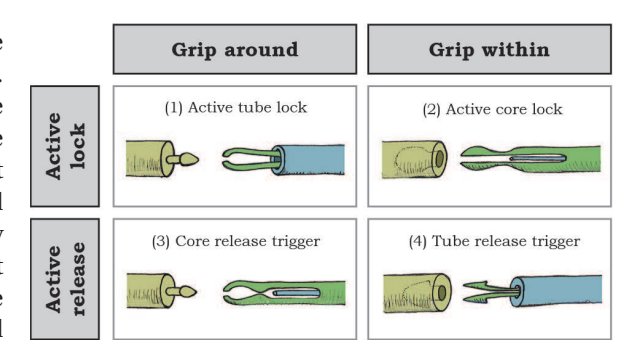


Figure 3.10: Idea structure for the possible compliant reload mechanisms. The grip method is given at the top and the method of control is presented on the left.

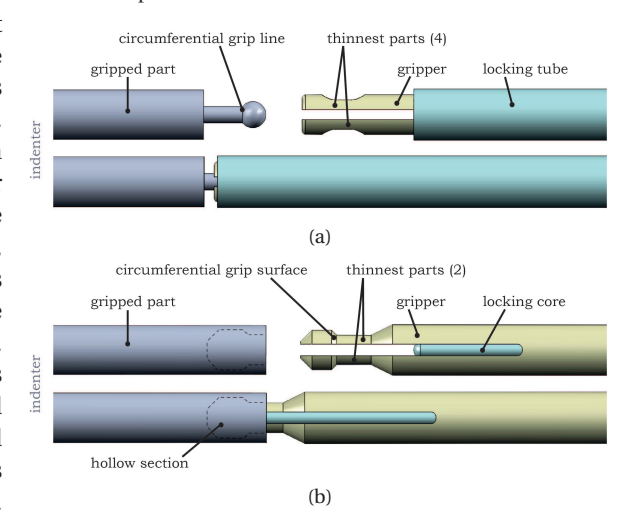


Figure 3.11: Detailed design of the two compliant reload mechanisms that have an actively locked position, in decoupled (upper) and locked (lower) configuration: (a) the "active tube lock" mechanism, (b) the "active core lock" mechanism.

maximum tension on the spring and reload mechanism, whereas in the active lock concepts, the pushing action is used only in the non-tensed state of the system, which is preferred.

To make a distinction in suitability between the two active lock mechanism, a detailed design of both mechanisms was made, as shown in Figure 3.11. Based on this design detailing, it was decided to implement the "active core lock" (Figure 3.11(b)), because it was judged as the more robust design. The "active tube lock" included thinner parts, that are more susceptible to undesired and permanent deformation, and grasps only along a circumferential line, rather than a circumferential surface, as found in the active core lock design.

To conclude, the final conceptual design of the reload mechanism consists of three parts: (1) the gripped part, (2) the (compliant) gripper, and (3) the locking core. The gripped part is the most distal part of the indenter, that contains a hollow section to connect the gripper. Similar to the proximal indenter part, a maximum length of 6.5 mm for the gripped part was taken into account (requirement

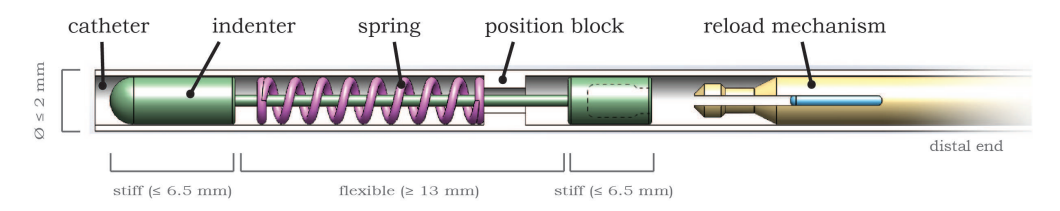


Figure 3.12: A cross-sectional representation of the final conceptual instrument tip design, consisting of five main parts: Catheter (tube), indenter, compression spring, position block, and load- and trigger mechanism.

2.1). To ensure the flexibility of the instrument, a minimum length of 13 mm (double the length of the stiff parts) was used as guideline for the separation of the two stiff parts of the indenter. The gripper was designed with two specifically shaped plates that can deform inwards to move through a narrowed opening into the hollow section of the indenter. Once the gripper is positioned, the core can be pushed forward to actively lock the position of the gripper, preventing position slip. At this moment, the complete mechanism may be pulled backwards to compress the spring. The subsequent removal of the core by pulling it backwards from the gripper will trigger inward deformation of the two gripper parts, by which the mechanism decouples and the indenter may accelerate.

3.4. FINAL CONCEPTUAL DESIGN

Bringing together the three presented instrument components, the final conceptual design for the tip of the instrument can be described with five main parts (see Figure 3.12): (1) a catheter tube, (2) the indenter, (3) a compression spring, (4) a position block, and (5) the reload mechanism. The catheter tube functions as the instrument shell, for smooth gliding through the vascular system, and guiding the indenter, spring, and reload mechanism internally. The indenter is the part that will ultimately collide with the CTO to cause fracture and penetration of the proximal cap. Moreover, it functions as part in the reload mechanism, where it is used to gain grip on the proximal end of the spring for compression. The compression spring is the actuation element in which elastic energy is stored that will be transformed into indenter momentum (kinetic energy) during release. The position block has a double function: it blocks the distal end of the spring from moving backwards during compression, and it blocks the indenter in forward movement at a pre-defined maximum reach distance. Finally, the reload mechanism will couple and decouple to the indenter, to compress the spring and to trigger the spring release for indenter acceleration, respectively.

In a final, clinical, instrument, this instrument tip should merge at its distal end into a flexible shaft that consists solely of the catheter tube and reload gripper and core part. Ultimately, an instrument handgrip should be developed at the most distal end of the instrument, to handle the complete instrument and to control the reload mechanism. The design of these clinical instrument parts was not part of this study. Rather, a rigid, proof-of-principle prototype has been developed. This prototype includes the complete instrument tip as presented, connected directly to a control interface, which will be presented within the following chapter.

4. PROTOTYPE

4.1. PROTOTYPE OBJECTIVE

The objectives for developing a functional prototype were to evaluate the functionality of the impact method and instrument design, as well as the feasibility and manufacturability of the conceptual design in the limited dimensions. It was decided that a minimized and fully rigid prototype would fulfill the described objectives. The results of the transformation from conceptual instrument design to the proof of principle prototype will be described in the following sections.

4.2. PROTOTYPE DESIGN

The prototype design activity mainly consisted of dimensioning the several parts of the conceptual design. Furthermore, a method for exchanging the indenter tip and a control interface for the reload mechanism had to be designed. The design of all parts has been performed largely with the help of 3D-modelling in *Solidworks 2014* (SolidWorks Corp., Dassault Systemes, France).

An exploded view of the core part of the finalized prototype design is presented in Figure 4.1. The outer shell of the instrument tip is a standardized \emptyset 2.0×0.1 mm capillary tube, made in two parts (C) and (E). These two parts are connected with a piece (D) that serves as the position block from the conceptual design, with a \emptyset 1.2 mm central channel. The two capillary tubes fit on either side of the connection piece. The ordered spring (B) for the prototype (COO170003016, Associated Spring SPEC, Evasham,



Figure 4.1: Exploded view of the core part of the finalized instrument prototype, with its 9 components (A-I), showing their axial alignment.

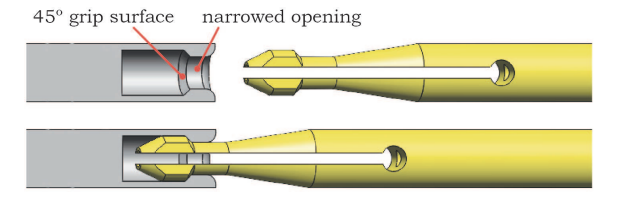


Figure 4.2: Detailed view on the grip part of the reload mechanism.

UK) has an outer diameter of 1.7 mm, wire diameter of 0.32 mm, and free length of 16 mm, fitting perfectly within the capillary tube. This compression spring was one of the stiffest springs available in its dimension range, with a spring rate of 1.3 N/mm and a maximum compression distance of 3.5 mm. The indenter of the conceptual design is designed in two main parts. The indenter tip (A) was designed as a Ø 1.8 mm solid cylinderof 6 mm in length, with the variable tip shapes as earlier presented (Chapter 3.3.2, Figure 3.8). This tip is connected to a \emptyset 1.0 mm rod with the indenter stop at its end (F). An M1 screw connection (3 mm in length) was designed to connect the parts (A) and (F), and serve the exchangeability of the indenter tip (A). The enlarged end (Ø 1.8 mm) of part (F) includes a hollow part that serves to embrace the gripper of the reload mechanism (G1). Within this hollow, a slanted (45°) circumferential surface was formed, as shown in Figure 4.2, that allows surface slip at the moment the lock is released to trigger the action. The gripper part (G1) is made from a thick-walled tube with an outer diamter of 1.8 mm and a Ø 0.5 mm central channel, with a specially shaped tip to fit within the hollow of the indenter stop (F), and with a back part (G2) that was designed to fit the control interface. The compliant movement of the gripper, necessary to allow the gripper (G1) to move through the narrowed opening of the hollow part, is possible by the axial slit (0.35 mm) from the proximal end that divides the tube in two separate parts. The core (I1) that is used to lock the grip and trigger the grip release is a Ø 0.5 mm rod, smoothly fitting within the gripper (G1).

The final control interface, that includes parts G–I, was designed with the main goals to mechanically control the gripper and core separately at precise distances. Moreover, it allows locking of the mechanism in the "loaded" position (spring compressed, reload mechanism coupled). To control the precise distances of the gripper, an axial slot was carved in the bottom of the squared distal part of the

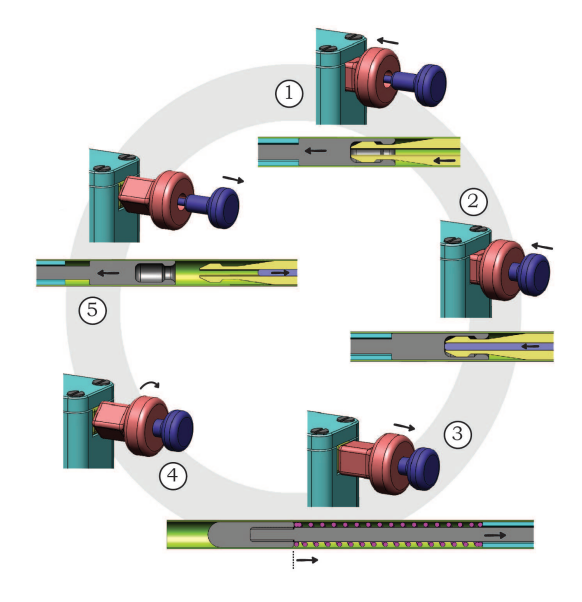


Figure 4.3: Visualization of the functionality of the prototype interface, starting from a decoupled situation.

gripper (G2), sliding over an extruding screw. The axial slot location and length defines the most proximal and distal position of the gripper. Part (H) is connected to part (G) by means of M6 screw-thread, and can be twisted to change the alignment of the squared surface and the distance between the parts (G2) and (H). The core (I1) and the handgrip of the core (I2) are configured together in part (I). The reload mechanism and control interface work as follows, starting from a decoupled situation, (see also Figure 4.3): (1) Forward movement of the gripper parts (G) and (H), pushing the distal indenter part (F) against the position block (D) and the gripper (G1) within the cavity of the distal indenter part (F). (2) Forward movement of the core (I), pushing it within the gripper tip (G1) to lock the grip. (3) Backward movement of the gripper and core (G)-(I), pulling the indenter (A) and (F) backwards to compress the spring (B). (4) Locking the loaded position by twisting the gripper handle (H), creating small reference surfaces that are locked behind the casing of the interface. (5) Backward movement of the core (I), to release the grip lock, and trigger the indenter (A) and (F) to pull loose from the gripper (G1) and accelerate forward as the spring (B) pushes on its tip (A).

Finally, the core part of the functional prototype is enveloped by a small box $(26 \times 41 \times 25 \text{ mm})$, that was designed with a base plate to serve easy surmounting of the prototype in an experimental setup. An

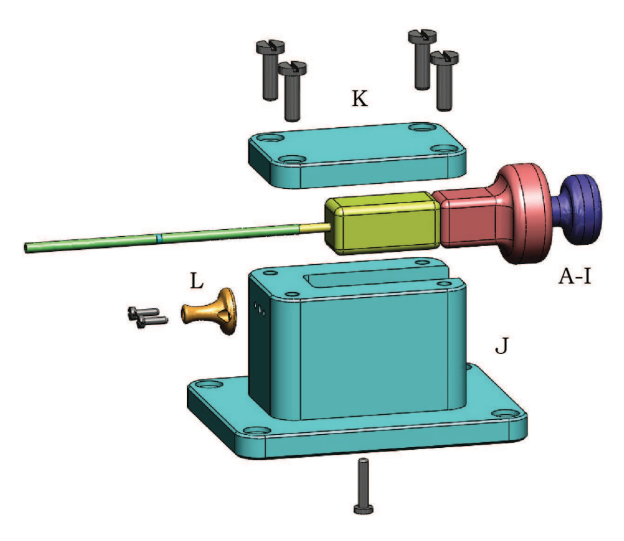


Figure 4.4: Exploded view of the complete finalized instrument prototype, with its 12 components (A-L), with the core (part A-I) assembled as one part.

exploded view of the complete prototype design is shown in Figure 4.4. The main enveloping box consists of a bottom and top part (J) and (K), respectively, that can be fastened by screws. The screw on the lower side of part (J) is the extruding screw aligned within the carved slot of part (G2), for the gripper positioning. Finally, an extra support part to the proximal end of the box (L) was developed to provide an extra 10 mm of support to the thin and fragile capillary tube (E) of the core part of the prototype. The finalized technical drawings of all parts (except the compression spring (B)) can be found in appendix D.

4.3. DEVELOPMENT AND ASSEMBLY

Except for the compression springs and screws, all parts of the prototype have been manufacture at DEMO, TU Delft. Parts (A), (C)-(F), (G1), and (I2) have been manufactured from stainless steel, parts (G2), (H), and (L) from brass, and the box parts (J) and (K) from aluminum. Part (I1) was made from tempered steel, which was the only off-the-shelve available material in Ø 0.5 mm rod. The selection of brass for parts (G2) and (H) was made to allow easy sliding of the control interface parts. Parts (A), (C)-(F), and (G1) were made with the help of wire-cut electrical discharge machining (EDM). The remaining parts were constructed by means of computer numerical control (CNC) milling and turning.

The small manufactured parts and actuation spring (A)-(G1) and (I1) are illustrated in Figure 4.5, next to a standard size match. In Figure 4.6 the three manufactured interface parts (G2), (H), and (I2) are presented. Finally, the enveloping box and tube support (J)-(L) can be viewed in Figure 4.7, showing the completely assembled prototype.



Figure 4.5: The small manufactured parts that are part of the instrument tip design, including parts A - G1 and I1.



Figure 4.6: The three parts of the control interface, that allow reloading and triggering of the mechanism, including parts G2, H, and I2



Figure 4.7: The complete assembled prototype.

The assembly of the complete prototype involved the creation of several permanent connections between parts (D) and (E), (E) and (J), (G1) and (G2), and (I1) and (I2). These connections were made with the help of Loctite 603 glue (Henkel AG & Co. KGaA, Düsseldorf, Belgium). Part (C) was not permanently connected to part (D), to allow easy exchanging of the indenter tip part (A). To assemble the prototype part (F) was inserted distally through part (J), (E) and (D), and subsequently part (G) was inserted similarly, which allows to push part (F) in its most proximal position. Following, the spring (B) could be placed proximally over the rod of part (F), the indenter tip (A) was screwed onto the tip of the rod, and part (C) could be placed onto part (D) to envelope parts (A), (B) and (F). Then, the control interface was placed, fitting part (H) distally to part (G2) by its screw thread and inserting part (I) distally as well. Finally, the box

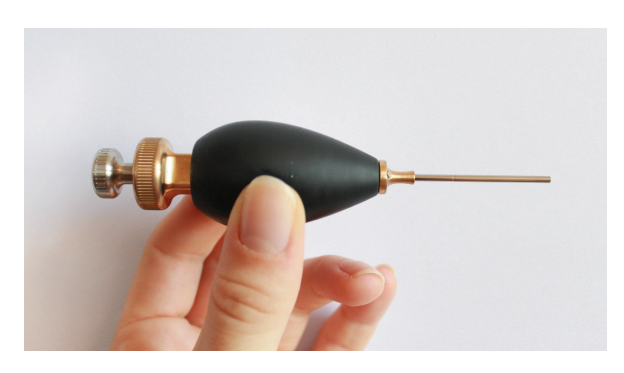


Figure 4.8: The prototype parts (A)-(I) and (L) assembled with a handgrip, providing a future view on a possible future clinical instrument.

top (K) and tube support (L) were placed in position on part (J), fastened with the help of M3 and M1.4 screws, respectively, and the guiding screw (M2) for the gripper positioning was inserted from below into the box (J).

In addition to the experimental prototype assembly, an assembly of the prototype was made with parts (J) and (K) replaced with a handgrip, to provide a view on a possible future clinical instrument. This assembly is shown in Figure 4.8.

5. EXPERIMENT

5.1. GOAL OF THE EXPERIMENT

The main goal of the experiment phase was to evaluate the performance and effectiveness of the developed instrument prototype. This goal was subdivided in two parts: (1) investigation of the mechanical performance of the instrument, and (2) evaluation of the effectiveness of the (variable) design to puncture CTO proximal caps. Within this chapter, the design and setup of the performed experiments will be described, based on the two experimental goals. Subsequently, the experimental results will be presented and discussed.

5.2. EXPERIMENT DESIGN

For the evaluation of the mechanical performance of the instrument, two experimental measures were defined: indenter momentum (p) and impact peak force (F_{peak}) . These measures have been validated separately. For the investigation of the puncture effectiveness of the impact method and the associated instrument, an experimental setup was configured with different indenter tip shapes striking onto CTO models, to attempt fracturing. Furthermore, a study to compare the instrument performance in air and liquid was performed and the dynamical CTO model behaviour was analysed. Within the following sections, details of the experimental setup and facility will be provided. The

described experiment designs have been developed with the help of small pilot tests, which were performed for each of the experiments, to improve the initial planned facilities and setups.

5.2.1. Indenter performance

The indenter momentum was defined to be the main objective mechanical performance measure for the instrument. Due to the constant indenter mass, momentum variability was only related to the variation of indenter velocity. Therefore, the main experimental setup to evaluate indenter performance consisted of velocity measurement. The peak force of the impact brought by the indenter onto an object, that is related to the indenter momentum, was determined as second performance measure. This measure was used to evaluate performance consistency, since this could not be performed with velocity measurement due to the limited availability of the velocity measurement facility.

To investigate the influence of friction and actuation force on mechanical performance, it was decided to include two variables within the setups of velocity and peak force measurement: strike object distance and spring compression distance. The strike object distance influences the length of the free flight of the indenter, throughout which the indenter dynamics are only affected by friction forces. The spring compression distance is directly coupled to actuation force, influencing the level of acceleration of the indenter. For the investigation of instrument performance consistency over time it was decided to perform peak force measurements in the initial experimental phase, as well as at the end of the experimental phase.

Facility

During the measurements of indenter velocity and impact peak force, the prototype was suspended vertically in a construction of *Thorlabs optomechanics* (Thorlabs, Inc., Newton, NJ, USA), including a solid aluminium breadboard (*MB3030/M*), a construction rail (*XE25L375/M*), and a single-axis translation stage (*PT1/M*). With an intermediate plate construction, the prototype was fastened on the translation stage, with its instrument tip pointing downwards. It is argued that the effect of gravity within the experiment can be neglected, since the estimated gravity force is 3 orders of magnitude smaller than the maximum spring force. This experimental facility composition is illustrated in Figure 5.1.

For the velocity analysis, High Speed Videos (HSVs) of the indenter strike were made with a *Photron Fastcam APX-RS* (Photron USA, Inc., Tokyo,

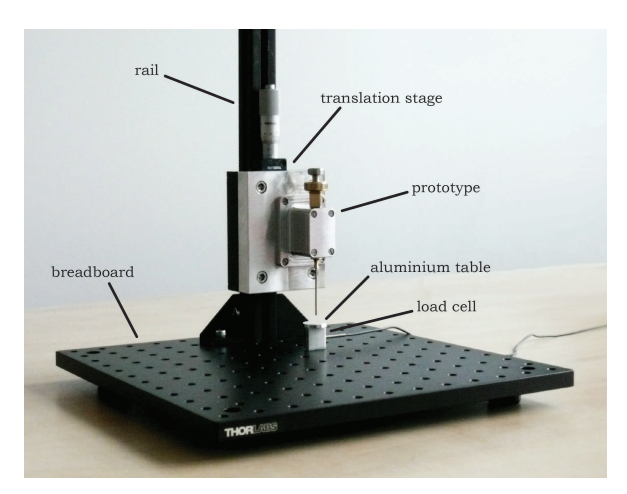


Figure 5.1: The experimental construction of *Thorlabs optomechanics* (including breadboard, rail, and translation stage), in which the prototype is suspended with the instrument tip pointing downwards onto a miniature load cell, on top of which a small table was fastened to capture the indenter strike.

Japan) at a frame rate of 10 kHz. Subsequently, the obtained images were processed with the associated software package *Photron FASTCAM Viewer v3.5.3*. The indenter mass measurement, to be combined with the velocity measures for the calculation of momentum, was performed with a high precision balance (*Mettler PJ360 DeltaRange*, Mettler-Toledo International Inc., Columbus, OH, USA).

The peak force was measured with a miniature S beam load cell (*LSB200, FSH00103*, FUTEK Advanced Sensor Technology, Inc., Irvine, CA, USA), connected to an analogue signal conditioner (*CPJ RAIL*, SCAIME, Annemasse, France) and a data acquisition system with a sampling rate set to 50 kHz (*NI USB-6211*, National Instruments Corporation, Austin, TX, USA). This system was controlled through *LabVIEW 2014* (National Instruments Corporation, Austin, TX, USA). The load cell was fastened onto the *Thorlabs* breadboard by means of a screw. To capture the impact strike of the indenter, a small aluminium table was fastened on top of the load cell.

Setup

The experimental variables (strike object distance and spring compression distance) were combined to form a total of 6 different mechanical settings. The 2 selected strike object distances were 1 mm and 3 mm from the instrument tip. The minimal distance of 1 mm was selected to still allow indenter bounce. The maximum distance of 3 mm was selected to be just below the maximum indenter reach (designed at 4 mm) before being blocked internally. The velocities at the 2 distances were obtained from one video capture, with maximized object distance. The spring compression variation included distances of

approximately 3.5 mm (maximum load length of the spring), 2.8 mm (medium compression, 360° twist of the handgrip), and 2.0 mm (minimal compression, 720° twist of the handgrip). The latter was found to be near the critical minimum for the indenter to reach an object at 3 mm distance during pilot tests, and was, therefore, selected as minimum. For each of the mechanical instrument settings, 5 measurement repetitions were made. Because of unknown instrument robustness, it was decided not to perform a larger amount of repetitions.

The final velocity evaluations were performed with manual analysis of the captured HSV images, by means of computing the travelled distance and elapsed time between subsequent images of the video capture. For each of the peak load measurements, 2 seconds of data was sampled that encompassed the indenter strike. The data was subsequently processed with *MATLAB 2013b* (The Mathworks, Inc., Natick, MA, USA), to correct for a measurement offset and to find the peak force (highest value measured) within each of the data sets.

Additional performance evaluation in fluid

To investigate the functioning of the instrument in fluid, corresponding with the final clinical environment, an additional peak force measurement was performed. For this measurement, to be compared with the measurements in air, the described facility and setup of the impact peak force experiment was used, with one adjustment: the aluminium table receiving the indenter strike was replaced with an aluminium bucket filled with Blood-Mimicking Fluid (BMF) in which the instrument tip (~ 15 mm) was immersed. The BMF was made from glycerine and clear water, which is a widely used mixture to resemble blood [37–39]. To mimic an estimated blood viscosity of 3.5 mPas [37, 38] it was decided to create a mixture of 25wt% glycerine (De Tuinen B.V., Beverwijk, NL) and 75wt% clear water, of which the viscosity was estimated to be between 3.1 and 4.0 mPas [40] ¹.

5.2.2. PUNCTURE EFFECTIVENESS

To validate the effectiveness of the instrument in puncturing proximal caps of heavily calcified CTOs, multiple CTO models were constructed. The choice for an artificial model was based on the highly limited possibility to test on real CTO lesions, which do not preserve after retracting from a body, according to an expert cardiovascular interventionist. Furthermore, the ability to compare the effectiveness of variable tip shapes is highly restricted with real CTOs, since the variability between CTO lesions can

¹Glycerine is a generally used name for pure glycerol as well as for a liquid mixture of glycerol and water. The presented estimation of viscosity is based on the assumption that the used glycerine contains a minimum of 75wt% glycerol.

be significantly large, providing an inconsistent test environment. Therefore, experimental CTO models were developed, which could be created in large numbers and with consistent characteristics. Different material models for the proximal caps were introduced to resemble the uncertain and variable CTO material properties.

With the help of the models, both effectiveness and efficiency of the prototype, to fracture material, could be evaluated, including the evaluation of various tip shape designs. It was decided to perform the experiment with maximized settings only (strike object distance of 1 mm and spring compression distance of 3.5 mm). It was argued, based on pilot study results, that testing with lower impact forces would only prove a trivial lower effectiveness and efficiency, which will be further discussed within the discussion section of this chapter.

Facility

The experimental facility for the puncture experiments consisted of the previously described *Thorlabs* construction, the developed CTO models, and the various tip shapes of the indenter (see Chapter 3.3.2). The CTO model was placed underneath the prototype tip and fastened to the breadboard of the *Thorlabs* construction with adhesive tape, to prevent small location shifts. This facility is shown in Figure 5.2.

The CTO model consisted of three basic parts: (1) a small circular container (26 mL), (2) surrounding tissue, and (3) a CTO proximal cap model, as illustrated in Figure 5.3. The circular container was filled with gelatine, representing the surrounding tissue, which is widely used in biomechanical studies to mimic human tissue. In this study the gelatine mixture was created with a weight percentage of 25wt% pure gelatine (Sheet gelatine, Dr. Oetker, Bielefeld, Germany) and 75wt% clear water, to get an estimated Young's modulus between 100 kPa and 130 kPa [41, 42] resembling that of cardiac muscle tissue. The procedure that was used to create the gelatine mixture is described in Appendix E. In its liquid form, the gelatine mixture was poured into the small containers, which were put in a specially made mould to create a Ø 10 mm notch of approximately 7 mm in depth within the centre of the gelatine volume during stiffening. This notch was created to surround the proximal cap model in an elastic environment as much as possible; completely submerging the proximal cap model within the gelatine was judged as impractical, because of, amongst others, the more difficult model production and decreased visibility of material fracture.

The CTO proximal cap models were made from plaster cast (SHERAALPIN Hartgips hellblau, SHERA

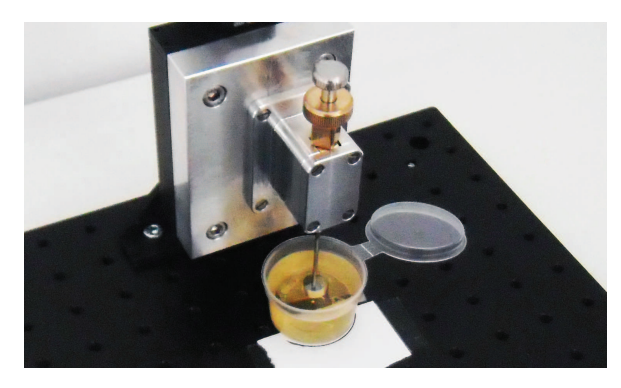


Figure 5.2: The complete experimental setup of the puncture effectiveness study, including the *Thorlabs* construction, the instrument prototype, and a CTO model.

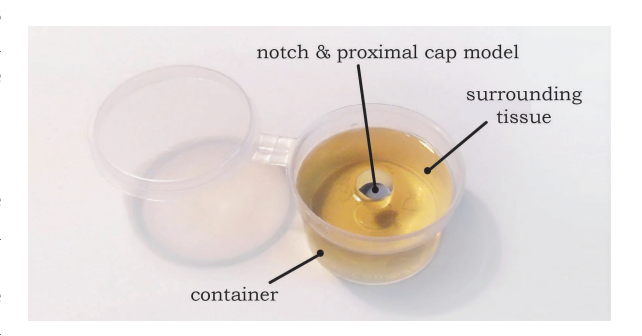


Figure 5.3: The complete CTO model, consisting of a small container filled with gelatine (resembling surrounding cardiac muscle tissue), in which a small slice of stiffened plaster cast mixed with gelatine/water (resembling the CTO proximal cap) is placed.

Werkstoff-Technologie GmbH & Co. KG) and the described gelatine mixture. These materials were selected to mimic the high calcium and collagen concentrations found in the proximal caps of heavily calcified CTOs. A first "basic" model was created with 75wt% plaster cast powder and 25wt% liquid gelatine mixture, in a Ø 10 mm circular slice of approximately 1 mm thick. Whereas global concentrations of calcium content within calcified CTOs are given lower than 75% [15], these concentrations are heterogeneously spread throughout the CTO, leading to higher local calcium concentrations. Therefore, the 75wt% of plaster cast was selected to represent a basic level of local calcification within a heavily calcified CTO. The model thickness of 1 mm was selected as a minimal thickness. Even though proximal caps may on average be 0.5 mm [43], moulding difficulties were experienced to produce homogeneous thinner models [44]. A highly similar proximal cap model was used and tested in an earlier study to resemble a real CTO quite closely, based on measured static penetration forces [44, 45]. Next to this basic model, a "soft", more elastic model (50wt% plaster cast powder and 50wt% gelatine mixture) and a "hard", more brittle model (77wt% plaster cast powder and 23wt% clear water) were developed, to represent the variable CTO material properties



Figure 5.4: Image of the several proximal cap models that were created of plaster cast and gelatine/water.

within the experiment. The detailed construction procedure of the proximal caps is given in Appendix E. The created proximal cap models are shown in Figure 5.4.

Setup

The final designed experimental setup for the effectiveness study included 54 trials, combined from the 3 material models (soft, basic, and hard proximal cap model), the 6 tip shape design (stamp, spherical, wedge, pointed, ringed, and spherical with guidewire passage), and 3 measurement repetitions. Even though a larger number of repetitions would be desired to increase the significance of the experimental results, it was argued that a larger experimenting time would increase the undesired effects of model variation on the collected data. To restrict those effects, it was decided to use models from one batch only, and to limit the experiment duration to 4 hours in total, preventing (large) influences from model hardening over time.

The main measure in the experiment was defined to be the number of indenter strikes necessary to puncture or fracture the proximal cap model. This measure was used to obtain a global classification of puncture effectiveness (binary classification; puncture versus no puncture), as well as an indication of efficiency in fracture performance (scale classification; number of strikes). The maximum number of strikes per trial was set to 10. Additionally, the development of dents, fracture lines, and material openings in the CTO models during the experiments were visually observed to identify the form of material deformation and puncture. To evaluate the overall effectiveness of the impact method on the different materials. the results from different tip shapes have been grouped together, resulting in data analysis of 3 groups with 18 performed trials. The effectiveness of the different indenter tip shapes, however, was judged per material group separately, since it was argued that the effectiveness of tip shapes is material dependent (see Chapter 2.4).

Additional dynamical behaviour study

In addition to the described effectiveness study, an exploratory study to the dynamical behaviour

of the CTO model upon indenter strike was performed, to evaluate the occurring collision scenario (feeding-back onto the collision theory described in Chapter 2.4). For this study, HSVs were made of the indenter striking onto a CTO model, for which the facility described for the indenter velocity measurement was supplemented with a CTO model. The finally used CTO model in this experiment was slightly adjusted from its original form, for the purpose of improved light exposure during the recordings: the proximal cap models were placed on top of a squared block of the surrounding tissue gelatine mixture. The indenter velocity after bouncing on the proximal cap model, as well as the maximum displacements within CTO model, were manually derived from the captured HSV images. These measures were subsequently used to investigate the distribution of energy dissipation during collision between indenter and CTO model.

5.3. RESULTS

Within this section, the retrieved experimental results will be presented separately for each of the experimental setups. A discussion of the results will be provided in the subsequent section. The complete sets of collected data are provided in Appendix F.

Indenter momentum

An impression of the images captured by the high-speed camera for the velocity measurement is given in Figure 5.5. The average indenter velocities (mean (range), n = 5), analysed from the HSV images, and subsequently calculated momenta ($p = m \cdot v$), for each of the earlier specified variable mechanical settings, are given in Table 5.1.

The maximum measured velocity, generated with maximized actuation force, was found to be 3.4 m/s. Together with the measured indenter mass of 0.39 grams, a maximum momentum of 1.33 mNs was found. It was observed that decreased compression spring distance and increased strike object distance both caused a decrease of measured velocity. In the case of minimal spring compression distance (2.0 mm), the indenter did not reach the ultimate position (3 mm) during the HSV capturing experiment.

Impact peak force

In this section, the results of both peak force measurements, executed in the beginning and end of the testing phase, are presented. A visualization of the measured load scenarios is given in Figure 5.6. The figure includes all indenter strikes captured during the secondary test. The derived average peak forces (mean *(range)*, n = 5) are presented in Table 5.2.

In both the primary and secondary test, the maximum peak force of the impact strike was measured to be around 19 N, generated with



Figure 5.5: Impression of the captured HSV images of an indenter strike with a spring compression distance of $3.5~\mathrm{mm}$.

Table 5.1: Results of the velocity measurement (mean *(range)*, n = 5) and momentum calculation ($p = m \cdot v$), for the different mechanical settings. The mechanical settings are given as *object distance | spring compression*, in the first column.

	v [m/s]	p [mNs]
1 mm / 3.5 mm	3.4 (3.3 - 3.6)	1.33
3 mm / 3.5 mm	3.0 (2.8 - 3.2)	1.17
1 mm / 2.8 mm	2.2 (2.1 - 2.3)	0.86
3 mm / 2.8 mm	1.3 (1.1 - 1.5)	0.51
1 mm / 2.0 mm	1.0 (0.9 - 1.0)	0.39
3 mm / 2.0 mm	-	-

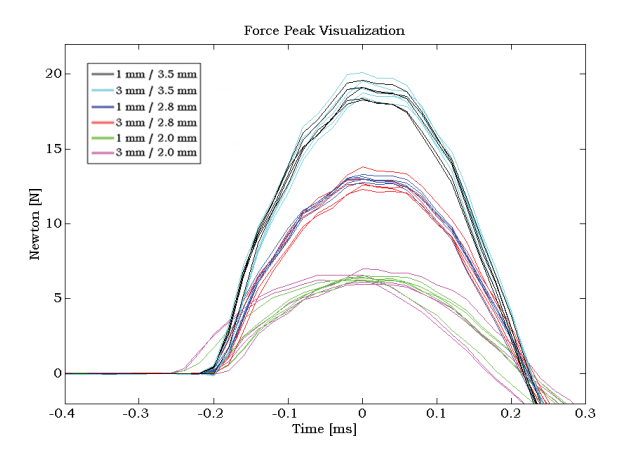


Figure 5.6: The load scenario around the peak force application measured during the secondary test. The colours represent the associated mechanical setting of the instrument, given as *strike object distance/spring compression distance* within the legend. For each indenter strike, represented by one line, the maximum value is plotted at time 0. The horizontal shift of 3 lines (2 pink, 1 green) is caused by a slightly delayed peak force in the load scenario.

Table 5.2: Results of the peak load measurement (mean (range), n = 5) for the different mechanical settings, which are given as *object distance | spring compression* in the first column.

	F _{peak} 1st [N]	F _{peak} 2nd [N]
1 mm / 3.5 mm	18.7 (17.7 - 19.8)	18.9 (18.3 - 19.6)
3 mm / 3.5 mm	18.6 (18.0 - 19.6)	19.2 (18.5 - 20.1)
1 mm / 2.8 mm	12.4 (12.0 - 12.9)	13.0 (12.8 - 13.3)
3 mm / 2.8 mm	11.2 (10.05 - 12.2)	12.9 (12.3 - 13.8)
1 mm / 2.0 mm	4.5 (4.1 - 5.1)	6.4 (6.2 - 6.5)
3 mm / 2.0 mm	2.5 (1.6 - 3.1)	6.4 (6.0 - 7.0)

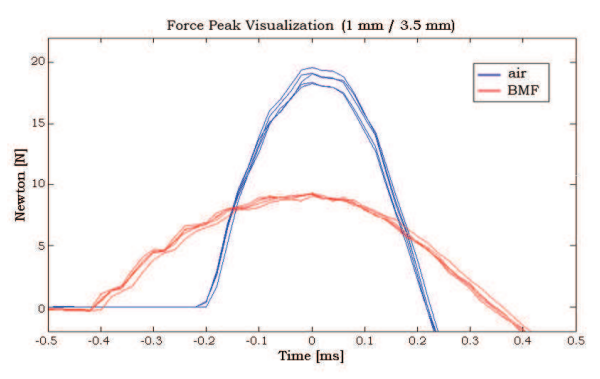


Figure 5.7: The load scenario around the peak force application of the indenter onto the load cell, for measurements in air (blue lines) and BMF (red lines) with maximized mechanical settings (1 mm object distance and 3.5 mm spring compression distance). Each of the lines represent one indenter strike.

Table 5.3: Results of the peak force measurements (mean *(range)*, n = 5) in air (secondary test) and in BMF, for the different mechanical settings given as *object distance | spring compression distance* in the first column.

	F _{peak} <i>air</i> [N]	F _{peak} BMF [N]
1 mm / 3.5 mm	18.9 (18.3 - 19.6)	9.2 (9.1 - 9.3)
3 mm / 3.5 mm	19.2 (18.5 - 20.1)	7.9 (6.9 - 8.4)
1 mm / 2.8 mm	13.0 (12.8 - 13.3)	5.8 (5.4 - 6.1)
3 mm / 2.8 mm	12.9 (12.3 - 13.8)	4.1 (3.1 - 4.7)
1 mm / 2.0 mm	6.4 (6.2 - 6.5)	2.4 (2.1 - 2.6)
3 mm / 2.0 mm	6.4 (6.0 - 7.0)	0.7 (0.4 - 1.6)

maximized actuation force and independent of strike object distance. For reduced spring compression distances, the peak force decreased. Differences between the primary and secondary test were observed only for reduced spring compression distances, in which the secondary tests show higher average peak loads for similar settings. Moreover, a slight influence of strike object distance was observed in the primary test, whereas the secondary test suggests independency of this variable.

Performance in fluid

A comparison of the load scenario in air (secondary test) and in liquid is visualized in Figure 5.7, showing the recorded peak forces for the maximized mechanical settings (1 mm object distance and 3.5 mm spring compression distance). The measured impact forces (mean *(range)*, n = 5) with the instrument tip immersed in BMF are given in Table 5.3, next to the earlier presented (secondary) measurements in air. It was observed that the peak force measured in BMF, compared to air, is reduced with a factor of 0.5 approximately. Moreover, the strike object distance was observed to be of larger influence on the measurements in liquid, compared to the measurements in air.

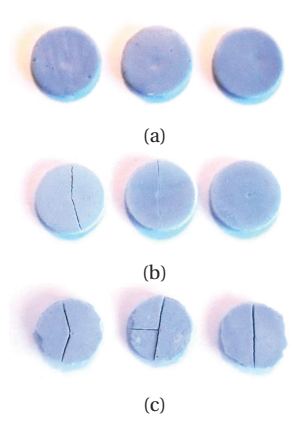


Figure 5.8: Typical resulting proximal cap models after striking the indenter multiple times onto it. The shown models were struck with the spherical indenter tip shape, on (a) the *soft* model (10 strikes), (b) the *basic* model (from left to right: 4, 5, and 10 strikes), and (c) the *hard* model (from left to right: 3, 3, and 2 strikes).

Table 5.4: Measured puncture effectiveness of the indenter (all tip shapes combined) for the 3 different material models of the proximal cap. 'Puncture' = number of punctures achieved, 'Success' = puncture success rate, and 'Strikes' = average number of strikes of the success cases (mean (range), n=13 and n=17 for the basic model and hard model, respectively).

	Puncture	Success	Strikes
Soft model	0 / 18	0 %	
Basic model	13 / 18	72 %	7.3 (4 - 10)
Hard model	17 / 18	94 %	3.4 (2 - 8)

Overall puncture effectiveness

The thicknesses (mean *(range)*, n=18) of the proximal cap models were measured to be 1.14 *(1.09 - 1.18)* mm, 10.8 *(0.90 - 1.24)* mm, and 1.24 *(1.21 - 1.27)* mm, for the *soft*, *basic*, and *hard* models, respectively. Some typical results of the proximal cap puncture trials are visualized in Figure 5.8, presenting the proximal cap models struck with the *spherical* indenter. It shows that no puncture of the *soft* models was achieved and puncture of the *basic* and *hard* models was mainly formed by means of a complete fracture line over the diameter of the model.

The measured results of the overall puncture effectiveness study are given in Table 5.4, showing the number of punctures achieved, the related success rate, and the puncture efficiency of all success cases (the average number of strikes necessary to achieve fracture), for the three material models. It was observed that both the puncture effectiveness and efficiency improved with increased model hardness; the method and instrument worked least effective in puncturing the *soft* models and were most effective and efficient in fracturing the *hard* models.

Tip shape effectiveness

The complete set of results of the effectiveness study, categorized for the different indenter tip shapes, is given in Table 5.5.

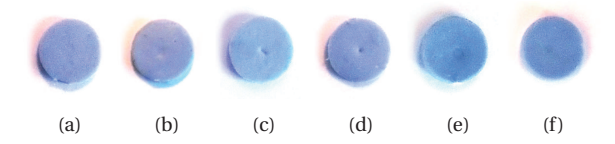


Figure 5.9: Typical resulting *soft* proximal cap models, after striking the indenter 10 times onto it. The shown models were struck with the (a) *stamp* indenter, (b) *spherical* indenter, (c) *wedge* indenter, (d) *pointed* indenter, (e) *ringed* indenter, and (f) *spherical indenter with guidewire passage.*

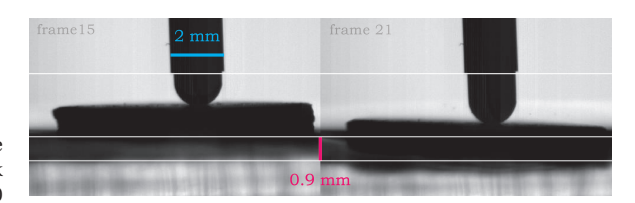


Figure 5.10: A visualization of the analysis of HSV images to derive maximum CTO displacement of the non-fractured *hard* model.

It was observed that the indenter strikes may leave an imprint of plastic material deformation on the *soft* model, but do not penetrate the model within 10 attempts. The imprinted soft models are presented in Figure 5.9, in which it is shown that the *wedge* indenter and *pointed* indenter typically left the most clearly visible and deep imprint (Figure 5.9 (c) and (d)), and the *stamp* indenter the least visible imprint (Figure 5.9 (a)).

The data of the experiments on the *basic* model did not show convincing results to point out one or more of the tip shapes as most or least effective. It was observed that the variability in puncture success and efficiency was quite large within the groups.

Finally, for the *hard* model it was observed that the *pointed* indenter was typically less effective and efficient to fracture the model, in comparison to all other tip shapes. The only failure case occurred with the pointed tip shape. Moreover, in the success cases (n = 2) this indenter needed 8 strikes to fracture the model; much more than the average of 2.7 strikes of the remainder 5 tip shapes (n = 15).

Dynamical model behaviour

The analysed average velocity of the indenter, after bouncing from the proximal cap model, was determined to be approximately $0.5 \, \text{m/s}$ in the cases the proximal caps did not fracture (n=7). No differences were observed in the bounce velocities for the different proximal cap models. A slight increased velocity of $0.8 \, \text{m/s}$ was observed for the cases in which the hard proximal cap model was fractured (n=2). In Figure 5.10 a visualization of the CTO displacement measurement is shown. The maximum displacement of the proximal cap models, in case no fracture occurred, was observed to be approximately $0.9 \, \text{mm}$ from its original location (n=7). An increased displacement was observed for the fractured (hard)

Table 5.5: Measured number of strikes to cause fracture of the proximal cap models, upon strikes of the indenter with different tip shapes (maximum number of strikes is 10; > 10 represents puncture failure). The tip shapes are presented in the top row, with "Spherical II" representing the spherical indenter with guidewire passage. The model type and test number (n = 3) are given in the left two columns.

		Stamp	Spherical	Wedge	Pointed	Ringed	Spherical II
Soft	I	> 10	> 10	> 10	> 10	> 10	> 10
	II	> 10	> 10	> 10	> 10	> 10	> 10
	III	> 10	> 10	> 10	> 10	> 10	> 10
Basic	I	9	4	6	> 10	5	> 10
	II	> 10	5	7	7	10	9
	III	6	> 10	5	> 10	9	10
Hard	I	2	3	3	8	2	3
	II	3	3	3	8	2	2
	III	5	2	3	> 10	2	3

proximal cap models, with a maximum of 1.4 mm measured.

5.4. DISCUSSION

Within this section, the results presented within the previous section will be interpreted and discussed. The discussion is separated for each of the measures. The final implication of the experimental results on the conclusion and prospects of the complete study will be described in the next chapter.

Consistency

The comparison of the primary and secondary peak force measurements has shown a slight inconsistency of instrument performance over time, for the measurements with non-maximized actuation force. This observed inconsistency may predominantly be explained by effects of wear, and possibly by a variable distribution of lubricating oil within the instrument.

This inconsistency was also observed within the HSVs, where the indenter did not reach the ultimate 3.0 mm object distance, which it did during the experiments with the load cell. Due to the close follow up of the velocity and primary peak force measurements, wear might not be the main factor of influence on this inconsistency. Rather, it is thought that the effects of lubricating oil distribution and uneven heating of the prototype parts (due to strong lights used for the HSV capture) play a larger role, influencing frictional effects.

The inconsistency within experimental setups, rather than between the setups, was observed to be sparse. However, a real significant indication of this variability could not be deduced, due to the limited number of repetitions performed within each of the tests. The earlier applied argument of unknown instrument robustness, for small measurement setups, not necessarily restricted the possibility of performing a consistency experiment with more repetitions at the end of the experiment phase.

This could have provided a valuable and significant measure of consistency, to exclude the influence of variable instrument performance on, for example, measured differences within the effectiveness study. However, the performance of such a consistency experiment was limited by time availability and not judged as a critical factor within this explorative study, since there were no indications of performance inconsistency (at maximized spring compression).

Indenter momentum

The maximum velocity was estimated to be 6 m/s at the moment the indenter protrudes from the instrument; frictional effects neglected. comparing this estimation with the measured maximum velocity of 3.4 m/s, it may be concluded that frictional effects play a large role within the mechanism. The potential spring energy (E_p = $\frac{1}{2} \cdot k \cdot x^2$, spring constant k = 1.3 N/mm, spring compression distance x = 3.5 mm) was calculated to be 8.0 mJ and the kinetic energy of the indenter at the start of its free flight $(E_k = \frac{1}{2} \cdot m \cdot v^2)$, indenter mass m = 0.39 gr, indenter velocity v = 3.4 m/s) was found to be 2.3 mJ. Based on these numbers, the mechanism efficiency ($\eta = \frac{E_k}{E_p}$, neglecting the kinetic energy in the spring) is approximated to be 28%. Potentially, a higher efficiency may be realizable by reducing frictional effects. This could, for example, be achieved by reducing the contact surface between the moving parts (the indenter and spring) and the surrounding catheter tube, or by a different material choice for these parts.

Impact peak force

For the peak force measure, it was expected to see more variability between the measurements with similar spring compression distances, but different strike object distances. The results of the secondary peak force measurements suggest that, after a period of initial mechanism wear, the friction effects during free flight of the indenter (in air) are negligible. Based

on this finding, the main mechanism friction, leading to the low mechanism efficiency, may most probably be assigned largely to losses within the spring itself and losses due to friction between the spring and the catheter tube. The higher effect of spring-catheter friction, compared to indenter-catheter friction, may be explained by the noticed curvature of the spring when compressed, which causes increased frictional forces between the spring and the catheter tube.

Furthermore, it was expected to see only a very thin (short time) peak in the force-time diagram, with one outstanding peak value. The resulting force-time diagram shows more of a sinusoidal load profile (phase ~ 0.8 ms) damped over time (~ 100 ms). This measured profile may be explained by the influence of the relatively large inertia of the load cell and aluminium table that captured the impact load, compared to the inertia of the indenter. Anticipating on the discussion of the peak force measurements in fluid, an increased phase and damping time of the load profile was observed, compared to the measurements in air. This can be explained by the larger inertia of the fluid filled bucket, compared to the table used during the measurements in air.

Finally, it was observed that the indenter strikes caused plastic deformation of the aluminium table (small dents), from which is may be concluded that the actual peak force might be slightly higher than the measured force, due to the dissipated deformation energy.

Performance in fluid

Looking at the peak force measurements within fluid (BMF), a large decrease of peak force was observed, compared to air. This decrease is caused by the increased resistance to the movement of the indenter and spring, due to the higher environmental viscosity. This viscous friction may be categorized by external friction, acting only on the protruding indenter tip, and friction acting on all moving parts within the instrument (the back part of the indenter and the spring). For a future instrument design, to be used within blood-filled arteries, the increased external friction may be inevitable to account for. Yet, obstructing the fluid to flow into the instrument tip may prevent the decelerating effect of internal friction.

Overall puncture effectiveness

Before discussing the results of the effectiveness study, it must be noted that due to the limited experimental setup, the presented results do not comprise significant measures. Moreover, it is suggested that the influence of proximal cap model variability should be considered while drawing conclusions, since it was observed that with the basic model, the most efficient fracture trial was correlated

to the thinnest proximal cap model, in all of the 6 tip shape categories. Even though it was attempted to create models with highly consistent characteristics, slight variation could not be precluded with the used materials, tools, and production procedure. The use of, for example, a vacuum mixer and a mould for individual proximal cap model production is suggested for future experiments, to further diminish the effect of model variation on obtained results. However, it was argued to be outside the scope of this explorative design study to invest in this production procedure.

Despite of the suggested uncertainty, it can be concluded that the impact method effectiveness is highly material dependent. The developed instrument prototype was effective to fracture the brittle material models, but ineffective to puncture the more elastic soft models. This may be explained by the difference in energy needed to form fracture when comparing brittle and tough materials. Material strength and toughness are linked to the amount of force and energy needed to created fracture, respectively. The brittle material (high strength, low toughness) may therefore be highly vulnerable to impact load, which provides high force but does not provide much energy, due to the short load period. A tougher, more elastic model (even with lower material strength compared to the brittle models) is able to resist fracture through its ability to absorb energy from the impact loads by deformation (elastic and plastic). This finding is in accordance with the fact that the impact method is more widely used to fracture hard and brittle material, rather than elastic material; for example the hammer drill that is specially designed for drilling holes in concrete walls.

The efficiency of the method, from the perspective of fracture formation, was observed to be non-optimal, as in none of the trials the proximal cap model was fractured after one indenter strike. Since it was argued that lower momentum of the indenter could not lead to increased effectiveness or efficiency of the fracture formation, effectiveness studies with decreased spring compression forces, or increased object distance, were precluded. Rather, it would be interesting to experiment with increased On the contrary, from medical momentum. perspective, increased momentum may induce undesired increased forces onto the arterial wall. Since, within this study, optimality is a consideration between fracture effectiveness and medical safety, it is difficult to draw conclusions about optimal efficiency of the method.

Finally, it must be noted that the measured effectiveness and efficiency might give a conservative impression of the performance on real CTOs. This thought is underpinned with the argument of

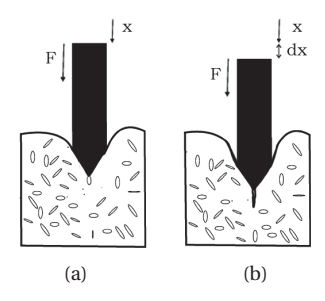


Figure 5.11: Elastic material fracture upon needle insertion with (a) an initial phase of elastic tissue deformation, and (b) material rupture at the tip of the needle. The applied force is given as F, the needle displacement direction with x, and the displacement between images (a) and (b) as dx. Figure adjusted from [46].

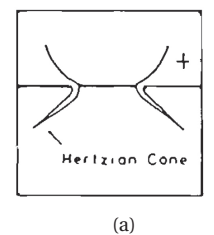
increased thickness of the developed proximal cap models, compared to the reported average thickness of proximal caps of CTOs, which is most likely associated with higher resistance to full penetration. However, due to overall simplification of the created models compared to a real CTO, it is difficult to translate the presented experimental findings to the clinical situation with certainty.

Tip shape effectiveness

For the evaluation of the effectiveness of the different tip shape designs, similarly as for the overall effectiveness, it must be noted that from the performed study no definite conclusion can be drawn. Nevertheless, some differences were observed, that can be used as guidelines for a future design study.

For the soft models, it was expected to see a better puncture performance with the sharp tools. Even though no puncture was achieved, the sharpest tools (pointed and wedge indenter) did leave the most clearly visible imprint. On the contrary, the pointed indenter showed least effective results in fracturing the hard models. Feeding back onto fracture formation theory, this finding can be clarified.

For needle insertion in soft tissue, the fracture process can be described as follows: (1) tissue elastic deformation (Figure 5.11 (a)), (2) material rupture at the tip of the needle (Figure 5.11 (b)), and (3) propagation of the crack (rupture) in response to needle displacement [46]. It is known that the rupture force (step 2) decreases with increased needle sharpness [46, 47]. This decreased force may be coupled to an increased level of material stress with decreased area of the force application (as argued in Chapter 2.4). With this theory in mind, the inability of the indenter to penetrate the soft models may not only be explained by ineffectiveness of impact load; also the non-optimal tip shape may be used as argument. It is expected that a sharper and thinner indenter tip, compared to the developed pointed indenter, would have been more effective. However, such a shape was precluded from the



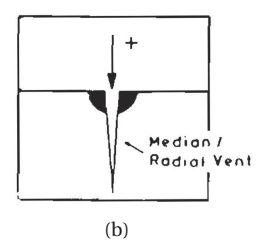


Figure 5.12: Evolution of cracks in rocks upon indentation with (a) a spherical indenter and (b) a pointed indenter. The spherical indenter causes cracks that propagate in radial direction of the indenter, known as the "Herzian crack". The pointed indenter causes a main crack in the axial direction of the indenter. Figures taken from [36].

experiment, due to the associated increased risks of arterial wall puncture.

The process of brittle fracture (for rock breakage) by impact load is given as follows: (1) formation of a crushed zone with numerous micro-cracks (pulverization), (2) dominant crack formation, (3) spontaneous and rapid crack propagation, and (4) chipping of the material [48]. The dominant crack formation (step 2) is reported to be dependent on indenter shape [36, 48], which is well illustrated in Figure 5.12 showing fracture formation as a result of indentation with a spherical and pointed tip shape. The blunt indentation shape shows crack formation in radial direction, whereas the pointed indenter load results in main crack formation in the axial direction of the indenter. Considering the formation of a complete fracture line over the diameter of the proximal cap models, the formation of main cracks in radial direction may explain the more efficient fracturing of the thin and wide models by non-pointed indenters.

Due to the uncertainty of the material characteristics of CTOs, and the limited experimental setup, it is difficult to suggest one of the tip shapes as most suitable for a future instrument. Nonetheless, it was concluded that the pointed indenter may be least appropriate for the application. Moreover, the trials suggest that the "open" shapes (the ringed and spherical indenter with guidewire passage) do not perform inferior to the different "closed" shapes (stamp, spherical, and wedge indenter).

Dynamical model behaviour

A typical finding of the dynamical behaviour evaluation is the increased bounce velocity of the indenter and model displacement that was observed in the cases the indenter strike actually fractured a proximal cap model. For the increased displacement it was argued that tilting of the two parts of the proximal cap model after fracturing has led to a more concentrated distribution of the impact force on the gelatine. With a constant energy input, a decreased area of impact may be associated

with larger displacements. Additionally, it may be argued that in the case of fracture a different distribution of energy dissipation occurs, compared to a non-fracture case, influencing the displacements and velocities of both the model and the indenter.

Furthermore, the observed maximum displacements within the CTO model during this study (1.4 mm) were found to be lower than for static loading measurements. Derived from the data of the study by Kassing et al. [44], the displacement of the proximal cap of a highly similar CTO model, induced by an almost static (0.1 mm/s) guidewire load, was found to be 2.1 mm on average (n = 4) with a maximum of 2.7 mm measured. Moreover, the period of load application is much longer for the static load application, compared to the impact load. Therefore, it may be argued that the impact method does not increase the risks of environmental 'stretch' damage, compared to the conventional guidewire crossing method. However, this line of argumentation should be underpinned with evidence from future studies to arterial damage induced by impact loads, since high accelerations of the environment may have unknown other effects.

Feeding back on the collision scenarios presented in Chapter 2.4, the occurring collision scenario was observed to deviate from the presented "ideal scenario". The occurring collision was defined as highly inelastic, due to the large amount of kinetic energy lost during the indenter strike (kinetic energy before and after collision were determined at 2.2 mJ and 0.1 mJ, respectively). However, instead of the desired energy dissipation purely into material deformation and fracture, the energy dissipates to cause displacement of the CTO proximal cap model and vibrations within the surrounding tissue as well. Even though the method is effective to cause fracture, it is argued that the system dynamics of the designed indenter are not optimal. Therefore, future studies are needed to investigate the optimization of the collision scenario, where a higher indenter velocity may possibly lead to more optimal use of the CTO inertia and environmental damping during collision.

Conclusion

In summary, the performance of the instrument with maximum spring compression was found to be relatively consistent, with a measured maximum indenter velocity of 3.4 m/s, momentum of 1.3 mNs, and peak force of approximately 19 N. The puncture effectiveness of the indenter strikes was observed to be high for hard and brittle material models, but limited for more elastic and tough models. Even though the obtained results do not provide a definite conclusion, due to the limited setup of the effectiveness study, it is

suggested that a pointed indenter tip shape is least appropriate for the application. The efficiency of the designed mechanism was found to be low (28%), which may be increased by means of, for example, reducing the frictional surface areas between the moving parts (indenter, spring) and the catheter tube. Furthermore, a highly reduced instrument performance in liquid was observed, to be prevented or accounted for in a future instrument design. Finally, it was observed that a reasonable amount of the indenter kinetic energy dissipates into environmental movement, nonetheless, fracture of the basic and hard proximal cap models occurred by the formation and growth of cracks upon multiple indenter strikes.

6. DISCUSSION

Throughout this study it has been explored if the described "impact method" shows potential to be developed into an endovascular instrument that could aid to increase the success rates of PCI for CTOs. To evaluate this method its potential, both the instrument design and the functioning of the developed prototype will be discussed.

The developed prototype has illustrated the possibility to transform the impact method into a functional design within the limited dimensions of a PCI instrument. From several design iterations a fully functional instrument prototype was created, with the ability to apply multiple and consistent impact loads with the indenter, controlled from the distal end of the instrument. The developed reload mechanism and control interface were capable of grasping the indenter to compress the spring, locking the mechanism in a desired loaded position, and subsequently control the moment of indenter release. The complete prototype design allowed easy disassembling and interchange of the indenter tip. Moreover, the complete mechanism has proven to be highly robust, since throughout the experiment phase, which included an estimated 600 indenter strikes, no signs of weakness or failure were observed.

Furthermore, the instrument has shown to be effective in fracturing proximal cap models, placed within the elastic environment. It was observed that the effectiveness of the method is material dependent. The highest fracture effectiveness and efficiency was observed for the most brittle material models. In contrast, it has been discussed that the effectiveness of the impact method to fracture more elastic and tough material models is limited. Additionally, it was evaluated that a pointed tip shape worked least effective in fracturing brittle material models. For the several non-pointed indenter tip

shapes that were developed, no distinction could be made regarding efficiency or effectiveness on fracturing models; they performed similarly well in fracturing the brittle material models and they all have shown the ability to fracture basic models, with tougher characteristics.

It is argued that these study results support the potential of the impact method to cross heavily The proper functioning of the calcified CTOs. instrument, the easy disassembly, and the observed mechanism robustness provide a positive view on the instrument design. Further development of the instrument into a flexible clinical design, possibly with a reduced outer diameter, is a feasible next step in the development of an endovascular CTO crossing device. Moreover, the fracturing potential of the impact strike is regarded positive, considering the particularly hard proximal caps of heavily calcified CTOs. However, there are several points of discussion to take into account when reviewing the future prospects build upon this study.

Study limitations

The main limitation of this study is argued to be the large uncertainty around the material properties of CTOs and the lack of an effectiveness experiment with real CTOs. The highly limited information on the biomechanical properties of CTOs in literature, as well as in hospitals, bounds the possibility to translate the results of the performed effectiveness study to the clinical situation. It is reasoned that for the most heavily calcified CTOs, in which high calcium concentrations account for brittle characteristics of the CTO proximal cap, the instrument may be developed into a great tool to facilitate crossing. On the contrary, the existence of high concentrations of collagen, not rarely correlated to high material toughness, is believed to restrain the potential of creating fracture by means of impact load. It is, therefore, presumed that the effectiveness of the impact load application will be largely variable between CTO lesions due to variability of material But the main and unanswered characteristics. question remains how broadly the method is really effective to facilitate CTO crossing that cannot be achieved by means of the current tools used during PCI. Also, the effects of the impact strikes on blood vessel damage are still uncertain due to the lack of experimenting in the clinical situation.

Another constraint of this study is the limited validity of the presented experimental results on instrument performance and effectiveness, due to the minimal number of measure repetitions. Even though this study provides initial insights in the performance of the developed prototype and its possible potential to fracture proximal caps of CTOs,

more extensive experiments are needed to transform these findings into definite answers. The explorative character of the study, covering theory, instrument design, and a wide range of experimental evaluations, was selected with the main goal of investigating if the impact method is generally valid and shows potential for further investment in the form of research and development; this study approach has provided a very broad range of insights, but it has limited in-depth evaluation in the different directions.

Experimental recommendations

Most importantly, it is recommended that an investment will be made to perform studies on real CTOs at short notice, to validate the actual effectiveness of the instrument to cross CTOs. It is believed that with the developed prototype, studies on, for example, animal tissue are certainly feasible from a mechanical point of view. Adversely, considerable investments need to be made to obtain and prepare the desired tissue and to gain ethical permission for such a study. This investment in a supplementary effectiveness study is depicted as a necessity for obtaining certainty about the potential effectiveness of the instrument for percutaneous revascularization of CTOs.

On the long term, it would be highly valuable to extend the research to biomechanical properties of CTOs and closely surrounding tissue. Quantification of, for example, material distribution, Young's moduli, and puncture forces of CTOs can be highly valuable to develop a representative CTO model that can be used in future experiments. Also, an investment in modelling of the complete case, for example by means of the finite element method (FEM), could be made. Both these efforts will lead to more clear guidance and validation possibilities for the design of PCI instruments for CTO treatment.

further evaluation of fracture Next tο effectiveness, the risks and side effects of the applied impact method in blood vessels should be mapped. The effects of possible damage, including vessel stretch, intimal damage, and arterial wall perforation, caused by the instrument are still largely unknown. Experimental trials have shown decreased displacement in the CTO models, compared to guidewire load, and effectiveness of blunt tip designs, with which the chances of arterial wall puncture may be reduced. However, the effects of the increased acceleration of the CTO and its environment have not been studied. Besides vessel damage, there are other medical risks to be evaluated, such as the risk of ischemic events. The impact method may cause the formation of CTO material chips, which could end up in the blood circulation and lead to new occlusion formation at other locations. This

evaluation of medical risks of the impact method should be incorporated in a future continuation of this project to supplement the guidelines for further development of the instrument and an associated procedure of use.

Finally, it is suggested that a time investment could be made to supplement the experimental results by means of additional experimenting with the available facilities. First of all, an effectiveness study with variable indenter mass and variable and increased velocity could be performed, to evaluate the most optimal indenter characteristics. It must be noted that for such an experiment a more accurate CTO model, or testing on real CTOs, is a necessity, to be able to draw conclusions; since the collision scenario is both dependent on indenter and CTO characteristics. Secondly, both the consistency measurements and the tip shape effectiveness studies could be performed with extended measure repetitions, providing the possibility to draw definite conclusions on the instrument its performance consistency and better distinguish the (non-pointed) tip shapes on fracture effectiveness.

Design recommendations

For the instrument, the most important redesign step should be focused on the transformation of the rigid design into a flexible clinical instrument. This transformation includes, evidently, the evaluation of suitable, biocompatible, materials for the instrument, but the largest challenge that is foreseen is the design of connections between desired rigid and flexible parts. Moreover, the compression of the spring within a flexible and bended catheter may cause compression and straightening of the catheter, as the axial spring stiffness increases and forces are applied on the catheter during this compression phase. These events may cause undesired pressure on the arterial wall and potentially lead to buckling of the catheter, most likely near the distal end of the spring. These effects should be evaluated and taken into account during the redesign process, for which a flexible but axial stiff catheter is suggested.

Furthermore, a diminished effect of mechanism friction may be desired within a future redesign, potentially leading to increased indenter velocity and instrument performance. As earlier discussed, the static and kinetic friction may be reduced by means of reduced contact surface area of the spring, indenter, and catheter, and possibly through smart material selection, to increase the mechanism efficiency. Additionally, it is important to prevent the inflow of blood into the mechanism to preclude the associated effects of viscous friction. Also, it may be possible to increase instrument performance by

means of increased actuation performance, rather than increased efficiency. The compression spring used within the developed prototype was found to be one of the stiffest off-the-shelve available springs in its dimension range, however, further acquisition to stiffer designs may be merited. Moreover, it may be investigated if the use of a longer compression spring (lower spring rate, similar force at maximum compression distance) could be applicable to generate higher indenter velocities.

Future vision

Despite the presented limitations of the study and the work that is still to be done before a real clinical application could emerge, it is believed that the impact method and associated instrument design does show potential for clinical application. Even, next to crossing coronary CTOs, applications may also be found in other fields of health care. An obvious alternative application would be to develop the instrument for crossing CTOs in peripheral arteries, in which similar crossing problems may occur as in coronary arteries, however, the geometrical design requirements for the instrument are less obstructive. A rather different application of the impact method may be found in microfracture surgery, in which cartilage is repaired by creating tiny fractures in bone. In current practice, mostly applied to the knee joint, these fractures are created by means of an awl. Due to the rigidness of this instrument, the reach within the knee joint is limited and undesired damage is caused during surgery. Potentially, the designed mechanism for impact load application could be transformed into a flexible instrument for microfracture surgery in confined accessible parts of the knee.

For the future of percutaneous revascularization of coronary CTOs, further development of the instrument with more functionality is foreseen. The complete CTO revascularization procedure consists of multiple steps, of which puncturing the proximal cap is only one. Other than moving through the resistant fibrous cap and subsequent complete CTO, also precise steering through the CTO and detection of correct intraluminal passage are mentioned as two important capabilities the ideal CTO crossing device should entail [17]. A possible necessary addition to the instrument is the creation of a lumen within the mechanism, through which other instruments can be interchanged. For example, an internally placed guidewire can be used to advance through the softer core of the CTO, after the proximal cap is fractured by the impact load. Also the insertion of a visualization aid (for example Optical Coherence Tomography (OCT) or Intravascular Ultrasound (IVUS)) might be possible, that could help in the detection of correct aiming and intraluminal passage. It is expected that when using this internal instrument as core part in the reload mechanism (Chapter 4.2, Figure 4.1, part I1), the redesign with a hollow core structure is feasible without large design challenges. Moreover, it is thought that this adjustment is feasible without compromising the puncture effectiveness, since the evaluation of the two indenter tip shapes with an open core has shown these are potentially just as effective as the more common closed indenter For precise steering through the CTO, including the aiming of the indenter onto the proximal cap, it is furthermore suggested that the instrument could be supplemented with a system to centre and fix its position within the blood vessel, with the help of, for example, a balloon extension, or with active steerability of the instrument tip.

Design challenges of potential function sharing and smart mapping of the design space will arise throughout the development process of such a multifunctional instrument. Nonetheless, an investment in creative engineering of PCI equipment may be a necessity for interventional cardiologists to be more successful in percutaneous revascularization of CTO lesions.

7. CONCLUSION

The low procedural success rates of endovascular revascularization of CTOs may largely be assigned to the inability to cross the hard proximal caps of heavily calcified CTOs due to guidewire buckling. To pursue improved CTO crossing ability, a new crossing method was sought for endovascular application. Through a process of theoretical modelling and analysis, the application of consecutive impact loads on the CTO was selected as most promising

method to puncture the fibrous cap of the CTO. An instrument consisting of a thin-walled tube enclosing an indenter, accelerated by a compression spring and actuated through a novel compliant reload mechanism, was developed and evaluated in several explorative experiments. The study results are positive regarding fracture effectiveness of heavily calcified proximal caps and potential development of a clinically applicable instrument. However, the lack of knowledge on CTO properties has limited the possibility to optimize the instrument design and to draw final conclusions on its effectiveness. More information on the biomechanical properties of CTOs, or an effectiveness experiment with real CTOs, is needed to facilitate the desired instrument optimization and conclusive evaluation. suggested to continue the research and development of the method, to transform the study results into a valuable contribution to the PCI treatment possibilities of coronary CTOs in time.

8. ACKNOWLEDGEMENTS

First of all, I would like to thank Paul Breedveld, for his support and guidance throughout this explorative design-study. Secondly, I would like to thank my daily supervisors Aimée Sakes and Paul Henselmans, for the enthusiasm and great effort in their support and guidance throughout this graduation project. Furthermore, I would like to thank David de Jager for his contribution to the development and manufacturing of the prototype. Finally, I would like to thank the department of Animal Sciences of Wageningen University, in particularly Johan van Leeuwen and Remco Pieters, for the opportunity and assistance to capture HSVs of the functioning prototype.

BIBLIOGRAPHY

- [1] C. A. Thompson, Textbook of Cardiovascular Intervention (Springer, 2014).
- [2] T. Brown, Atherosclerosis, in ACM SIGGRAPH 2009 Computer Animation Fesitval (ACM) pp. 18–18.
- [3] J. A. Finegold, P. Asaria, and D. P. Francis, *Mortality from ischaemic heart disease by country, region, and age: Statistics from world health organisation and united nations*, International journal of cardiology **168**, 934 (2013).
- [4] World health Organization, *The top 10 causes of death*, Retrieved March 15, 2015 from http://www.who.int/mediacentre/factsheets/fs310/en/.
- [5] G. W. Stone, D. E. Kandzari, R. Mehran, A. Colombo, R. S. Schwartz, S. Bailey, I. Moussa, P. S. Teirstein, G. Dangas, and D. S. Baim, *Percutaneous recanalization of chronically occluded coronary arteries a consensus document: Part i*, Circulation **112**, 2364 (2005).
- [6] J. A. Grantham, S. P. Marso, J. Spertus, J. House, D. R. Holmes, and B. D. Rutherford, *Chronic total occlusion angioplasty in the united states*, JACC: Cardiovascular Interventions **2**, 479 (2009).
- [7] American Heart Association, *Atherosclerosis*, Retrieved January 29, 2015 from http://www.heart.org/HEARTORG/Conditions/Cholesterol/WhyCholesterolMatters/Atherosclerosis_UCM_305564_Article.jsp.
- [8] Encyclopædia Britannica Online, *Atherosclerosis: Comparison of arteries*, (), retrieved February 10, 2015 from http://www.britannica.com/EBchecked/media/95216.
- [9] K. Sakakura, M. Nakano, F. Otsuka, K. Yahagi, R. Kutys, E. Ladich, A. V. Finn, F. D. Kolodgie, and R. Virmani, *Comparison of pathology of chronic total occlusion with and without coronary artery bypass graft*, European heart journal, eht422 (2013).
- [10] R. Waksman and S. Saito, Chronic Total Occlusions: A Guide to Recanalization (Wiley, 2013).
- [11] R. Jaffe, G. Leung, N. R. Munce, A. S. Thind, H. Leong-Poi, K. J. Anderson, X. Qi, J. Trogadis, A. Nadler, and D. Shiff, *Natural history of experimental arterial chronic total occlusions*, Journal of the American College of Cardiology **53**, 1148 (2009).
- [12] G. W. Stone, N. J. Reifart, I. Moussa, A. Hoye, D. A. Cox, A. Colombo, D. S. Baim, P. S. Teirstein, B. H. Strauss, and M. Selmon, *Percutaneous recanalization of chronically occluded coronary arteries a consensus document: Part ii*, Circulation **112**, 2530 (2005).
- [13] Encyclopædia Britannica Online, *Balloon angioplasty*, (), retrieved February 10, 2015 from http://www.britannica.com/EBchecked/media/95218.
- [14] I. Kinoshita, O. Katoh, J. Nariyama, S. Otsuji, H. Tateyama, T. Kobayashi, N. Shibata, T. Ishihara, and N. Ohsawa, *Coronary angioplasty of chronic total occlusions with bridging collateral vessels: immediate and follow-up outcome from a large single-center experience,* Journal of the American College of Cardiology **26**, 409 (1995).
- [15] J. R. Cho, Y. J. Kim, C.-M. Ahn, J.-Y. Moon, J.-S. Kim, H.-S. Kim, M. K. Kim, Y.-G. Ko, D. Choi, and N. Chung, *Quantification of regional calcium burden in chronic total occlusion by 64-slice multi-detector computed tomography and procedural outcomes of percutaneous coronary intervention*, International journal of cardiology **145**, 9 (2010).
- [16] D. Delaney, P. Johansson, and B. R. Constantz, *Catheter devices and methods for their use in the treatment of calcified vascular occlusions,* (2001).
- [17] G. W. Stone, A. Colombo, P. S. Teirstein, J. W. Moses, M. B. Leon, N. J. Reifart, G. S. Mintz, A. Hoye, D. A. Cox, and D. S. Baim, *Percutaneous recanalization of chronically occluded coronary arteries: Procedural techniques, devices, and results*, Catheterization and cardiovascular interventions **66**, 217 (2005).

- [18] W. Nichols, M. O'Rourke, and C. Vlachopoulos, *McDonald's blood flow in arteries: theoretical, experimental and clinical principles* (CRC Press, 2011).
- [19] P. B. Dobrin and J. M. Doyle, *Vascular smooth muscle and the anisotropy of dog carotid artery*, Circulation research **27**, 105 (1970).
- [20] A. B. Mathur, A. M. Collinsworth, W. M. Reichert, W. E. Kraus, and G. A. Truskey, *Endothelial, cardiac muscle and skeletal muscle exhibit different viscous and elastic properties as determined by atomic force microscopy*, Journal of biomechanics **34**, 1545 (2001).
- [21] Q.-Z. Chen, A. Bismarck, U. Hansen, S. Junaid, M. Q. Tran, S. E. Harding, N. N. Ali, and A. R. Boccaccini, *Characterisation of a soft elastomer poly (glycerol sebacate) designed to match the mechanical properties of myocardial tissue*, Biomaterials **29**, 47 (2008).
- [22] C.-K. Chai, A. C. Akyildiz, L. Speelman, F. J. Gijsen, C. W. Oomens, M. R. van Sambeek, A. van der Lugt, and F. P. Baaijens, *Local axial compressive mechanical properties of human carotid atherosclerotic plaques—characterisation by indentation test and inverse finite element analysis*, Journal of biomechanics **46**, 1759 (2013).
- [23] L. Yang, Mechanical properties of collagen fibrils and elastic fibers explored by AFM, Thesis (2008), department of Polymer Chemistry and Biomaterials, University of Twente.
- [24] F. Jelínek, G. Smit, and P. Breedveld, *Bioinspired spring-loaded biopsy harvester—experimental prototype design and feasibility tests*, Journal of Medical Devices **8**, 015002 (2014).
- [25] M. Lock, A Study of Buckling and Snapping Under Dynamic Load, Report (DTIC Document, 1967).
- [26] J. Bavosi, Artwork of human arterial system, (2013), retrieved October 24, 2014 from http://fineartamerica.com/featured/artwork-of-human-arterial-system-john-bavosi.html.
- [27] A. Avolio, *Multi-branched model of the human arterial system*, Medical and Biological Engineering and Computing **18**, 709 (1980).
- [28] Terumo Medica lCorporation, Azur peripheral hydrocoil embolization system, (2008), retrieved November 20, 2014 from http://www.terumois.com/administration/Collateral.aspx.
- [29] T. Sandgren, B. Sonesson, s. R. Ahlgren, and T. Länne, *The diameter of the common femoral artery in healthy human: influence of sex, age, and body size,* Journal of vascular surgery **29**, 503 (1999).
- [30] P. Boutouyrie, C. Bussy, P. Lacolley, X. Girerd, B. Laloux, and S. Laurent, *Association between local pulse pressure, mean blood pressure, and large-artery remodeling*, Circulation **100**, 1387 (1999).
- [31] S. Saito, H. Ikei, G. Hosokawa, and S. Tanaka, *Influence of the ratio between radial artery inner diameter* and sheath outer diameter on radial artery flow after transradial coronary intervention, Catheterization and Cardiovascular Interventions **46**, 173 (1999).
- [32] M. A. Kotowycz and V. Džavík, *Radial artery patency after transradial catheterization*, Circulation: Cardiovascular Interventions **5**, 127 (2012).
- [33] B.-S. Yoo, J. Yoon, J.-Y. Ko, J.-Y. Kim, S.-H. Lee, S.-O. Hwang, and K.-H. Choe, *Anatomical consideration of the radial artery for transradial coronary procedures: arterial diameter, branching anomaly and vessel tortuosity,* International journal of cardiology **101**, 421 (2005).
- [34] J. Dodge, B. G. Brown, E. L. Bolson, and H. T. Dodge, *Lumen diameter of normal human coronary arteries*. *influence of age, sex, anatomic variation, and left ventricular hypertrophy or dilation,* Circulation **86**, 232 (1992).
- [35] R. A. Lange and L. D. Hillis, Diagnostic cardiac catheterization, Circulation 107, e111 (2003).
- [36] H. Guo, *Rock cutting studies using fracture mechanics principles*, Thesis (1990), department of Civil and Mining Engineering, University of Wollongong.

- [37] K. V. Ramnarine, D. K. Nassiri, P. R. Hoskins, and J. Lubbers, *Validation of a new blood-mimicking fluid for use in doppler flow test objects*, Ultrasound in medicine & biology **24**, 451 (1998).
- [38] M. Y. Yousif, D. W. Holdsworth, and T. L. Poepping, *A blood-mimicking fluid for particle image velocimetry with silicone vascular models*, Experiments in fluids **50**, 769 (2011).
- [39] H. Samavat and J. Evans, *An ideal blood mimicking fluid for doppler ultrasound phantoms*, Journal of medical physics/Association of Medical Physicists of India **31**, 275 (2006).
- [40] N.-S. Cheng, *Formula for the viscosity of a glycerol-water mixture*, Industrial & engineering chemistry research **47**, 3285 (2008).
- [41] R. Houwink and H. K. De Decker, *Elasticity, plasticity and structure of matter* (Cambridge University Press, 1971).
- [42] A. Junaid, *Tissue phantom for robotic needle insertion in the liver*, Report (Zuyd University of Applied Sciences, University of Technology Delft, 2012).
- [43] S. Barrett, M. Sutcliffe, S. Howarth, Z. Li, and J. Gillard, *Experimental measurement of the mechanical properties of carotid atherothrombotic plaque fibrous cap*, Journal of biomechanics **42**, 1650 (2009).
- [44] R. Kassing, F. Jacobs, A. v. Hilten, and F. Paalman, *Invloed van de penetratiesnelheid op de penetratiekracht in een Chronische Totale Occlusie: een haalbaarheidsstudie*, Report (Delft University of Technology, 2015).
- [45] A. Thind, B. Strauss, A. Teitelbaum, R. Karshafian, M. Ladouceur, C. Whyne, D. Goertz, and S. Foster, *A novel method for the measurement of proximal fibrous cap puncture force in chronic total occlusions: the effect of increasing age*, EuroIntervention: journal of EuroPCR in collaboration with the Working Group on Interventional Cardiology of the European Society of Cardiology 6, 997 (2011).
- [46] M. Mahvash and P. E. Dupont, *Mechanics of dynamic needle insertion into a biological material*, Biomedical Engineering, IEEE Transactions on **57**, 934 (2010).
- [47] C. Nguyen and T. Vu-Khanh, *Mechanics and mechanisms of puncture by medical needles*, Procedia Engineering 1, 139 (2009).
- [48] V. Raghavan, *Analysis of performance of jack hammer to determine the penetration rate on different rocks*, The International Journal of Engineering and Science **3**, 8 (2014).

A. ARTERY MODELLING

This appendix provides a detailed view on the main endovascular intervention approaches. The focus in these approaches is on the travel path through the human vascular system. This information, together with geometrical details of the vascular system and calculations, was used to gain insight in the medical procedure and to define design requirements 2.1 and 2.2.

A.1. ENDOVASCULAR ROUTES

The most prevalent location of a CTO within the coronary arteries is the Right Coronary Artery (RCA) [17]. For the peripheral arteries, the Superficial Femoral Artery (SFA) is the most common location [49,50]. Even though this project focusses on the coronary arteries, the peripheral occlusion analysis was added to give a more global insight in endovascular interventions. To approach the RCA and SFA, several endovascular routes can be taken. Two common approaches for each of the occlusion locations were selected for this analysis:

- 1. RCA Transfemoral approach
- 2. RCA Radial approach
- 3. SFA Ipsilateral antegrade approach
- 4. SFA Contralateral retrogade approach

In the case of a transfemoral approach, the artery system is entered at the groin into the Common Femoral Artery (CFA). From here, the path travels upwards towards the heart. The vascular route is specified in detail in Table A.1 and shown in Figure A.1. For the radial approach, the artery system is entered at the wrist into the Radial Artery (RA). In this approach, the pathway travels upwards through the arm and shoulder to the heart. For both the described approaches for reaching an occlusion in the SFA, the vascular system is entered at the groin, either on the ipsilateral or the contralateral side of the body. The detailed description of the latter three approaches are also given in Table A.1 and Figure A.1.

Table A.1: The detailed arterial routes of the four selected endovascular paths: (1) RCA - Transfemoral approach, (2) RCA - Radial approach, (3) SFA - Ipsilateral antegrade approach, and (4) SFA - Contralateral retrogade approach.

1. Transfemoral	2. Radial	3. Ipsilateral	4. Contralateral
Common femoral artery	Radial artery	Common femoral artery	Common femoral artery
External illiac artery	Brachial artery	Superficial femoral artery	External illiac artery
Common illiac artery	Axillary artery		Common illiac artery
Descending aorta	Subclavian artery		Common illiac artery
Aortic arch	Brachiocephalic artery		External illiac artery
Ascending aorta	Aortic arch		Common femoral artery
Right coronary artery	Ascending aorta		Superficial femoral artery
	Right coronary artery		_

A.2. ARTERY DIAMETERS, BIFURCATONS AND CURVATURE

The geometry of the four described endovascular routes have been identified in more detail. These details include the average artery diameters, curvature of the arteries, and artery bifurcation angles. The artery diameters of all arteries that are passed in one of the four routes have been obtained from literature. These diameters are presented in Table A.2. It can be seen that the diameters found in literature differ slightly between sources. Therefore, an average number was calculated for further modelling and calculation. This average diameter was defined as the mean of the smallest and largest number given in the table; given in the final column of Table A.2. The artery curvatures and bifurcation angles have been defined by estimation, and are given in Table A.3 and Table A.4 respectively.

The presented artery diameters, curvatures, and bifurcations that are present in the analysed endovascular routes have been used to model the routes in simplified nodes. These nodes represent the curvatures and bifurcations that need to be passed during the intervention from the location of instrument insertion to the lesion. The annotation of the nodes, as well as the simplified models of the nodes, are given in Figure A.2.

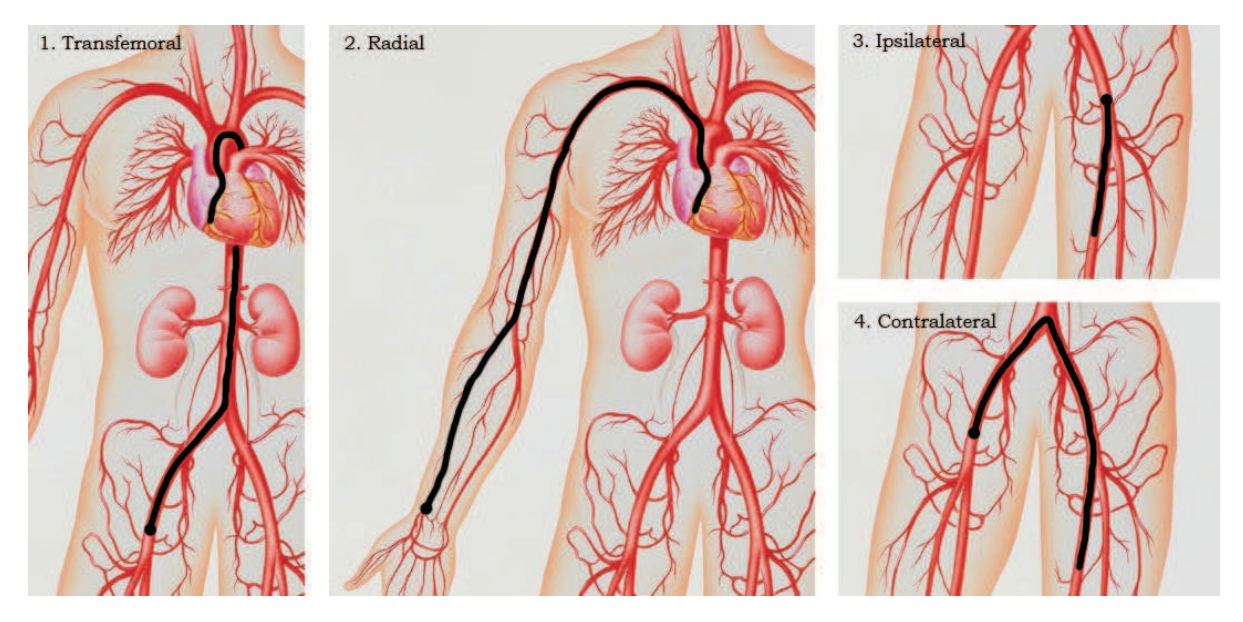


Figure A.1: The arterial routes of the four selected endovascular paths in the body: (1) RCA - Transfemoral approach, (2) RCA - Radial approach, (3) SFA - Ipsilateral antegrade approach, and (4) SFA - Contralateral retrogade approach. Figures adjusted from [26].

Figure A.2(a) and A.2(b) show the nodes for the transferoral approach to the RCA, Figure A.2(c) and A.2(d) for the radial approach to the RCA, and finally Figure A.2(e) and A.2(f) the contralateral retrogade approach to the SFA. The ipsilateral antegrade approach to the SFA may be described as part of the contralateral retrogade approach.

A.3. ENDOVASCULAR INSTRUMENT FLEXIBILITY

The minimal flexibility of an instrument to be used for endovascular intervention restricts the maximum length of stiff instrument parts. By means of analysis of all artery bifurcations and curvatures, together with the artery diameters, a guideline for this maximum stiff part length was derived.

The nodes shown in Figure A.2 have been used as input for the calculations. To derive the maximum stiff part length to pass through a bifurcation, the bifurcation has been translated into a curvature first with the help of Equations A.1-A.3. The Equations A.4-A.6 are subsequently used to derive the desired length. For the first set of Equations (A.1-A.3) the derivation and inputs (bifurcation angle α , diameter of the smallest artery D_{small} , and diameter of the largest artery D_{large}) are presented in Figures A.3(a) and A.3(b). Similarly, the derivation and inputs (artery curvature R_{curve} , artery radius $R_{art} = \frac{1}{2} \cdot D_{art}$, and instrument diameter \emptyset_{instr}) of Equations A.4-A.6 are shown in Figure A.3(c). For the calculations an instrument diameter of 2 mm was used.

$$Y = D_{large} - \frac{1}{2} \cdot D_{small}$$

$$X = \frac{\cos \alpha \cdot Y}{1 - \cos \alpha}$$

$$R_{curve} = X + Y$$
(A.1)
(A.2)

$$X = \frac{\cos \alpha \cdot Y}{1 - \cos \alpha} \tag{A.2}$$

$$R_{curve} = X + Y \tag{A.3}$$

$$P = R_{curve} - R_{art} + \emptyset_{instr} \tag{A.4}$$

$$Q = R_{curve} + R_{art} \tag{A.5}$$

$$Q = R_{curve} + R_{art}$$

$$L = \sqrt{Q^2 - P^2}$$
(A.5)
$$(A.6)$$

In table A.5 the results of all calculations are presented. From the table it has been derived that the bifurcation from the ascending aorta to the RCA is the most restrictive node for reaching a lesion in the RCA. For the flexibility of the instrument design (requirement 2.2) the maximum stiff part length was set to 6.5 mm; the smallest number from all calculations.

Comparing the diameter and stiff part length with two state-of-the-art systems, the *Frontrunner XP* (Cordis Corporation, Miami, FL, USA) and *Wildcat catheter* (Avinger, Redwood City, CA, USA), the dimensions were confirmed to be suitable for a first design. The *Frontrunner XP*, presented in Figure A.4, is 1 mm in diameter and has a tip length estimated at 4.4 mm. The Wildcat catheter, shown in Figure A.5, has a diameter of 2 mm and a tip length estimated at 5.5 mm.

Table A.2: Artery diameters given in millimeters, as cited in literature. The letters given in between brackets are used as follows: f = female, m = male, d = distal, p = proximal, a = abdominal, and t = thoracic.

	Avolio [27]	Terumo [28]	Other	
Common illiac artery	10.4	7 - 10		8.7
External illiac artery	5.4 - 5.8	6 - 8		6.7
Common femoral artery		8 - 11	7.5 (f) 10.4 (m) [29]	9.3
Superficial femoral artery	4.8			4.8
Aortic arch	21.4 - 22.4			21.9
Ascending aorta	29.0			29.0
Brachiocephalic artery	12.4			12.4
Subclavian artery	8.0			8.0
Axillary artery	6.2 - 7.2			6.7
Brachial artery	4.8 - 5.6			5.2
Radial artery	3.2		2.3 [30]	2.8
			2.8 (f) 3.1 (m) [31, 32]	
			2.4 (f) 2.7 (m) [33]	
Descending aorta	19.0 - 20.0 (t)	15 - 20		15.7
	11.4 - 17.4 (a)			
Right coronary artery			1.9 (d) 4.0 (p) [34]	3.0

Table A.3: Estimated curvature radii given in millimeters.

	Radius
Common femoral / External illiac artery	100
Brachial / Axillary / Subclavian artery	60
Aortic arch	20
Right coronary artery	29

 ${\it Table A.4: Estimated bifurcation angles given in degrees.}$

	Angle
Radial - Brachial artery	150
Brachiocephalic artery - Aortic arch	90
Aortic arch - Right coronary artery	90
Common illiac - Common illiac artery	90

Table A.5: Calculation results for the maximum stiff part length for the instrument design, for all of the modelled nodes (of figure A.2), given in millimeters.

RCA - Transfemoral		RCA -	- Radial	SFA - Contralateral		
Node	Length	Node	Length	Node	Length	
1	30.8	1	6.9	1	30.8	
2	23.1	2	23.9	2	8.5	
3	28.9	3	18.6	3	30.8	
4	6.5	4	28.9			
5	7.7	5	6.5			
		6	7.7			

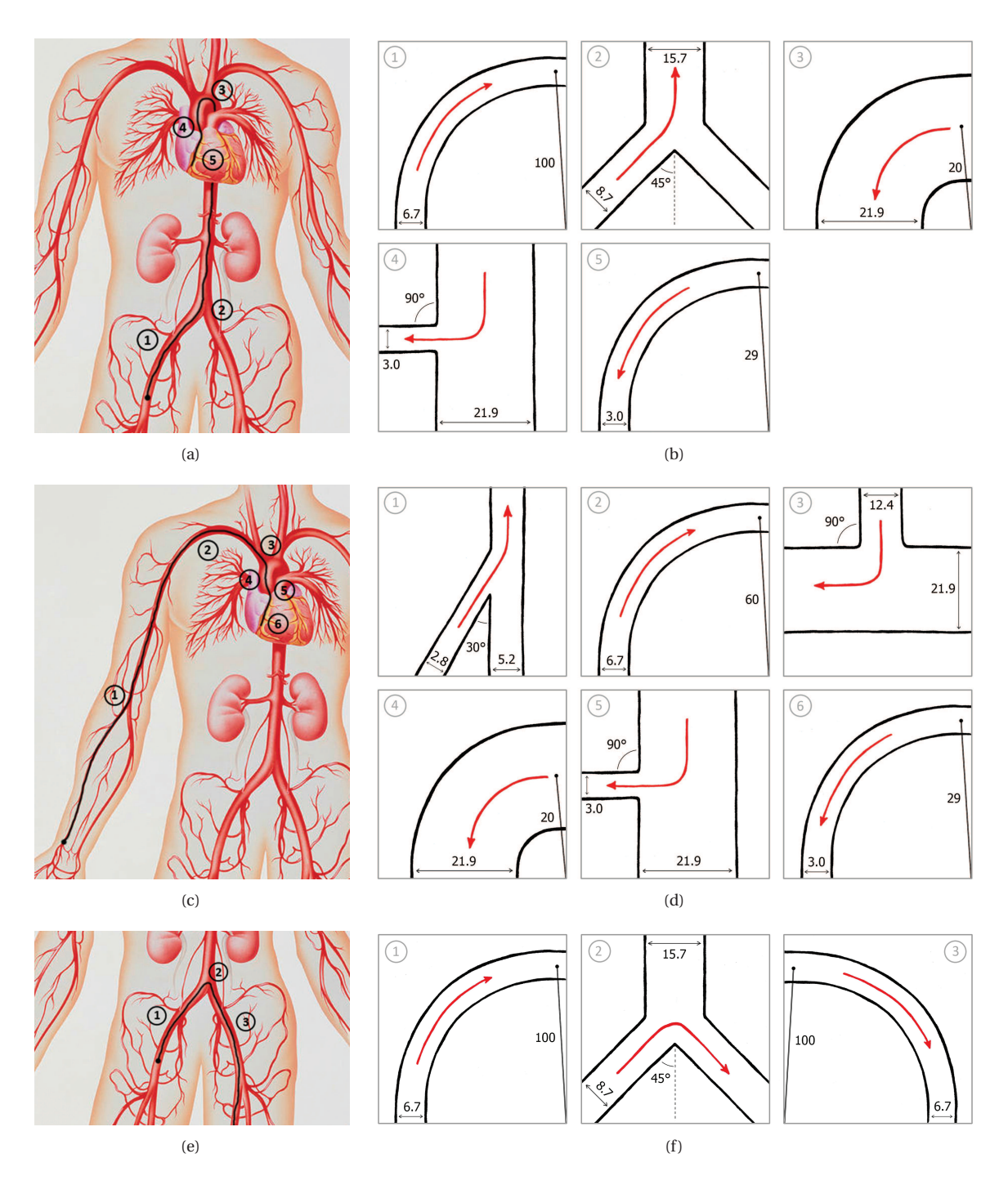


Figure A.2: Identification and modelling of the nodes on the four selected endovascular routes. (a) Node identification of the RCA - Transfemoral approach. (b) Node modelling of the RCA - Transfemoral approach. (c) Node identification of the RCA - Radial approach. (d) Node modelling of the RCA - Radial approach. (e) Node identification of the SFA - Contralateral retrogade approach. (f) Node modelling of the SFA - Contralateral retrogade approach. Figures (a), (c), and (d) adjusted from [26].

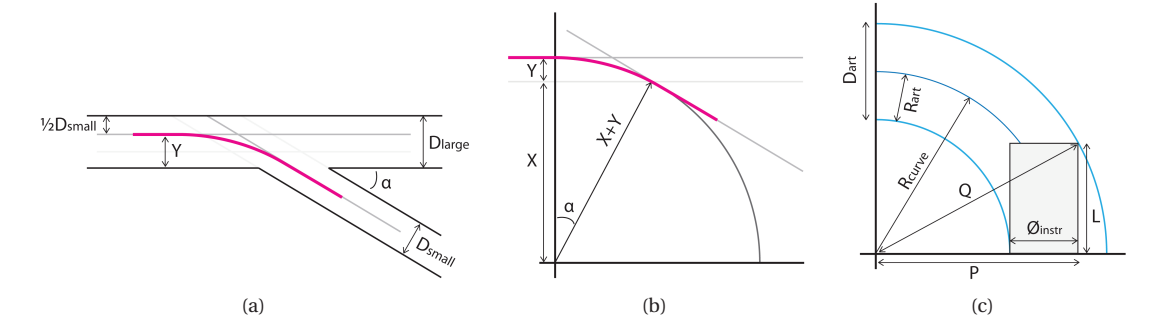


Figure A.3: Simplified drawings showing the formula derivation for calculating the maximum stiff part length of an endovascular instrument to travel through set curvatures and bifurcations. (a) Inputs of formulas A.1-A.3. (b) Derivation of formulas A.1-A.3. (c) Inputs and derivation of formulas A.4-A.6.

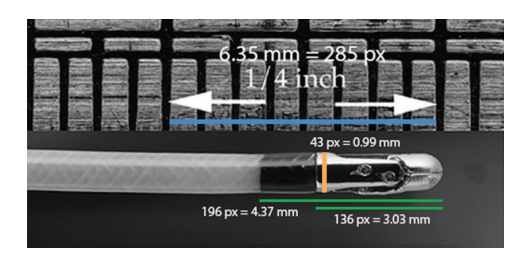


Figure A.4: *Frontrunner XP* (Cordis Corporation, Miami, FL, USA), with estimated diameter 1 mm and tip length of 4.4 mm. Figure adjusted from [51].

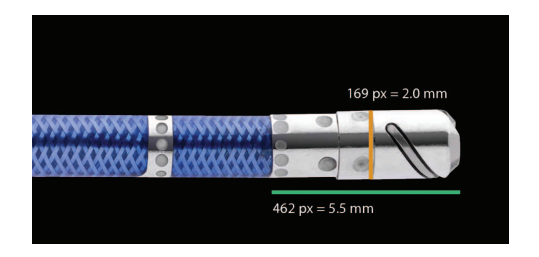


Figure A.5: *Wildcat catheter* (Avinger, Redwood City, CA, USA), with estimated diameter 2 mm and tip length of 5.5 mm. Figure adjusted from [52].

REFERENCES

- [17] G. W. Stone, A. Colombo, P. S. Teirstein, J. W. Moses, M. B. Leon, N. J. Reifart, G. S. Mintz, A. Hoye, D. A. Cox, and D. S. Baim, *Percutaneous recanalization of chronically occluded coronary arteries: Procedural techniques, devices, and results*, Catheterization and cardiovascular interventions **66**, 217 (2005).
- [27] A. Avolio, *Multi-branched model of the human arterial system*, Medical and Biological Engineering and Computing **18**, 709 (1980).
- [28] Terumo Medical Corporation, *Azur peripheral hydrocoil embolization system*, (2008), retrieved November 20, 2014 from http://www.terumois.com/administration/Collateral.aspx.
- [29] T. Sandgren, B. Sonesson, s. R. Ahlgren, and T. Länne, *The diameter of the common femoral artery in healthy human: influence of sex, age, and body size*, Journal of vascular surgery **29**, 503 (1999)
- [30] P. Boutouyrie, C. Bussy, P. Lacolley, X. Girerd, B. Laloux, and S. Laurent, *Association between local pulse pressure, mean blood pressure, and large-artery remodeling,* Circulation **100**, 1387 (1999).
- [31] S. Saito, H. Ikei, G. Hosokawa, and S. Tanaka, *Influence of the ratio between radial artery inner diameter and sheath outer diameter on radial artery flow after transradial coronary intervention*, Catheterization and Cardiovascular Interventions **46**, 173 (1999).
- [32] M. A. Kotowycz and V. Džavík, *Radial artery patency after transradial catheterization*, Circulation: Cardiovascular Interventions **5**, 127 (2012).
- [33] B.-S. Yoo, J. Yoon, J.-Y. Ko, J.-Y. Kim, S.-H. Lee, S.-O. Hwang, and K.-H. Choe, *Anatomical consideration of the radial artery for transradial coronary procedures: arterial diameter, branching anomaly and vessel tortuosity,* International journal of cardiology **101**, 421 (2005).
- [34] J. Dodge, B. G. Brown, E. L. Bolson, and H. T.Dodge, *Lumen diameter of normal human coronary arteries. influence of age, sex, anatomic variation, and left ventricular hypertrophy or dilation*, Circulation **86**, 232 (1992).
- [49] L. L.Nadal, J. Cynamon, E. C. Lipsitz, and A. Bolia, *Subintimal angioplasty for chronic arterial occlusions*, Techniques in vascular and interventional radiology 7, 16 (2004).
- [50] EndoCross, What is coronary arterial disease (cad)?, Retrieved November 20, 2014 from http://endocross.eu/clinical-background/.
- [51] G. D. Dangas, R.Mehran, and J.Moses, Handbook of Chronic Total Occlusions (CRC Press, 2007).
- [52] Avinger, Wildcat, Retrieved October 1, 2014 from http://intl.avinger.com/products/wildcat_ous.

B. ACTUATION FEASIBILITY REVIEW

This appendix includes the complete argumentation for the initial feasibility review of all 25 actuation ideas to accelerate an indenter within the instrument, that will eventually exert an impact force onto the CTO. This feasibility check was based on five basic requirements:

- 1. Medical safety
- 2. Dimensional feasibility
- 3. Level of reachable velocity
- 4. Reload ability
- 5. Shape independency

For the *medical safety* requirement, the concept was judged on possible medical risks and interference with medical procedures for the endovascular intervention. For example, the incidence of an air bubble within the artery system is of high risk, therefore the use of pneumatics has been excluded as feasible actuation method. The *dimensional feasibility* check included the judgment on the possibility to develop the actuation method within the limited dimensions of the instrument (maximum instrument diameter and stiff tip length of 2 mm and 6.5 mm, respectively). For the *velocity feasibility* check, the concepts have been compared on their potential to generate a "high" velocity. In this case, for example, a high influence of friction within the actuation is undesired, and the bi-metal and bi-stable element, with only small impact distances, have been judged with less potential to generate large moment, compared to a helical spring. For the ability to create a *reloadable action*, the actuation elements have been judged on the ability to reload the action or to develop a reload mechanism. Finally, the actuation elements have been judged on the *shape dependency* of the action. The elements using a shockwave or hydraulic transmission, will be largely influenced by the shape of the (long and flexible) instrument, whereas actuation elements that are located in the tip of the instrument may function largely independent of shape.

The feasibility selection was done with the help of a criteria table, using a judgement scale with three values: positive (+), neutral (0), and negative (-). The (+) accounts for all positive expectations on each of the requirements; for which the development and use of the actuation element will most certainly not lead to any problems. The (0) is used for a neutral or uncertain expectation. In development this may include extra design challenges, which are, however, anticipated not to be insurmountable. Moreover, it may represent an uncertainty in knowledge. Finally, a (-) is linked to ideas with negative expectations. This includes, for example, insurmountable design problems or significantly lower performance in comparison with other solutions.

In Table B.1 the criteria review is presented for all actuation elements. The arguments for all of the classifications made are noted in the table with a small, blue, number, which refers to one of the arguments presented below the table.

Based on the criteria table, five concepts have been selected as most feasible actuation ideas: (1) *stream push*, (2) *electromagnetic force*, (3) *SMA wire spring*, (4) *helical spring*, and (5) *elastic stretch band*. These five concepts have been taken into account during a next selection phase, which included a more in-depth evaluation on all criteria.

Table B.1: Criteria judgement table for the selection of feasible actuation ideas. The ideas (1 - 25) are presented on the left and the criteria (1 - 5) are presented at the top. The small blue numbers link to the arguments below this table.

		Medio	cal	Dim	ension	Velocity		Reloadable		Sh	ape
1	Free flight transmission	+	1	+	5	0	9	0	15	-	19
2	Hydraulic shockwave	0	2	+	5	0	9	+	16	-	19
3	Dense ball shockwave	+	1	+	5	0	9	+	16	-	19
4	Cable pull transmission	+	1	0	6	-	10	0	15	-	19
5	Stiff push transmission	+	1	+	5	-	10	+	16	-	19
6	Mechanical linkage	+	1	-	7	-	10	+	16	-	19
7	Stream push	0 2	,3	+	5	0	9	+	16	0	20
8	Inside-out inflation	0 2	,3	-	7	0	9	0	15	0	20
9	Squeeze inflation	0 2	,3	-	7	0	9	-	17	0	20
10	External magnetic guide	0	2	+	5	0	9	+	16	-	19
11	Rotation screw system	+	1	+	5	-	11	+	16	0	20
12	Treadmill system	+	1	-	7	-	12	+	16	0	20
13	Electromagnetic force	0	2	0	6	0	13	+	16	+	21
14	SMA wire spring	0	2	0	6	0	13	+	16	+	21
15	Bi-metal element push	0	2	0	6	-	11	+	16	+	21
16	Tube shape squeeze	0	2	-	7	0	9	-	17	+	21
17	Miniature treadmill	0	2	ı	7	0	13	+	16	+	21
18	Helical spring	+	1	+	5	+	14	0	15	+	21
19	Elastic stretch band	+	1	+	5	+	14	0	15	+	21
20	Chameleon squeeze	+	1	-	8	-	12	-	17	+	21
21	Bi-stable element push	+	1	0	6	-	11	0	15	+	21
22	Torsion spring wheels	+	1	-	7	0	13	0	15	+	21
23	Jet push		4	-	7	0	13	0	18	+	21
24	Explosion push		4	+	5	+	14	0	18	+	21
25	Propeller propulsion	0	2	-	7	-	11	+	16	+	21

- 1 A pure mechanical solution is medically the most safe solution.
- 2 Uncertainties about possible medical risks (e.g. heating, leaking of fluid, magnetic interference, electronics), but expected to be solvable (e.g. isolation, biocompatible fluid selection).
- 3 Pneumatics is unsafe due to risks of air embolism (only the hydraulic version is taken into account).
- 4 Pneumatics is unsafe due to risks of air embolism and chemical reactions are medically risky. Biocompatible chemical reactions that are safe in use, are expected to be difficult to find and implement.
- 5 Expected to be realizable in small dimensions.
- 6 Uncertainties about minimal dimensions for realization.
- 7 Expected to give large difficulties for realization in small dimensions.
- 8 Idea based on example from nature (chameleon tongue); unknown to exist in mechanical version, therefore large difficulties are expected for the realization of this idea.
- 9 Uncertainties around velocity (momentum) generation, due to unknown friction forces and effects of transmission through bended parts.
- 10 Undesired delay in transmission expected, including deceleration due to friction and elastic behavior.
- 11 Only low velocity (momentum) generation is expected due to the method of acceleration.
- 12 Only low velocity (momentum) generation is expected due to friction.
- 13 Uncertain velocity (momentum) generation.
- 14 Expected to give highest velocity (momentum) output.
- 15 Design of reloading system is necessary, but expected to be solvable.
- 16 Direct reversible or repeatable action.
- 17 Large difficulties or complexity is expected for the design of a reloading system.
- 18 Reloading a chemical package brings design complexity; expected to be solvable.
- $19\,$ Transmission efficiency is highly dependent on the shape of the catheter.
- 20 Activation through bended catheter length might give undesired friction effects and/or delay.
- 21 Activation located within the tip of the catheter prevents shape dependency problems.

C. ACTUATION CRITICAL REVIEW

Within this appendix an extensive analysis of five possible actuation elements for the design of the instrument will be described. The five actuation elements that have been selected are the following: (1) *Hydraulic stream push,* (2) *electromagnetic coil,* (3) *shape memory alloy (SMA) wire spring,* (4) *helical spring,* and (5) *elastic stretch band.* These five actuation elements have been judged to be the most feasible ideas from the complete list of 25 generated ideas.

The following appendix sections are each dedicated to one of the five ideas. All of the ideas will be described in functioning and critically judged on the criteria that were used for the feasibility check (see appendix B; medical safety, dimensional feasibility, level of reachable velocity, reload ability, and shape independency). Finally, a conclusion is drawn on the most promising actuation method.

C.1. HYDRAULIC STREAM PUSH

A hydraulic actuator makes use of hydraulic pressure to drive a system. This hydraulic stream push idea uses hydraulic pressure to drive the acceleration of an indenter. This pressure is generated at the distal end of the catheter and will pass through the complete instrument to be used as actuator in the tip of the instrument.

Medical safety

The anticipated medical risks of this concept include liquid leakage and hose or cylinder failure. Both these risks have been judged to be surmountable with the selection of safe liquid and suitable parts. For the liquid, saline is an example that can be used, which is a sterile solution of sodium chloride in water. This solution is used in intravenous infusion and other medical, mostly cleaning, activities.

Dimensional feasibility

The selection and development of parts for this hydraulic system, that fit the limited dimensions, is judged to be challenging. Most hydraulic actuators are used to drive large and heavy systems, rather than miniature and precision mechanisms. However, the development of a miniature hydraulic system for the instrument is not expected to be unfeasible, since other miniature hydraulic solutions have been developed in the past [53].

Velocity feasibility

The feasibility of reaching a desired velocity has been foreseen to be one of the critical factors of this concept. To be able to compare this concept with the other ideas, an estimation of the maximum hydraulic stream velocity within a thin tube was made. This was done through a calculation with the Reynold's number (Re), which is used to predict at which velocity a flow becomes turbulent. Turbulent flow is related to undesired high friction and inconsistency of pressure and velocity of the flow. The formula to estimate the maximum flow velocity before turbulence (Re > 3500) arises in a cylindrical straight tube is given in Equation C.1. In a tube with an inner diameter of 1.6 mm the estimated maximum velocities of 37°C water ($\rho = 1000 kg/m^3$ and $\eta \approx 0.69 mPa \cdot s$) and blood ($\rho = 1000 kg/m^3$ and $\eta \approx 3.50 mPa \cdot s$) are 1.5 m/s and 7.7 m/s respectively. As shown, the fluid viscosity is of quite large influence. For higher viscous fluids the maximum velocity increases, but so does the flow resistance, so also higher input forces are needed to reach a similar flow velocity.

$$Re = \frac{\rho \cdot v \cdot d}{\eta} \tag{C.1}$$

 $Re = \text{Reynold's number } [-], \ \rho = \text{density of the fluid } [kg/m^3], \ v = \text{velocity of the fluid } [m/s], \ d = \text{inner diameter of the tube } [m], \ \eta = \text{dynamic viscosity } [Pa \cdot s]$

Reload ability

The hydraulic solution is highly favorable for its two-way control possibility. Both a push and pull force may be realized through a closed liquid-filled chamber, which is for example used in a syringe (pulling to fill the syringe with liquid and pushing to inject the liquid into the desired location). Based on this characteristic, it is foreseen that reloading of the actuator should not bring design difficulties.

Shape dependency

The shape dependent actuation that is anticipated with this concept is the second most critical factor. It is not only the fluid viscosity that is of influence on the flow resistance, but also the shape. To gain a consistent output at the instrument tip, the input force should be adapted to the shape and length of the instrument. For this reason, the concept is unfavourable.

C.2. ELECTROMAGNETIC COIL

This second concept describes an electromagnetic coil that can be used to transfer electrical energy to forces. A current that is flowing through a conductor creates a circular magnetic field around this conductor, as described by Ampere's law. The magnetic field may be used as actuator force by the repelling interaction between this electromagnet and a permanent magnet, that may be accelerated as a result of the interaction.

Medical safety

When considering the medical application of this idea, the use of electricity may be judged as risky, and moreover, the magnetic elements could interfere with other magnetic medical systems (for example MRI). When designing the instrument with this actuation method, these two concerns should be taken into account; for the wiring, a good isolation design should be made, and for the magnetic interference, the intervention procedure should be analyzed and tuned to make sure the magnetic applications will only run consecutively.

Dimensional feasibility

For de development of an electromagnetic driven instrument, both off-the-shelve available copper wire and coils may be used. Copper wire is widely available with small diameters, with a minimum of 0.2 mm found. It has been concluded that the dimensional feasibility of this concept is trivial.

Velocity feasibility

An estimation of the maximum velocities that may be reached with a miniature electromagnetic coil was made in two steps. First of all, calculations were performed to define possible coil designs with the help of Equations C.2-C.7.

$$t_{coil} = \frac{\emptyset_{out} - \emptyset_{in}}{2} \tag{C.2}$$

$$C_{mean} = 2 \cdot \pi \cdot \frac{\emptyset_{out} + \emptyset_{in}}{2} \tag{C.3}$$

$$t_{coil} = \frac{\emptyset_{out} - \emptyset_{in}}{2}$$

$$C_{mean} = 2 \cdot \pi \cdot \frac{\emptyset_{out} + \emptyset_{in}}{2}$$

$$A = \pi \cdot \left(\frac{\emptyset_{out}}{2}\right)^{2}$$

$$N = \frac{L_{coil}}{\emptyset_{wire}} \cdot \frac{t_{coil}}{\emptyset_{wire}}$$

$$L_{wire} = N \cdot C_{mean}$$

$$R_{tot} = L_{wire} \cdot T_{wire}$$
(C.2)
$$(C.3)$$

$$(C.4)$$

$$(C.5)$$

$$(C.5)$$

$$N = \frac{L_{coil}}{Q_{ming}} \cdot \frac{t_{coil}}{Q_{ming}} \tag{C.5}$$

$$L_{wire} = N \cdot C_{mean} \tag{C.6}$$

$$R_{tot} = L_{wire} \cdot r_{wire} \tag{C.7}$$

 $\emptyset_{out} = \text{coil outer diameter } [mm], \emptyset_{in} = \text{coil inner diameter } [mm], \emptyset_{wire} = \text{wire diameter } [mm], L_{coil} = \text{coil length } [mm], r_{wire} = \text{wire diameter } [mm], L_{coil} = \text{coil length } [mm], r_{wire} = \text{wire diameter } [mm], L_{coil} = \text{coil length } [mm], r_{wire} = \text{wire diameter } [mm], L_{coil} = \text{coil length } [mm], r_{wire} = \text{wire diameter } [mm], L_{coil} = \text{coil length } [mm], L_{coil}$ resistivity $[\Omega/m]$, t_{coil} = coil thickness [mm], C_{mean} = average coil circumference [mm], A = cross-sectional area of coil $[mm^2]$, N = number of windings [-], L_{wire} = total wire length [mm], R_{tot} = total wire resistance [Ω]

In total, four coils have been evaluated, each with a different wire diameter. The coil designs were modelled with an outer diameter, inner diameter, and length of 1.6 mm, 0.8 mm, 5 mm, respectively. The copper wire diameter ranged from 0.02 mm to 0.1 mm. With these inputs, the number of coils and total wire resistance could be estimated, and were subsequently used as input for the performance evaluation. The results are presented in Table C.1.

The Equation C.8 has subsequently been used to estimate the performance of the electromagnetic coils. For the calculations a current range between 100 - 500 mA was selected. The cross-sectional area was defined to be 2.0 mm (see Equation C.4), the initial gap distance between coil and ferro-magnet was set to 0.5 mm, and the magnetic constant in the formula is equal to $4\pi \cdot 10^{-17}$. The final velocities anticipated with the estimated forces have been calculated with the help of MATLAB 2013b (The MathWorks, Inc., Natick, MA, USA) and Equations C.9-C.11. The velocities presented were taken at a distance of 5.5 mm from the coil (after a travelled distance of 5 mm), with a mass of 0.1 and 1.0 gram, and timesteps of 1.0 μ s. The results of the calculations are given in Table C.2.

$$F = \frac{N^2 \cdot I^2 \cdot A \cdot \mu}{2 \cdot g^2}$$

$$a = \frac{F}{m}$$

$$v = v + a \cdot t_s$$
(C.8)
(C.9)

$$a = \frac{F}{m} \tag{C.9}$$

$$v = v + a \cdot t_s \tag{C.10}$$

$$s = s + v \cdot t_s \tag{C.11}$$

F = force between coil and ferro-magnet [N], N = number of windings [-], I = current through wire [A], μ = magnetic constant [-], g = gap distance between coil and ferro-magnet [mm], a = acceleration $[m/s^2]$, v = velocity [m/s], s = travelled distance [m], $t_s =$ time step [s]

From the presented performance evaluation, it was concluded that the most optimal performing coil is developed from wire with diameter of 0.04 mm (coil 2, taking into account 200mA and 15V as current and voltage limit, respectively). This coil produces a maximum force of 0.3 N with the gap distance set to 0.5 mm. The anticipated maximum velocities for a 1.0 gr and 0.1 gr load to be accelerated (neglecting any influences of friction) are 0.5 m/s and 1.7 m/s respectively. When reducing the initial gap distance to 0.2 mm these velocities may approximately be doubled to 0.9 m/s and 2.8 m/s.

Table C.1: Calculated characteristics of four different coil designs, with varying thicknesses of copper wire. The wire resistivity of the different wires were taken from [54].

		Coil 1	Coil 2	Coil 3	Coil 4
Wire diameter (Ø _{wire})	[mm]	0.02	0.04	0.06	0.10
Wire resistivity (r_{wire})	$[\Omega/m]$	55.8	13.8	5.5	2.1
Number of windings (N)	[-]	5000	1250	488	192
Total wire length (L_{wire})	[<i>m</i>]	19	4.8	1.9	0.7
Total wire resistance (R_{tot})	[Ω]	1060	65.6	10.4	1.5

Table C.2: Results of the performance evaluation of the four modelled electromagnetic coils (see table C.1) with varying wire thicknesses.

		Coil 1	Coil 2	Coil 3	Coil 4		
I = 100 mA							
Voltage $(I \cdot R_{tot})$	[V]	106	6.5	1.0	0.2		
Max force	[N]	1.26	0.08	0.01	0.002		
Velocity, m = 0.1 gr	[m/s]	3.38	0.84	0.33	0.13		
Velocity, m = 1.0 gr	[m/s]	1.07	0.27	0.10	0.04		
I = 200 mA							
Voltage $(I \cdot R_{tot})$	[V]	212	13	2.1	0.3		
Max force	[N]	5.03	0.31	0.05	0.01		
Velocity, m = 0.1 gr	[m/s]	6.76	1.69	0.66	0.26		
Velocity, m = 1.0 gr	[m/s]	2.14	0.53	0.21	0.08		
I = 500 mA							
Voltage $(I \cdot R_{tot})$	[V]	530	32.8	5.2	0.8		
Max force	[N]	31.4	1.96	0.30	0.05		
Velocity, m = 0.1 gr	[<i>m</i> / <i>s</i>]	16.9	4.22	1.65	0.65		
Velocity, m = 1.0 gr	[m/s]	5.34	1.34	0.52	0.21		

Reload ability

Similar to the reload ability of the previous presented hydraulic concept, the electromagnetic actuator has a two-way control possibility. By switching the direction of the current through the wire of the coil, the magnetic field changes. Depending on this magnetic field, it either repels or attract a magnet. The design of a reloadable action, by means of switching current direction, should not give design difficulties.

Shape dependency

For this concept the shape dependency is assumed to be absent, as the actuator may be located in the tip of the instrument. The bending of the instrument and the long travel distances for the control of the actuation, which may only be two electrical wires placed within the catheter, will not have any influence on the final functioning of the actuator in the tip.

C.3. SMA WIRE SPRING

Shape-Memory Alloys (SMA) are materials that can be used as actuator with shape-changing characteristics based on temperature change. This material "memorizes" a certain shape that can be imprinted by exposing it to high heat. In a cold condition, the material may be deformed, but it will return to its memorized shape when heated above its activation temperature. SMA wire may be used to develop a coil spring that will collapse and exert a force when heated above its activation temperature. Heating of the wire can be realized by running current through the wire, with the principle of Joule heating. Nitinol (nickel-titanium) is the most commonly used SMA.

Medical safety

The main medical risk that is associated with the use of SMA wire is the high activation temperature. The temperature to activate nitinol wire is given to be between 55°C - 75°C, which is undesirable to be transferred to body tissue. In case this concept is to be implemented in an instrument, isolation between body and actuator should be carefully designed.

Dimensional feasibility

Nitinol wire is available in small dimensions, with a minimum found diameter of 0.02 mm. This gives a first indication for the feasibility of developing SMA coil springs in miniature dimensions. In the study by Follador et al. [55] springs with outer diameter of 1.2 and 1.7 mm and wire diameter of 0.2 mm have been created. For this reason the dimensional feasibility was judged positively.

Velocity feasibility

The SMA wire spring actuator may accelerate the indenter at the moment of transition from cold to heated (activated) condition. To estimate the performance of this actuator, information about the power of the transition (transition force and velocity) is needed. Whereas equations are available to derive the spring rate and maximum force to be exerted by the spring in either the cold or the heated condition [55], they do not describe the power of the transition between the two phases. Therefore, it has been concluded the actual acceleration performance of this concept can only be found through experimentation.

Reload ability

For the development of a reloadable action, there are possibilities to create two-way shape memory effects within SMA applications, however, these are either difficult to manufacture or have a lack of reliability [56]. A one-way SMA wire can only provide a tensile force, so for returning the system into the initial condition either a bias force or an antagonistic second spring is needed [57], increasing the complexity of the concept.

Shape dependency

The SMA wire spring may be located in the tip of the instrument, and controlled through the placement of electrical wires throughout the instrument. This configuration is similar to the described configuration for the electromagnetic coil concept. It has been argued that the shape of the instrument will not have influence on the performance of the actuator.

C.4. HELICAL SPRING

A helical spring can be used to actuate the indenter. When compressing (or pulling) the spring, elastic energy will be stored, which may be released to push forward an indenter.

Medical safety

Due to the purely mechanical working principle of this actuator, no medical risks have been anticipated for this concept.

Dimensional feasibility

The dimensional feasibility of the simple coil spring was judged positively. Miniature compression springs, that fulfill the requirement of fitting within a tube with an inner diameter of 1.6 mm, are widely off-the-shelve available, and may be easily implemented within instrument.

Velocity feasibility

An estimation of the performance of a small helical compression spring was made in a similar way as for the electromagnetic coil concept. The force delivered by the spring may be defined with the spring rate and the distance of spring compression or tension (Equation C.12). By means of calculating the effect of the spring force on acceleration and velocity over time, resulting velocities have been estimated. This was done with Equations C.13-C.15 implemented in MATLAB 2013b (The MathWorks, Inc., Natick, MA, US).

$$F = k \cdot x \tag{C.12}$$

$$F = k \cdot x$$
 (C.12)

$$a = \frac{F}{m}$$
 (C.13)

$$v = v + a \cdot t_s$$
 (C.14)

$$v = v + a \cdot t_s \tag{C.14}$$

$$s = s + v \cdot t_s \tag{C.15}$$

 $F = \text{spring force } [N], k = \text{spring rate } [N/m], x = \text{distance of spring compression } [m], a = \text{acceleration } [m/s^2], v = \text{velocity } [m/s], s = \text{velocity } [m/s$ travelled distance [m], $t_s = \text{time step } [s]$

The most optimally performing off-the-shelve spring that was found is the "high performance" compression spring C00170003016, produced by Associated Spring SPEC, Evasham, UK (chrome vanadium/chrome silicon, free length 16.0 mm, outer diameter 1.70 mm, wire diameter 0.32 mm) with a spring rate of 1.3 N/mm and maximum compression of 3.5 mm, providing a force of 4.4 N at maximum compression. The velocities anticipated, neglecting any influence of friction, are 4.0 m/s and 12.6 m/s for masses of 1.0 gr and 0.1 gr, respectively.

Reload ability

The reload ability design is the most critical part of this concept. For compressing or tensing the spring, a connection between the free spring end and the catheter end should be made to control and apply the needed load. This connection, needs to be decoupled from the spring during the release action, to prevent shape dependency and high friction influences on performance. The necessary mechanism to decouple the reloading action and release action may lead to high design complexity.

Shape dependency

The functioning of this actuator should not be influenced by the shape and length of the instrument, as the actuator may be located in the tip of the instrument. Therefore, the concept is judged to function shape independently, similarly to the electromagnetic and SMA wire concepts.

C.5. ELASTIC STRETCH BAND

The basic mechanism of the idea to use an elastic band for generating force to accelerate an indenter is largely similar to the previously described helical spring; both mechanisms work with storage of elastic energy. However, elasticity in rubbery materials is nonlinear, in contrast with the elasticity of metal that is mostly used in helical springs. It is for this reason that the helical spring concept was selected as the more favourable elastic energy storage solution. The elastic stretch band concept will therefore not be taken into further consideration as actuation element.

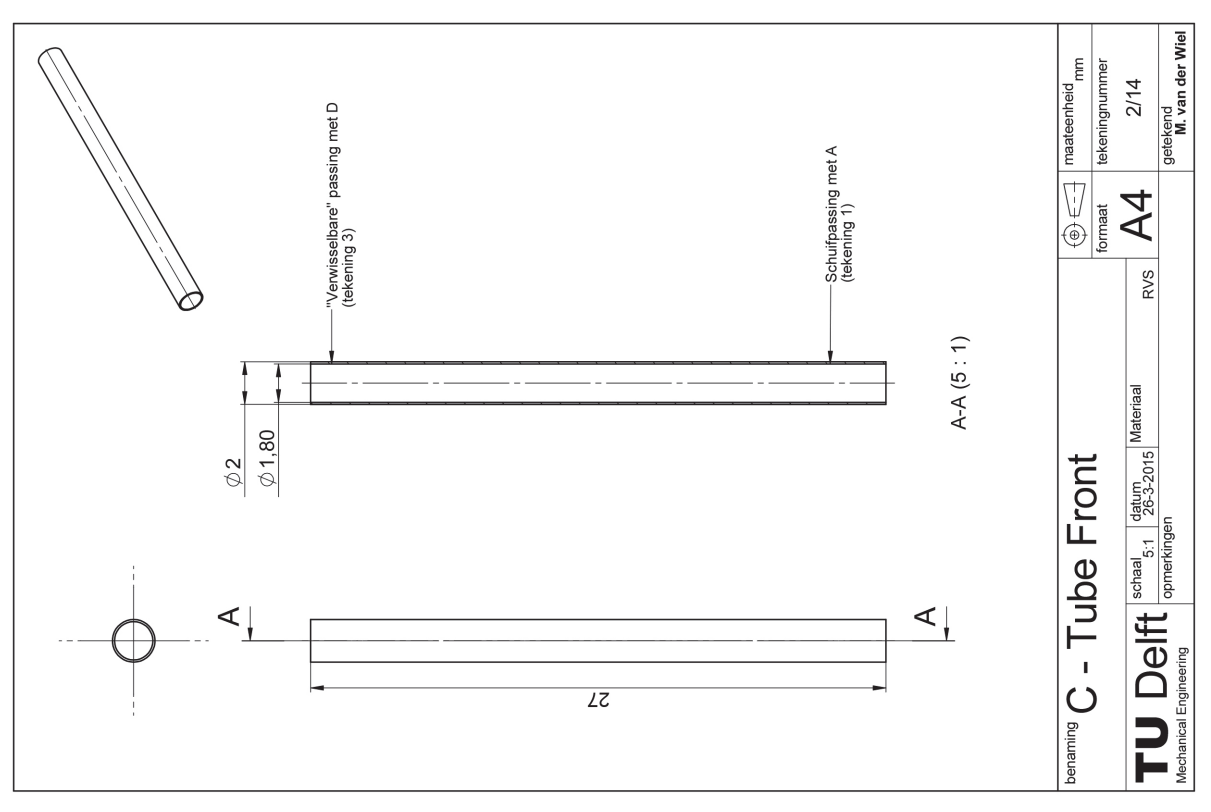
C.6. CONCLUSION

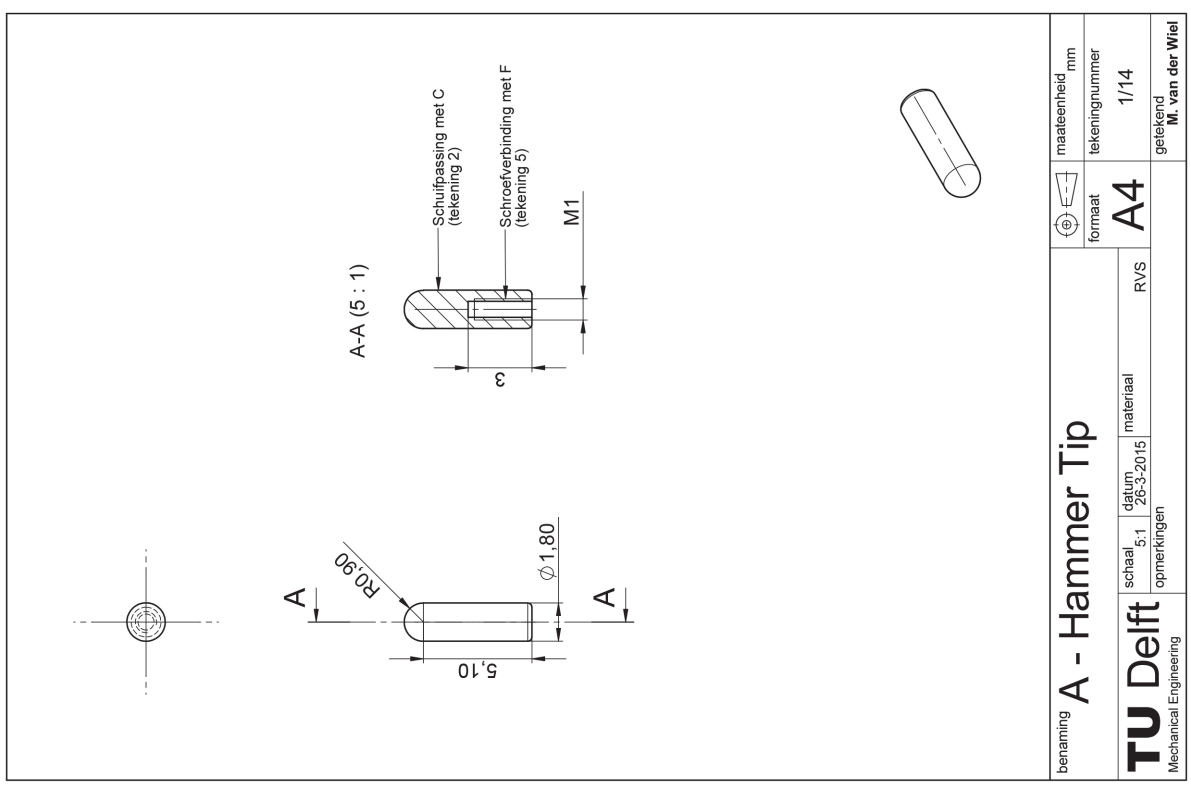
From this critical analysis of the five concepts that were selected as feasible concepts, it has been concluded that a helical compression spring is the most favourable and promising solution for actuating the instrument. This element shows no medical risks, should perform highly independent of catheter shape and is available in small dimensions. Furthermore, it has shown to be the most promising concept on performance for the level of velocity to be reached, based on estimates. Even though the necessity to design a reload mechanism with decoupling of the loading and release action, the uncertainty and complexity of this design was intuitively rated lower than the overall complexity and uncertainties that come with the design of the other actuation elements.

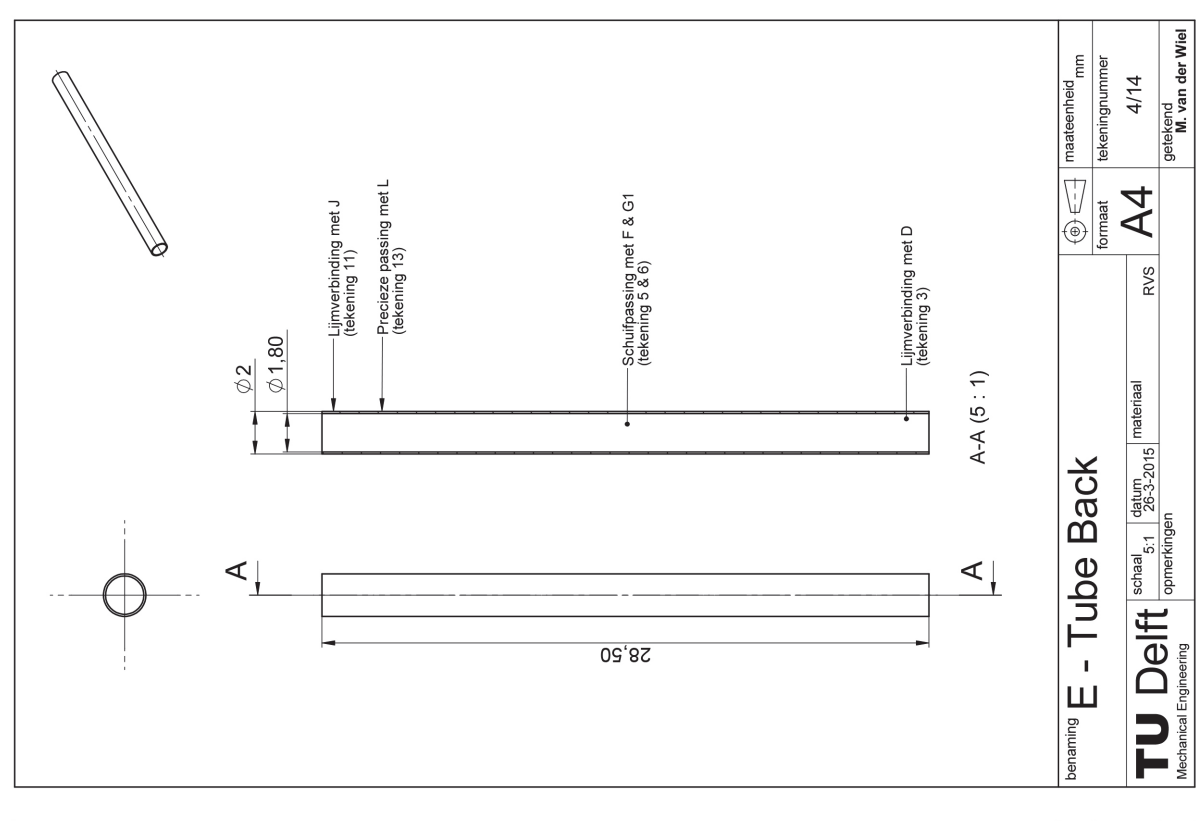
REFERENCES

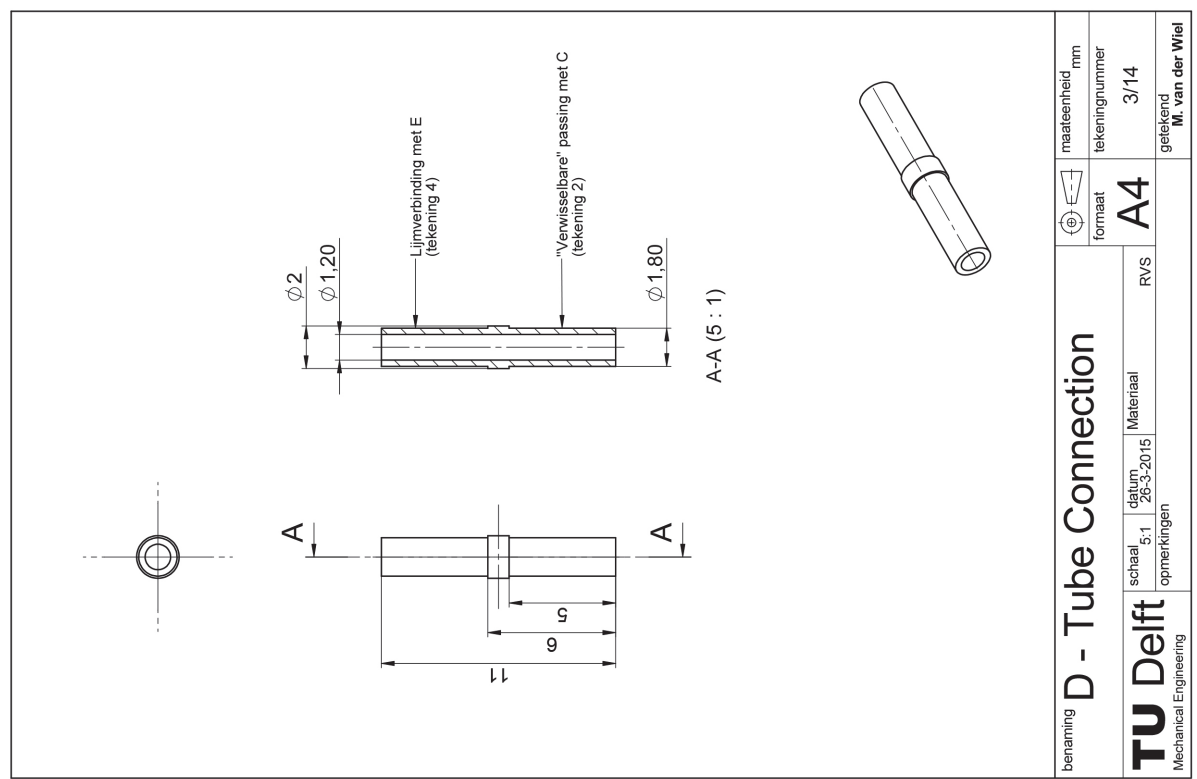
- [53] G. Smit, Natural grasping, design and evaluation of a voluntary closing adaptive hand prosthesis, Thesis (2003).
- [54] A. H. Robbins and W. Miller, Circuit analysis: Theory and practice (Cengage Learning, 2012).
- [55] M. Follador, M. Cianchetti, A. Arienti, and C. Laschi, *A general method for the design and fabrication of shape memory alloy active spring actuators*, Smart Materials and Structures **21**, 115029 (2012).
- [56] W. Huang and W. Toh, *Training two-way shape memory alloy by reheat treatment*, Journal of materials science letters **19**, 1549 (2000).
- [57] R. Vepa, *Dynamics of smart structures* (JohnWiley & Sons, 2010).

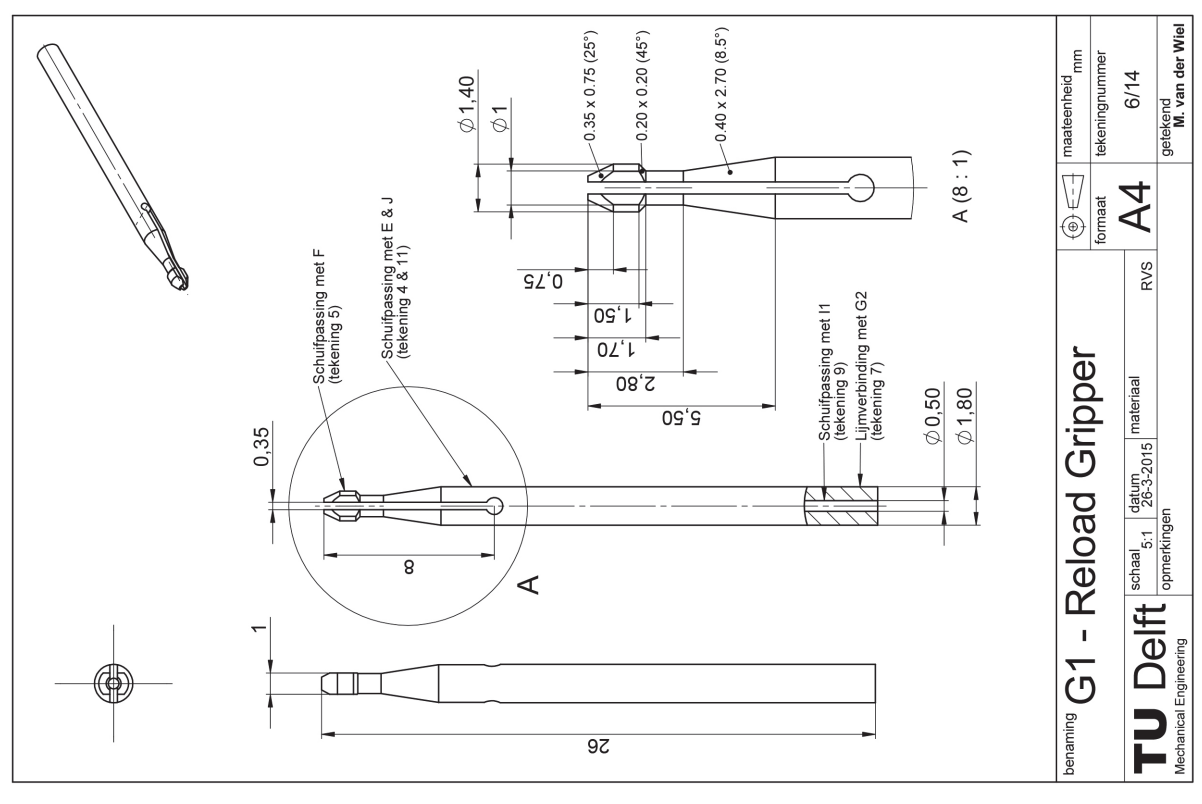
D. TECHNICAL DRAWINGS

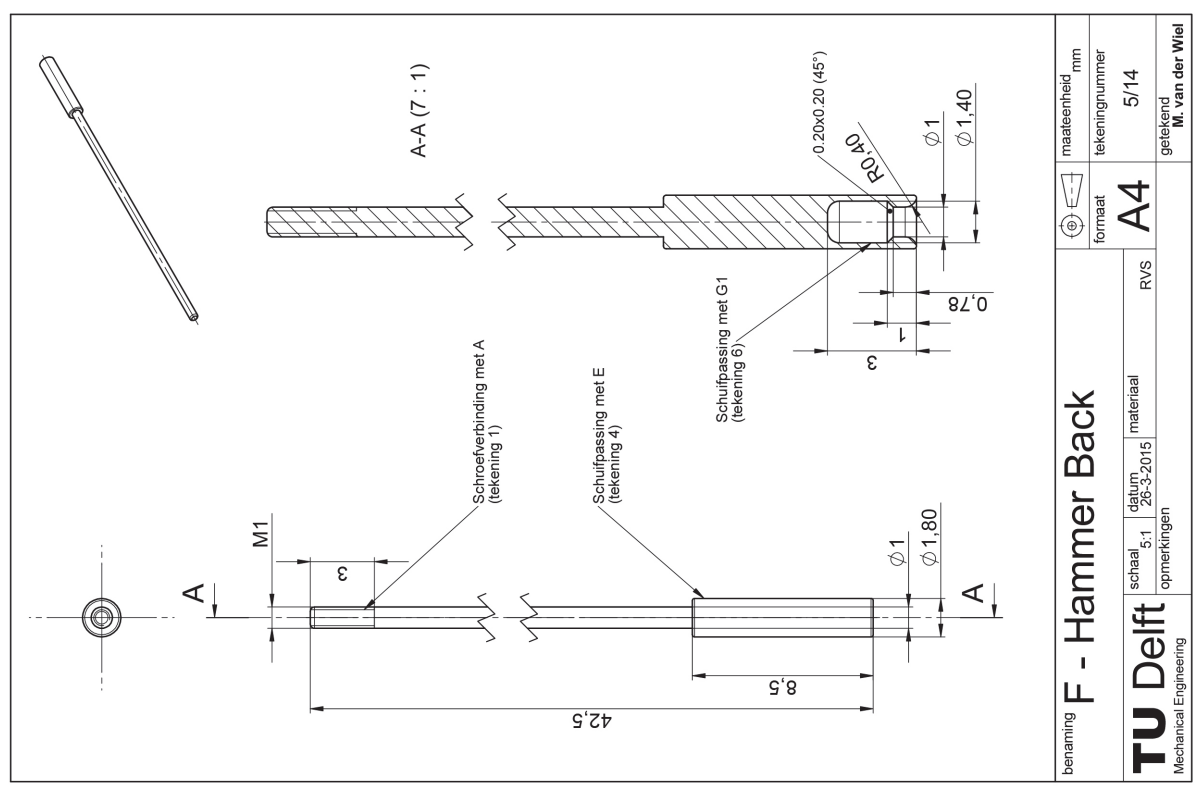


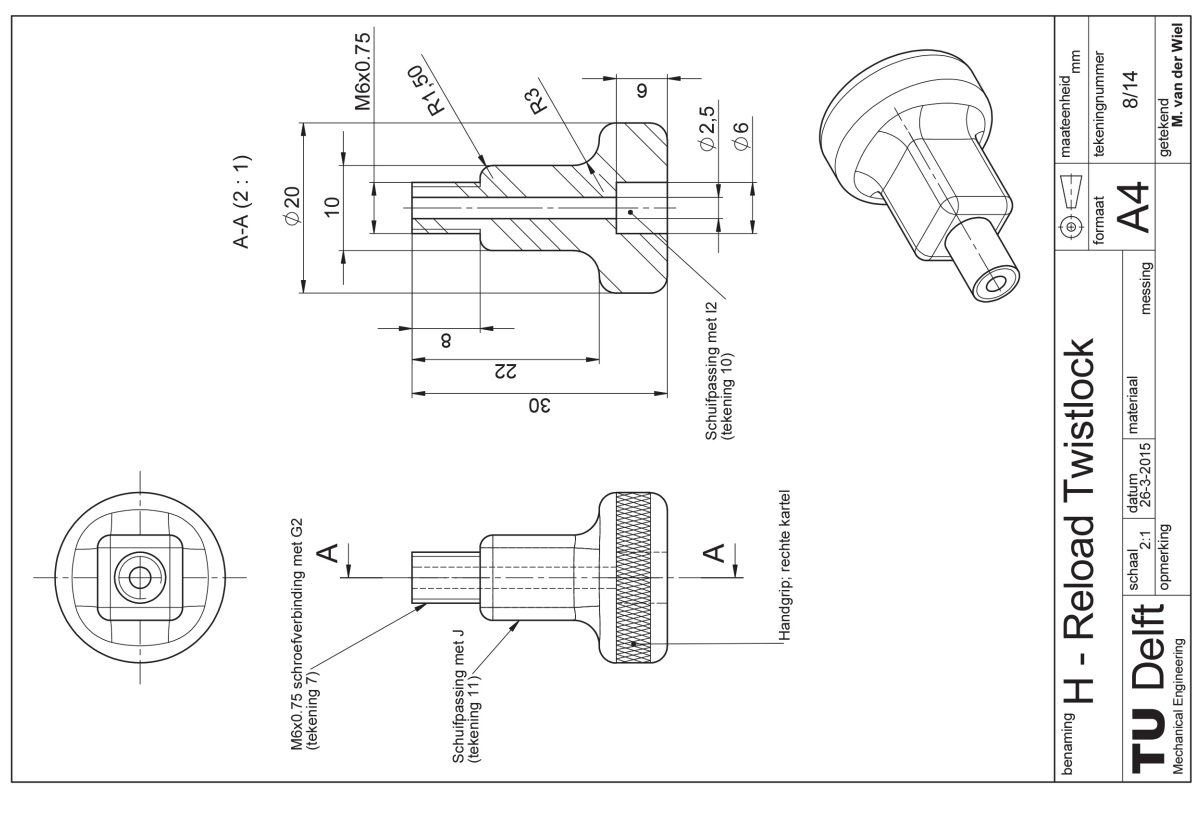


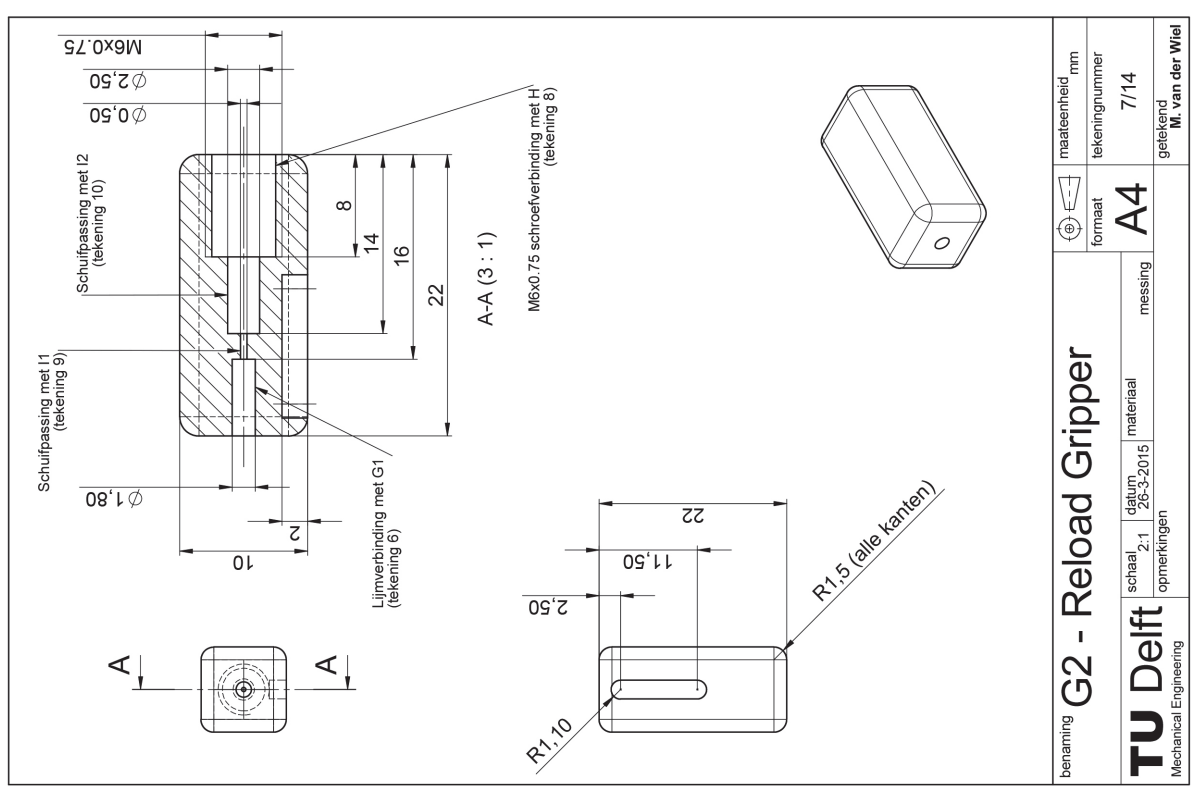


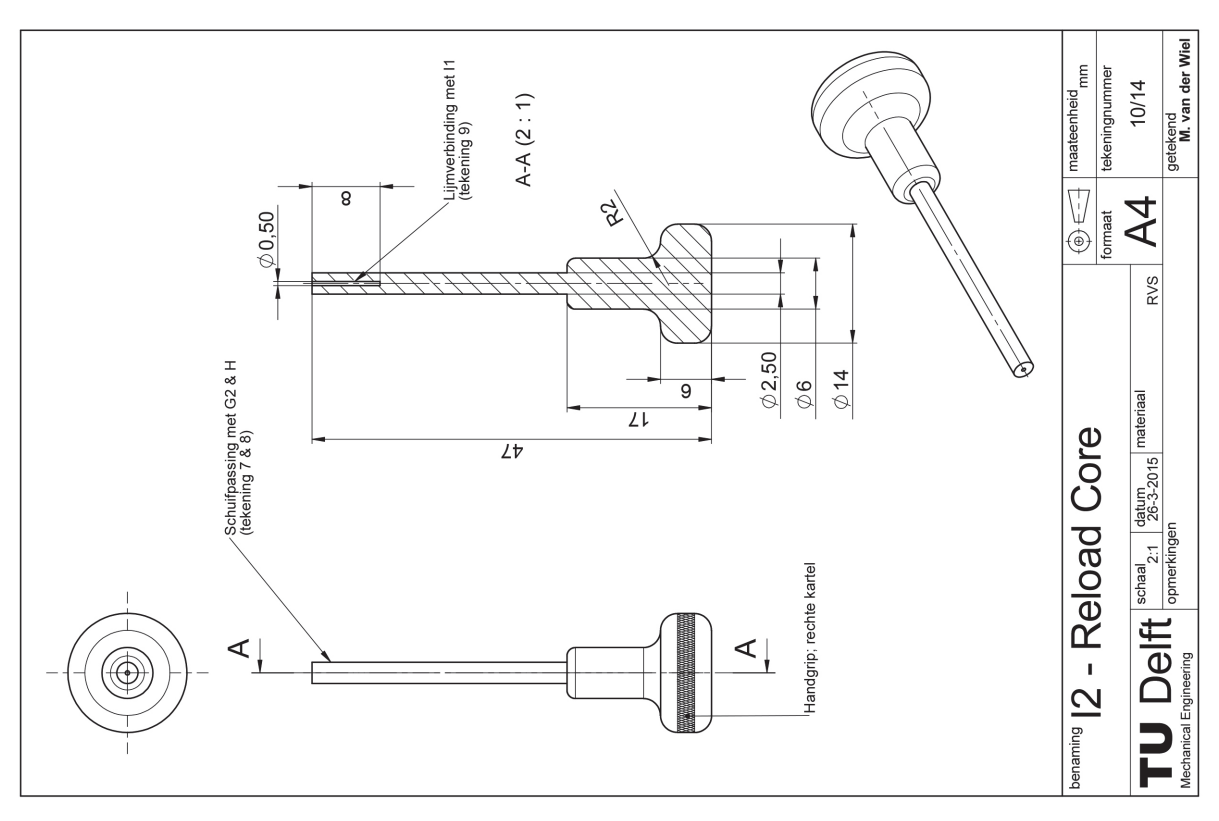


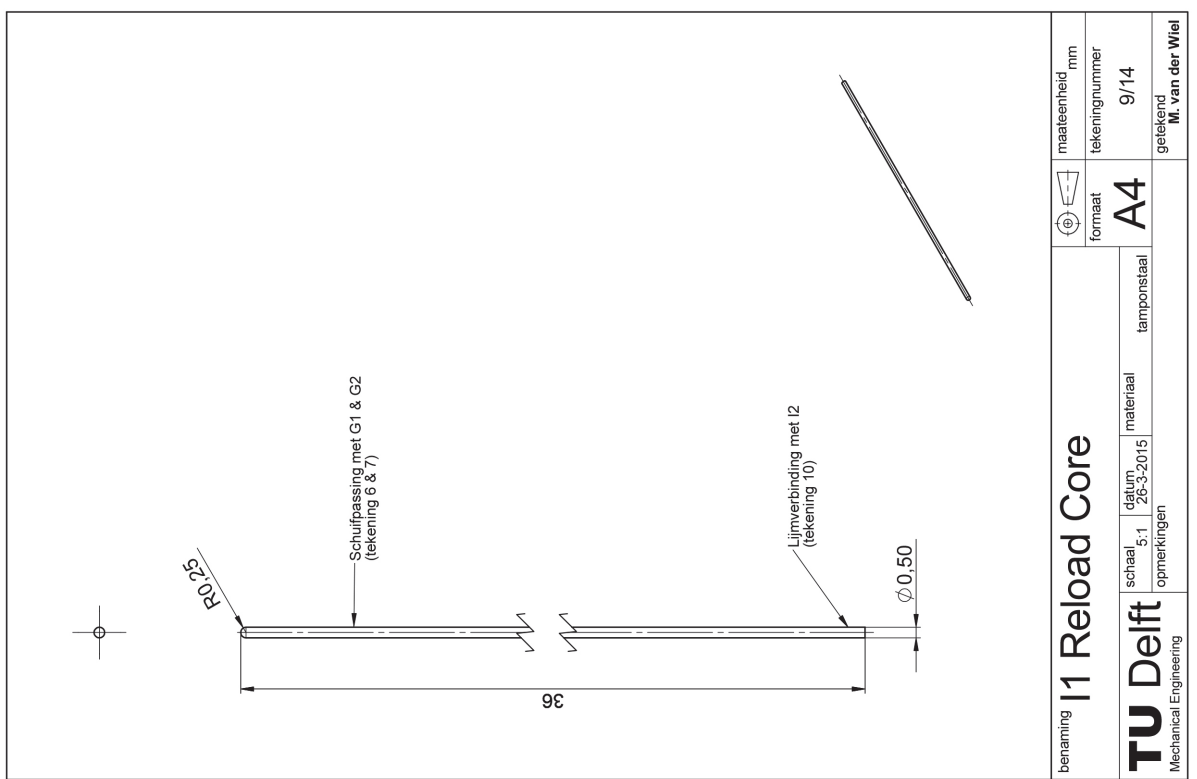


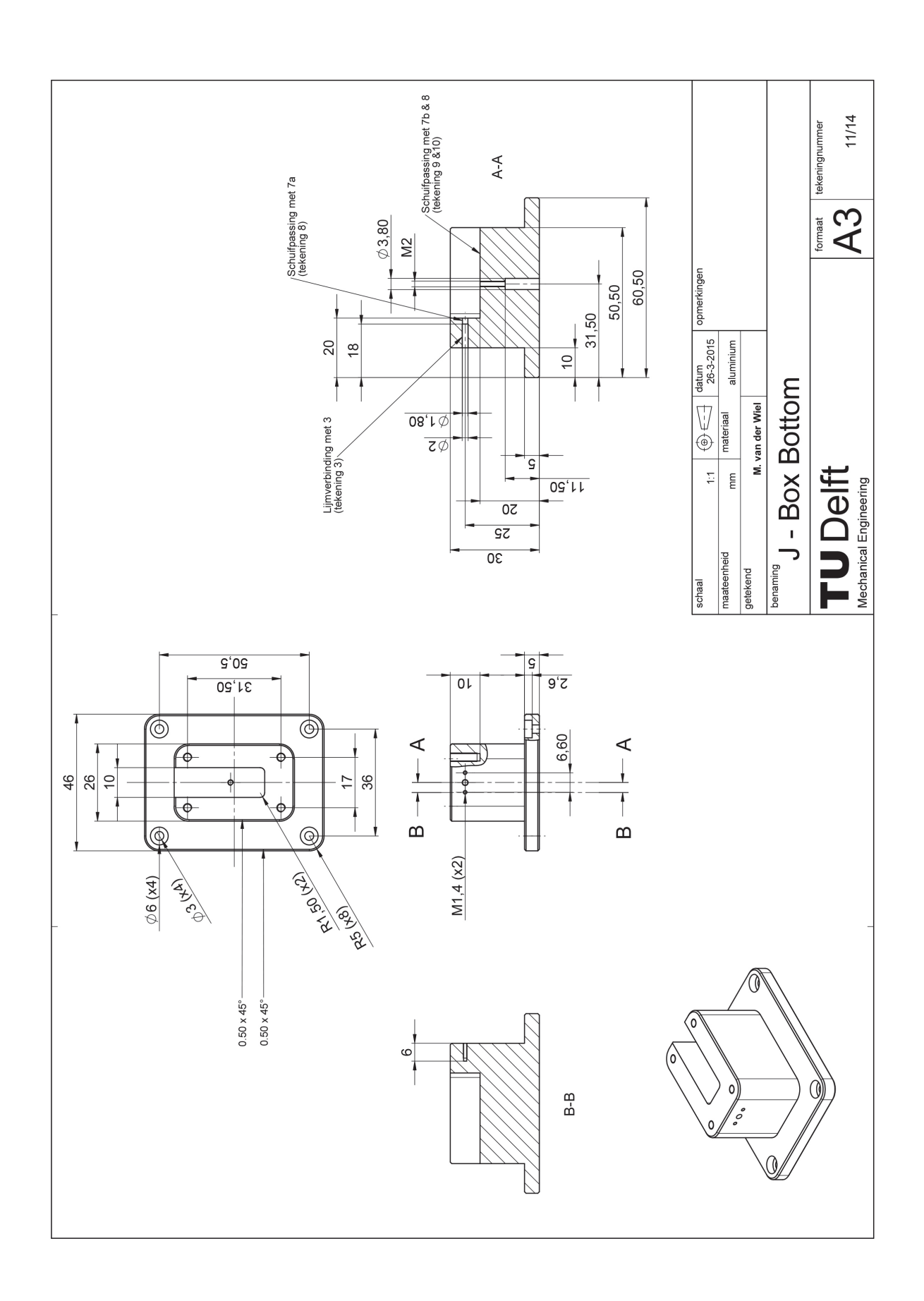


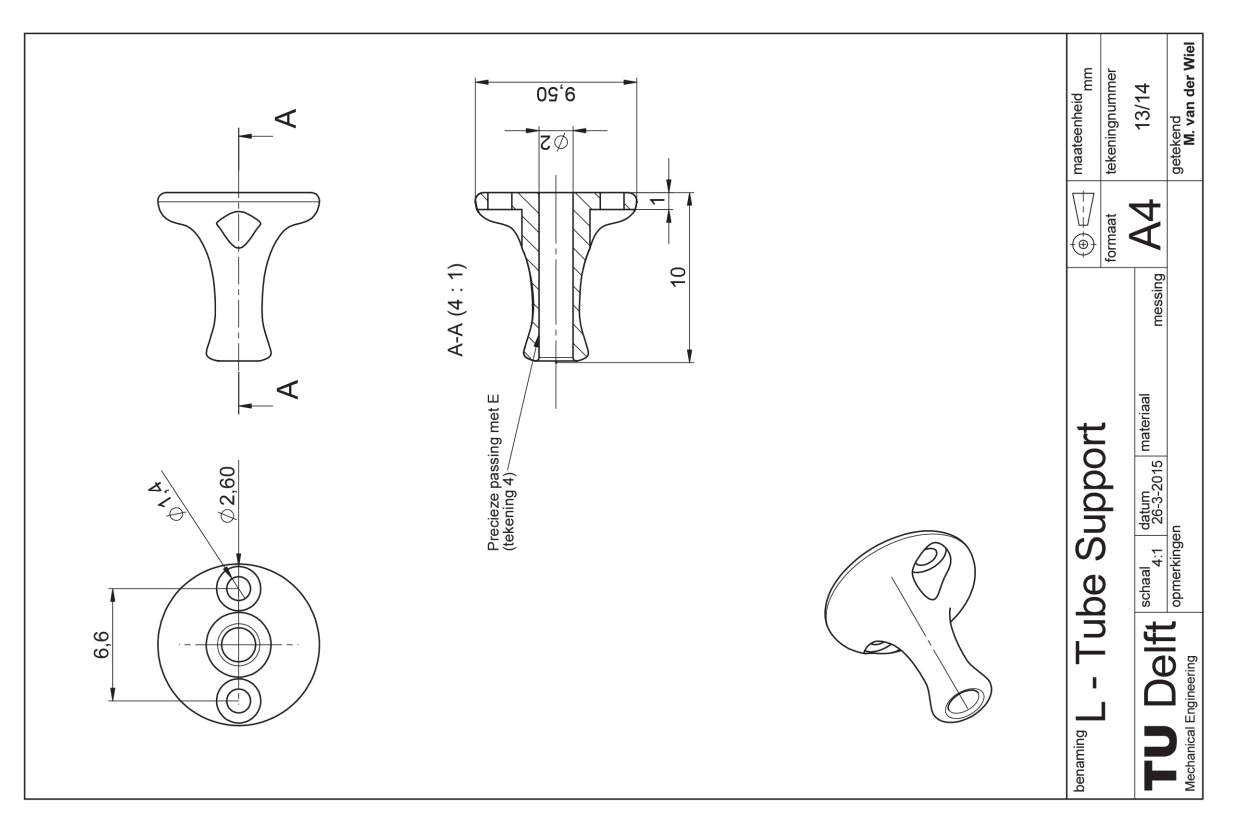


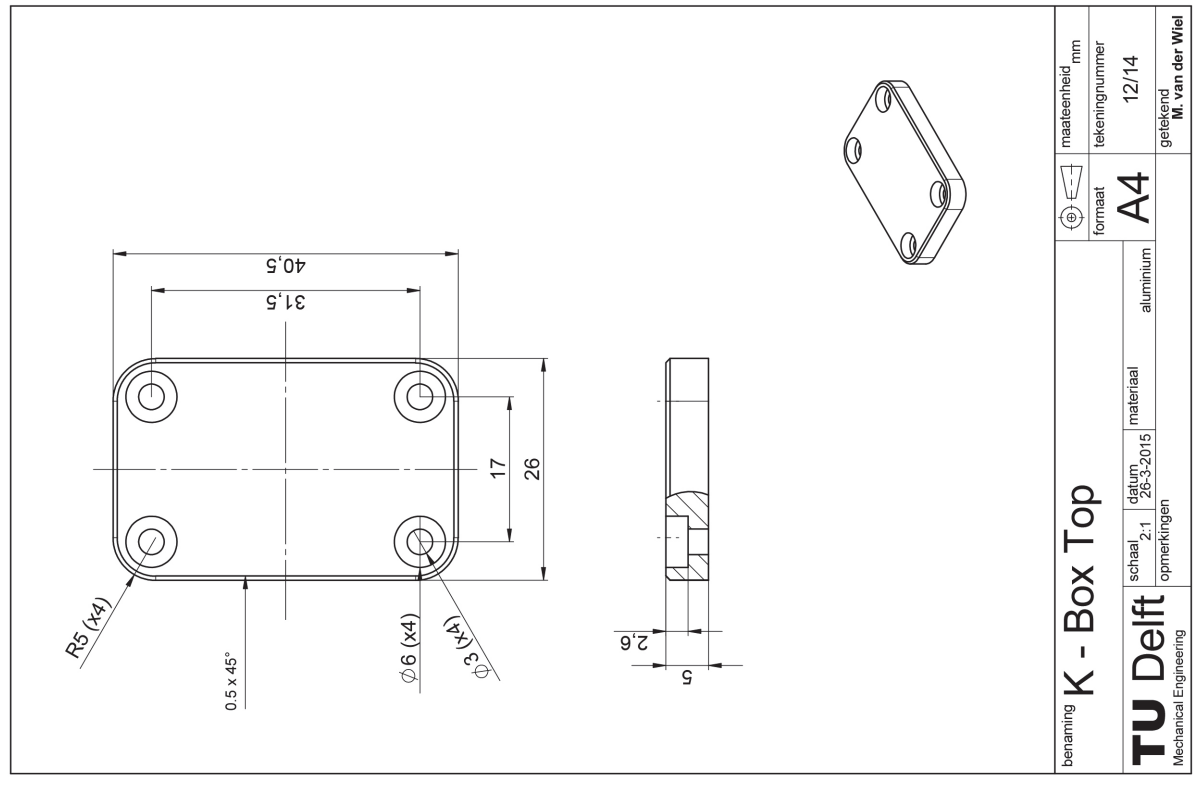


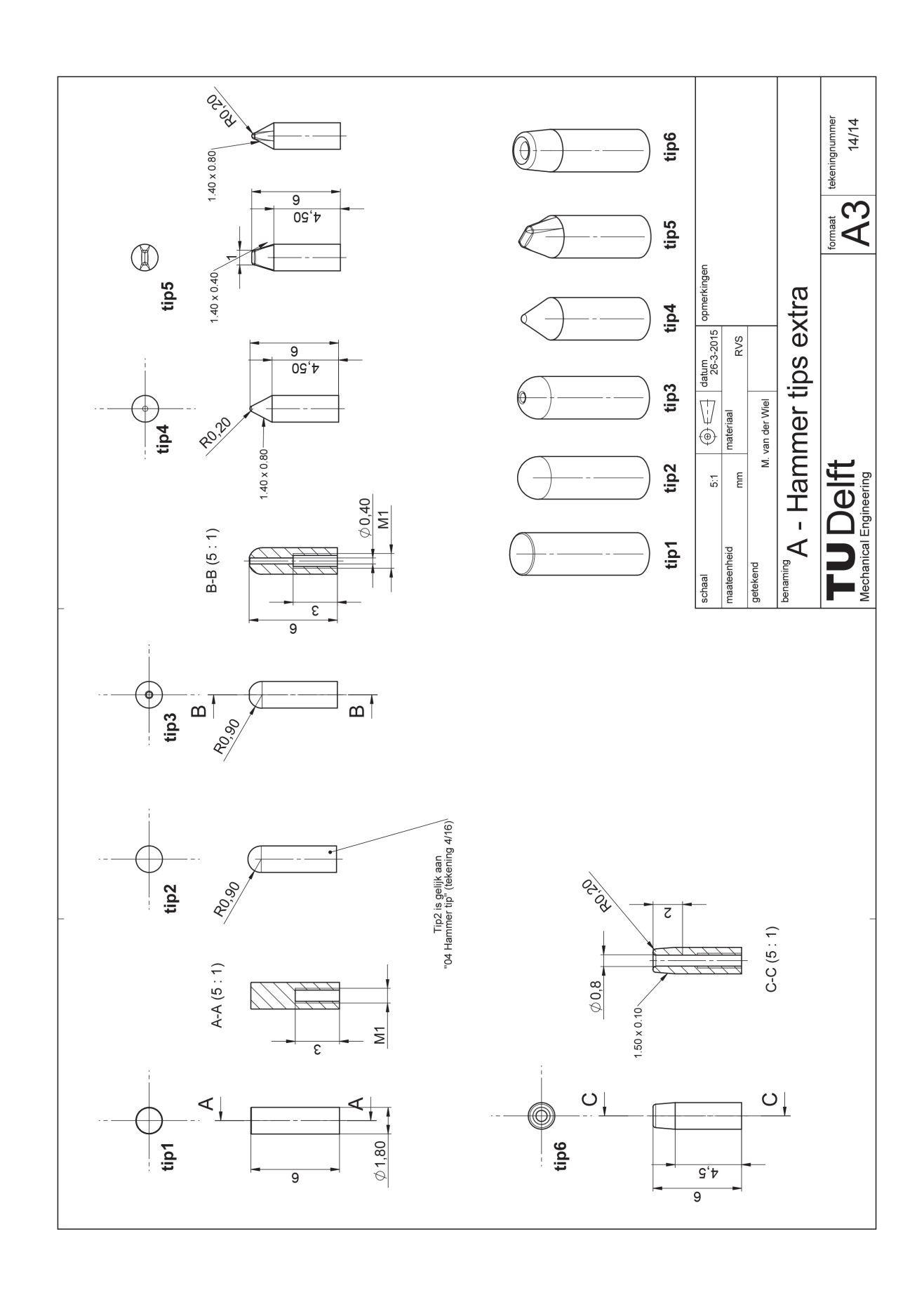












E. CTO MODEL CREATION

Within this appendix, the procedure that was followed to create the surrounding (cardiac) tissue models and proximal cap models for experimenting will be described stepwise. The surrounding tissue was mimicked with a gelatine mixture with 25wt% pure gelatine and 75wt% clear water. The proximal cap models were made of plaster cast powder mixed with the gelatine mixture or clear water.

E.1. CARDIAC TISSUE MODEL

The following 11 steps describe the creation of the cardiac tissue model:

- 1. Weigh a correct amount of gelatine (Sheet gelatin, Dr. Oetker, Bielefeld, Germany).
- 2. Put the gelatine sheets in a bath of cold clear water ($\sim 15^{\circ}$ C), and leave them to soak for a moment (5 minutes).
- 3. Take the gelatine sheets from the bath and wring them cautiously before putting them in a plastic container.
- 4. Weigh the new (soaked) mass of the gelatine sheets, and add an amount of cold clear water to create the correct total volume (25wt% gelatine from step (1), to a total 100wt% of soaked gelatine and added water).
- 5. Put the gelatine-filled container in a bath of warm water ($\sim 50^{\circ}$ C) and stir gently until the content is completely liquid.
- 6. Take the container from the bath and leave it to rest for a moment (15 minutes), during which all bubbles will float to the surface to be taken out.
- 7. Put the gelatine mixture within the small container, which can subsequently be put within the mould shown in Figure E.1.
- 8. Close the mould with the lid, to create a notch within the gelatine volume.
- 9. Leave the gelatine-filled container for approximately 1 hour within a refrigerator ($\sim 2^{\circ}$ C), before gently removing the lid of the mould from the gelatine (see Figure E.2).
- 10. Finally, close the lid of the small container and leave it for another 24 36 hours in the refrigerator.
- 11. To ensure constant tissue stiffness, the tissue model is to be used directly from the refrigerator (< 1 hour) within the timing of the 24 36 hours mentioned in the previous step.



Figure E.1: Mould, including 10 surrounding (cardiac) tissue models, to create notches within the gelatine volume.



Figure E.2: Cardiac tissue models with created notches in the center.

E.2. PROXIMAL CAP MODEL

The following 10 steps describe the creation of the basic proximal cap models:

- 1. Create the gelatine mixture as described in step 1 6 from the previous procedure (surrounding tissue model).
- 2. Weigh a correct amount of plaster cast powder (SHERAALPIN Hartgips hellblau, SHERA Werkstoff-Technologie GmbH & Co. KG).
- 3. Put the powder in a small plastic cup and add a correct amount of gelatine mixture into the cup.
- 4. Stir the mixture gently, while holding the cup in a bath of warm water ($\sim 50^{\circ}$ C), until a homogeneous mixture has formed.
- 5. Pour the mixture onto the mould, and close the mould with force (see Figure E.3).
- 6. Leave the filled mould for a while (20 minutes) in a refrigerator (~ 2°C), to cool and stiffen the created mixture.
- 7. Remove the mould from the refrigerator, and open it to take out the formed slice of (at this moment still flexible) material.
- 8. Press the small circles from the material with the help of a thin-walled tube, as shown in Figure E.4.
- 9. Pack the created models into cling film, and leave it for another 24 28 hours in the refrigerator.
- 10. To ensure constant material stiffness, the model is to be used directly from the refrigerator (< 1 hour) within the timing of the 24 28 hours mentioned in the previous step.



Figure E.3: Mould for the proximal cap models, to create the desired 1 mm material thickness, filled with the gelatine/plaster cast mixture



Figure E.4: The complete moulded slice of material (left), thin-walled tube to press the circles (top right), and final proximal cap models (lower right).

F. EXPERIMENTAL DATA SETS

This appendix includes the complete data sets and detailed analysis of the experiments performed within the study. This includes the analysis of images from the HSVs to find the indenter velocity and dynamic CTO model behaviour, analysis of the data sets obtained with the load cell to find the impact peak forces (in air and in fluid), and the gathered data and images from the puncture effectiveness studies. The data and analyses will be presented seperately for the different experimental setups.

F.1. INDENTER VELOCITY

This section includes the complete analysis of the velocities that the indenter reaches at different spring compression and distances from the instrument tip (in free flight). The velocities were calculated by means of measuring the travelled distance of the indenter in between two images captured in the HSVs. The measured distances are presented in Figures F.1 - F.5. The calculated velocities and velocity means are presented in Table F.1.

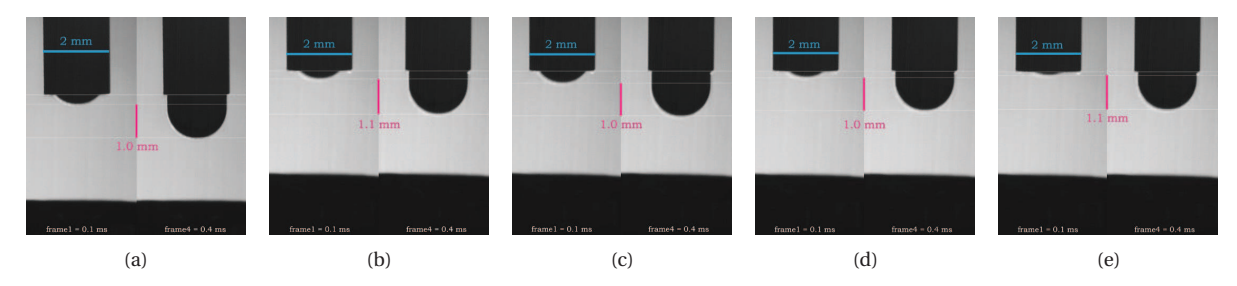


Figure F1: Analysis of indenter speed during the initial part of free flight from HSV images. Spring compression set to 3.5 mm. Calculated mean indenter velocity is 3.4 m/s.

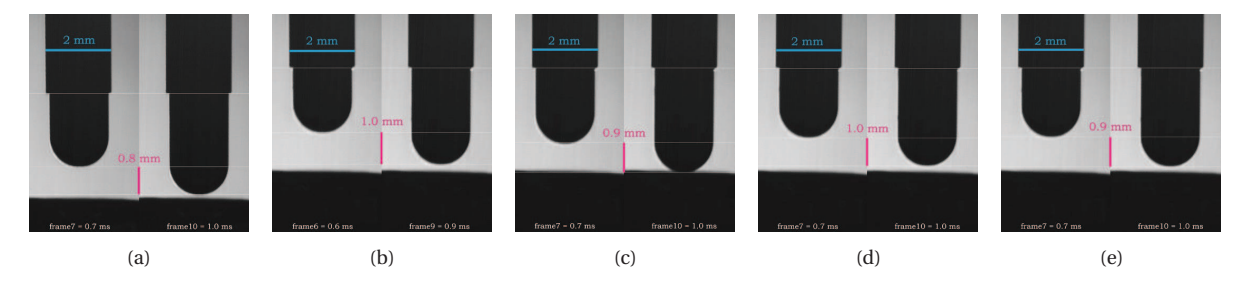


Figure F.2: Analysis of indenter speed during the final part of free flight from HSV images. Spring compression set to 3.5 mm. Calculated mean indenter velocity is 3.0.

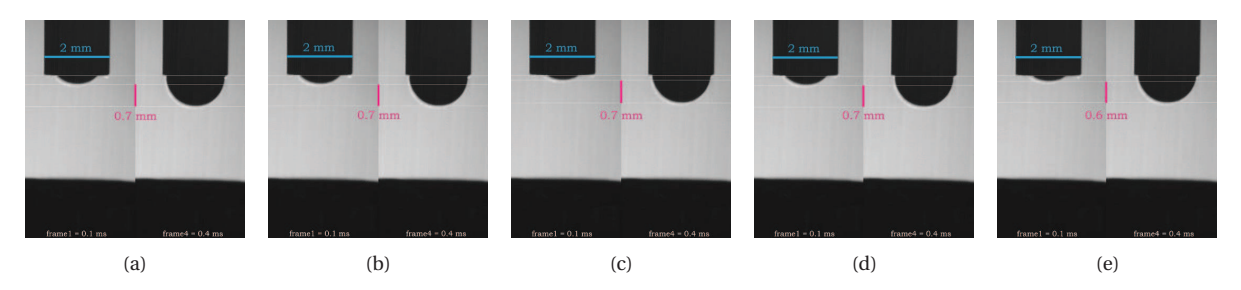


Figure E3: Analysis of indenter speed during the initial part of free flight from HSV images. Spring compression set to 2.8 mm. The calculated mean indenter velocity is 2.2.

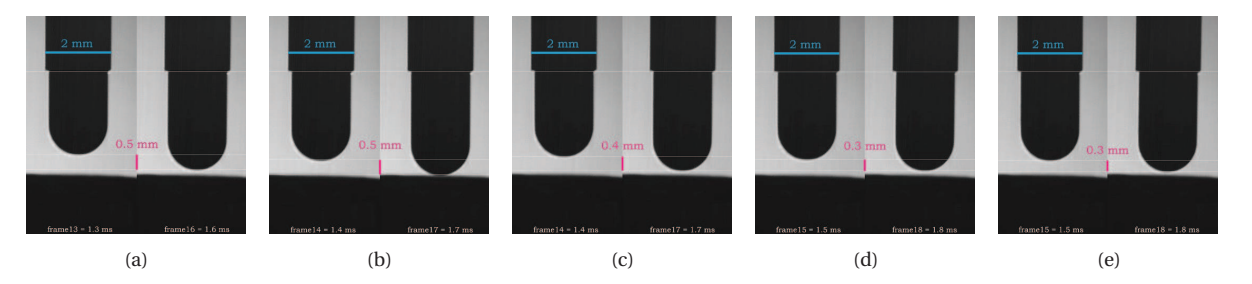


Figure F4: Analysis of indenter speed during the final part of free flight from HSV images. Spring compression set to 2.8 mm. The calculated mean indenter velocity is 1.3.

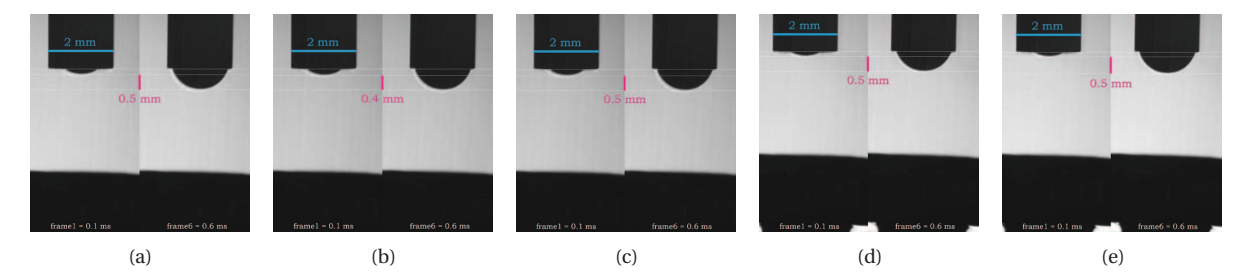


Figure F.5: Analysis of indenter speed during the initial part of free flight from HSV images. Spring compression set to 2.0 mm. The calculated mean indenter velocity is 1.0.

Table F.1: Calculated velocities for each of the HSV image analyses, and the calculated mean velocities of the groups, given in m/s. The mechanical settings are given as *object distance / spring compression distance* in the first row.

	1 mm / 3.5 mm	3 mm / 3.5 mm	1 mm / 2.8 mm	3 mm / 2.8 mm	1 mm / 2.0 mm
1	3.4	2.8	2.3	1.5	1.0
2	3.6	3.2	2.2	1.5	0.9
3	3.3	3.0	2.3	1.4	1.0
4	3.4	2.9	2.2	1.2	0.9
5	3.5	3.0	2.1	1.1	1.0
Mean	3.4 m/s	3.0 m/s	2.2 m/s	1.3 m/s	1.0 m/s

F.2. IMPACT PEAK FORCE

This section includes the complete analysis of the peak force measurements (in air), that were performed with the indenter striking onto a miniature S beam load cell. The collected sensor data has been processed with an algorithm correcting for the offset at zero applied force and searching for the highest numbers in each data set, which represent the peak force. These peak forces are given in Table F.2 for the primary test and in Table F.3 for the secondary test, including the calculated mean of the 5 repetitions.

Table E.2: Peak forces of the primary force measurements with a load cell, and the calculated mean of the groups, given in Newton. The mechanical settings are given as *object distance / spring compression distance* in the first row.

	1 mm / 3.5 mm	3 mm / 3.5 mm	1 mm / 2.8 mm	3 mm / 2.8 mm	1 mm / 2.0 mm	3 mm / 2.0 mm
1	18.4	19.6	12.1	12.3	5.1	2.5
2	17.7	18.5	12.9	11.9	4.5	3.1
3	18.1	18.2	12.5	10.9	4.1	1.6
4	19.3	18.8	12.0	10.5	4.6	2.4
5	19.8	18.0	12.1	10.6	4.3	2.6
Mean	18.7 N	18.6 N	12.4 N	11.2 N	4.5 N	2.5 N

Table E3: Peak forces of the secondary force measurements with a load cell, and the calculated mean of the groups, given in Newton. The mechanical settings are given as *object distance / spring compression distance* in the first row.

	1 mm / 3.5 mm	3 mm / 3.5 mm	1 mm / 2.8 mm	3 mm / 2.8 mm	1 mm / 2.0 mm	3 mm / 2.0 mm
1	18.3	20.1	13.0	12.6	6.5	6.0
2	18.4	19.5	12.8	13.8	6.3	6.1
3	19.6	18.8	13.3	13.0	6.4	6.3
4	19.1	18.5	13.1	12.7	6.2	7.0
5	19.1	19.0	13.0	12.3	6.4	6.6
Mean	18.9 N	19.2 N	13.0 N	12.9 N	6.4 N	6.4 N

F.3. PUNCTURE EFFECTIVENESS

This section includes an overview of the results obtained during the puncture effectiveness study. The data is presented without any processing. The counted number of strikes to cause penetration, together with the measured proximal cap model thicknesses for all of the trials, is presented in Table F.4. The captured images of the imprinted and fractured *soft*, *basic* and *hard* models are shown in Figures F.6, F.7, and F.8, respectively.

Table F.4: Complete overview of the retrieved results of the effectiveness experiments; striking the indenter onto the proximal cap models. The table includes the number of strikes ("s", maximum tested = 10) and the measured model thickness ("t"), given in millimeters, for experiments with the different indenter tip shapes (top row) and material models (left column).

		STA	MP	SPHE	RICAL	WEI	DGE	PO	INT	RIN	GED	SPHE	RE HOLE
		s	t	s	t	s	t	s	t	s	t	s	t
SOFT	I	> 10	1.15	> 10	1.13	> 10	1.09	> 10	1.13	> 10	1.18	> 10	1.14
	II	> 10	1.15	> 10	1.18	> 10	1.17	> 10	1.19	> 10	1.13	> 10	1.1
	III	> 10	1.16	> 10	1.16	> 10	1.14	> 10	1.11	> 10	1.12	> 10	1.11
BASIC	I	9	1.17	4	0.9	6	0.97	> 10	1.12	5	0.94	> 10	1.22
	II	> 10	1.15	5	1.13	7	1.11	7	0.97	10	1.23	9	1.02
	III	6	0.91	> 10	1.24	5	0.95	> 10	1.19	9	1.19	10	1.02
HARD	I	2	1.23	3	1.22	3	1.21	8	1.27	2	1.22	3	1.25
	II	3	1.25	3	1.27	3	1.25	8	1.24	2	1.24	2	1.21
	III	5	1.25	2	1.22	3	1.27	> 10	1.23	2	1.23	3	1.23

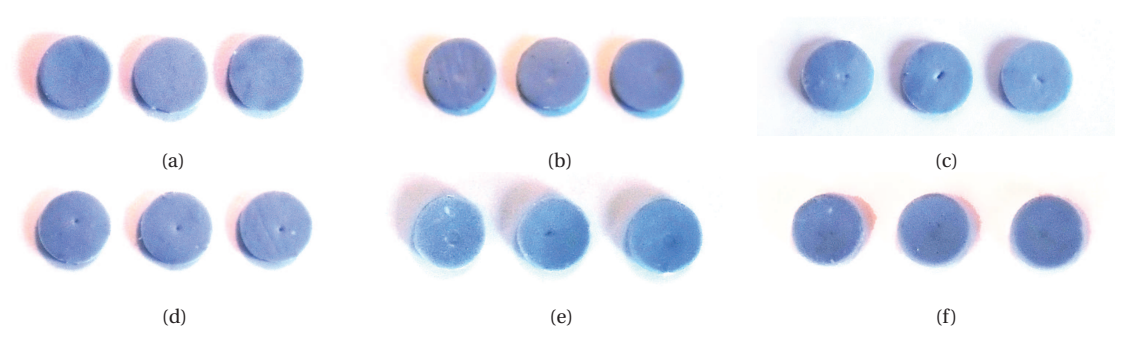


Figure F.6: Images of the resulting soft proximal cap models after striking several times with the indenter onto the model, for (a) the stamp indenter, (b) spherical indenter, (c) wedge indenter, (d) pointed indenter, (e) ringed indenter, and (f) spherical indenter with guidewire passage.

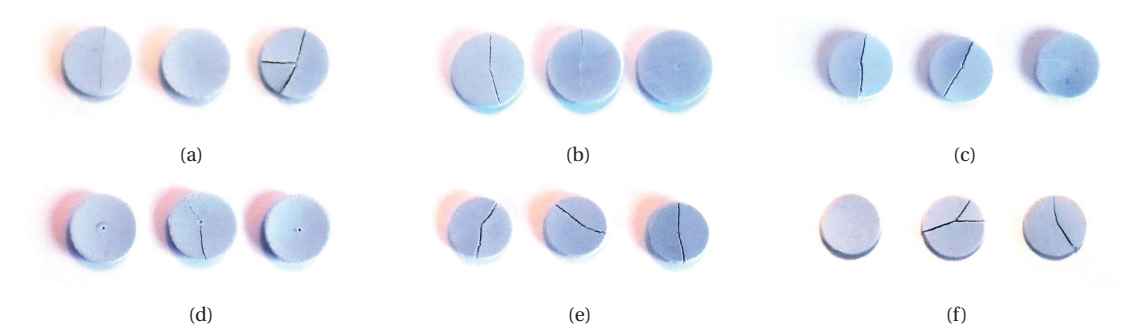


Figure F.7: Images of the resulting basic proximal cap models after striking several times with the indenter onto the model, for (a) the stamp indenter, (b) spherical indenter, (c) wedge indenter, (d) pointed indenter, (e) ringed indenter, and (f) spherical indenter with guidewire passage.

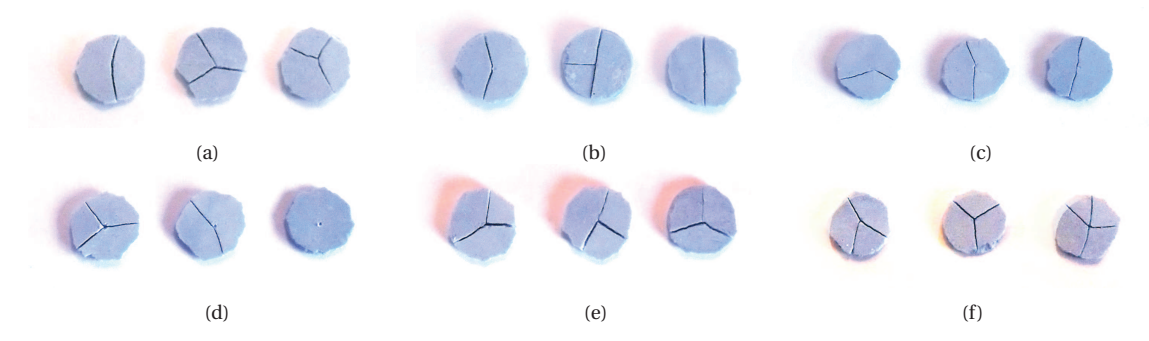


Figure F.8: Images of the resulting hard proximal cap models after striking several times with the indenter onto the model, for (a) the stamp indenter, (b) spherical indenter, (c) wedge indenter, (d) pointed indenter, (e) ringed indenter, and (f) spherical indenter with guidewire passage.

F.4. IMPACT PEAK FORCE IN LIQUID

This section includes the complete analysis of the peak load measurements that were performed with the indenter immersed in BMF, striking onto a miniature S beam load cell. The collected sensor data has been processed similarly as explained for the Section 2 (impact peak force) of this Appendix. The peak loads are given in Table F.5, including the calculated mean of the 5 repetitions.

Table F.5: Peak forces measured by the load cell with the indenter immersed into BMF, and the calculated mean of the groups, given in Newton. The mechanical settings are given as *object distance | spring compression distance* in the first row.

	1 mm / 3.5 mm	3 mm / 3.5 mm	1 mm / 2.8 mm	3 mm / 2.8 mm	1 mm / 2.0 mm	3 mm / 2.0 mm
1	9.2	8.7	5.6	4.7	2.3	1.2
2	9.3	8.4	5.4	4.6	2.5	1.6
3	9.3	8.0	6.1	4.5	2.6	0.4
4	9.2	6.9	6.0	3.1	2.4	0.1
5	9.1	7.4	5.8	3.5	2.1	0.1
Mean	9.2 N	7.9 N	5.8 N	4.1 N	2.4 N	0.7 N

F.5. DYNAMIC MODEL BEHAVIOUR

The final section of this appendix contains the complete analysis of the dynamic behaviour of the CTO model, based on HSV image analysis. First of all, in Figure F.9 the measured distances of the bouncing indenter are shown, with which the bounce velocity was determined. Secondly, in Figure F.10 the measured distances of the CTO displacement are presented. Finally, in Table F.6 an overview of the measured velocities and displacements is given.

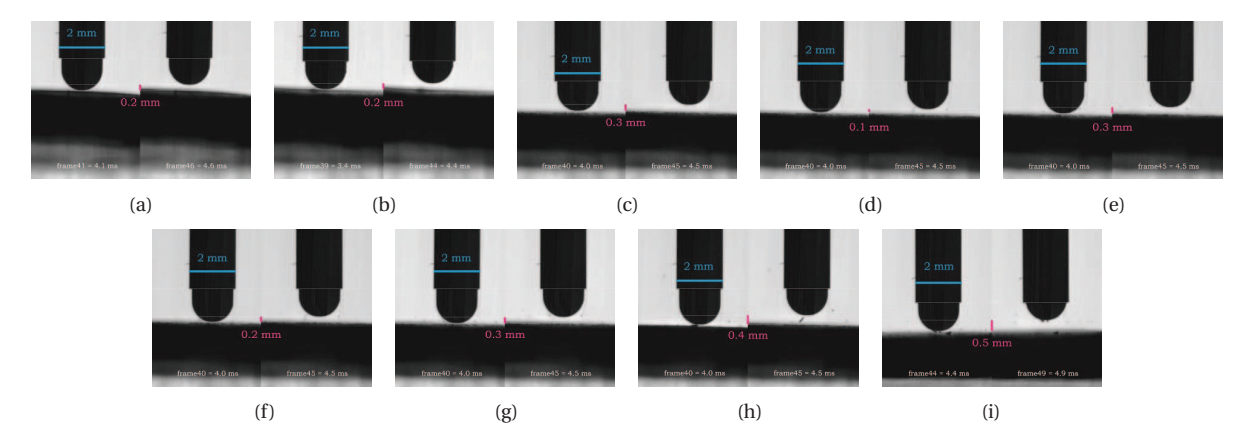


Figure F9: Analysis of the indenter bounce velocity, after striking onto a CTO model with maximized spring compression (3.5 mm) and at short distance from the CTO (1 mm). The following proximal cap models are presented: (a) soft model, (b) basic model, (c) hard model, strike 1, (d) hard model, strike 2, (e) hard model, strike 3, (f) hard model, strike 4, (g) hard model, strike 5, (h) hard model, strike 6, broken, and (i) a second hard model, strike 5, broken.

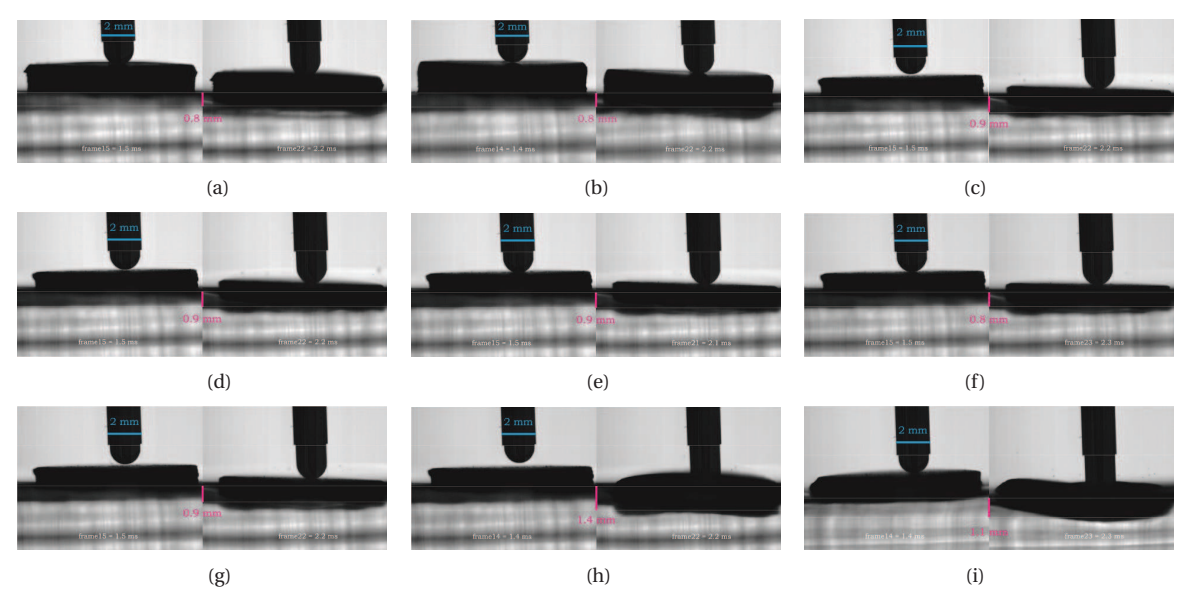


Figure F.10: Analysis of the CTO displacement, after striking onto a CTO model with maximized spring compression (3.5 mm) and at short distance from the CTO (1 mm). The following proximal cap models are presented: (a) soft model, (b) basic model, (c) hard model, strike 1, (d) hard model, strike 2, (e) hard model, strike 3, (f) hard model, strike 4, (g) hard model, strike 5, (h) hard model, strike 6, broken, and (i) a second hard model, strike 5, broken.

Table F.6: Measured indenter bounce velocities and CTO displacements, as part of the dynamical model behaviour, for different used proximal cap models.

		Velocity [m/s]	CTO displacement [mm]
Soft model unbroken	strike 1	0.5	0.8
Basic model unbroken	strike 1	0.5	0.8
Hard model unbroken	strike 1	0.5	0.9
	strike 2	0.2	0.9
	strike 3	0.5	0.9
	strike 4	0.4	0.8
	strike 5	0.5	0.9
Hard model broken	strike 6	0.8	1.4
Hard model broken	strike 5	0.9	1.1